EXPERIMENTAL DEFORMATION OF NATURAL AND SYNTHETIC DOLOMITE

A Thesis

by

NATHAN E. DAVIS

Submitted to the Office of Graduate Studies of
Texas A&M University
in partial fulfillment of the requirements for the degree of

MASTER OF SCIENCE

August 2005

Major Subject: Geology

EXPERIMENTAL DEFORMATION OF NATURAL AND SYNTHETIC DOLOMITE

A Thesis

by

NATHAN E. DAVIS

Submitted to the Office of Graduate Studies of
Texas A&M University
in partial fulfillment of the requirements for the degree of

MASTER OF SCIENCE

Approved by:

Co-Chairs of Committee, Andreas Kronenberg
Julie Newman
Committee Members, David V. Wiltschko
James E. Russell
Head of Department, Richard L. Carlson

August 2005

Major Subject: Geology

ABSTRACT

Experimental Deformation of Natural and Synthetic Dolomite.

(August 2005)

Nathan E. Davis, B.S., University of Missouri: Rolla

Co-Chairs of Advisory Committee: Dr. Andreas Kronenberg
Dr. Julie Newman

Natural and hot isostatically pressed dolomite aggregates were experimentally deformed at effective pressures of $P_e = 50 - 400$ MPa, temperatures of 400 – 850°C, and strain rates of $\dot{\varepsilon} = 1.2\text{x}10^{-4}\ \text{s}^{-1}$ to $1.2\text{x}10^{-7}\ \text{s}^{-1}$. Coarse- and fine-grained dolomite deformed at low temperature ($T \leq 700$°C for coarse-grained natural dolomite, $T < 700$°C for fine-grained natural and synthetic dolomite) exhibit mechanical behavior that is nearly plastic; differential stresses are insensitive to strain rate, fitted either by a power law $\dot{\varepsilon} = \dot{\varepsilon}_o \left(\frac{\sigma_1 - \sigma_3}{\mu} \right)^n$ with n values that range from 12 to 49 or an exponential law $\dot{\varepsilon} = \dot{\varepsilon}_o \exp[\alpha(\sigma_1 - \sigma_3)]$ with exponential law term α values from 0.023 to 0.079 MPa^{-1}. Microstructures of samples deformed at low temperatures include mechanical twins, and undulatory extinction suggesting that twin glide and dislocation slip are the predominant deformation mechanisms.

At high temperatures ($T \geq 800$°C) flow strengths of coarse- and fine-grained dolomite depend more strongly on strain-rate and exhibit pronounced temperature dependencies. Microstructures of coarse-grained dolomite samples deformed at $T \geq$

800°C include undulatory extinction and fine recrystallized grains suggesting that recovery and dynamic recrystallization contribute to dislocation creep at these conditions. By comparison with lower temperature deformation, mechanical twinning is unimportant. Fine-grained synthetic dolomite deformed at high temperature ($T \geq 700°C$) exhibits nearly linear (Newtonian) viscous behavior, with $n = 1.28$ (±0.15) consistent with grain boundary (Coble) diffusion creep.

At low temperatures ($T \leq 700°C$) coarse-grained dolomite exhibits higher strengths at higher temperatures which cannot be described by an Arrhenius relation, while fine-grained dolomite strengths show little or no temperature dependence. At high temperatures ($T \geq 800°C$), dislocation creep of coarse-grained dolomite can be described by a thermally activated power law $\dot{\varepsilon} = \dot{\varepsilon}_o \left(\frac{\sigma_1 - \sigma_3}{\mu} \right)^n \exp\left(\frac{-H^*}{RT} \right)$ with $H^*/n = 60$ kJ/mol, or by an exponential law $\dot{\varepsilon} = \dot{\varepsilon}_o \exp[\alpha(\sigma_1 - \sigma_3)] \exp\left(\frac{-H^*}{RT} \right)$ with $H^*/\alpha = 25447$ kJ/mol. At high temperatures, diffusion creep of fine-grained synthetic dolomite can be described by $\dot{\varepsilon} = \dot{\varepsilon}_o \left(\frac{\Omega}{d^3} \right) \left(\frac{\sigma_1 - \sigma_3}{\mu} \right)^n \exp\left(\frac{-H^*}{RT} \right)$ with $H^* = 280 \pm 45$ kJ/mol. Taken together, the flow laws for coarse- and fine-grained dolomites constrain the high temperature conditions over which crystal plasticity, dislocation creep, and diffusion creep dominate.

DEDICATION

To my parents,

for tolerating my continued pursuit of education.

ACKNOWLEDGMENTS

Without the help and assistance of the following personnel, facilities, companies and organizations this project would not have been possible.

Project funding was under NSF EAR Tectonics Grant # 0107078.

Facilities used were The John Handin Rock Deformation Lab, Center for Tectonophysics, Dept. of Geology and Geophysics, Texas A&M University, College Station TX, 77843-3115; and the Materials Preparation Center at Ames Laboratory, 111 TASF, Ames, IA 50011-3020.

I would like to acknowledge the help and assistance of the following personnel, Clayton Powell, lab technician, John Handin Rock Deformation Lab; Paul Wheelock, lab technician, MPC at Ames Laboratory; and Ray Guillemette, research scientist, Electron Microprobe at the Department of Geology and Geophysics, Texas A&M University.

Materials were provided by Polar White Marble Quarry, near Madoc, Ontario, a part of Upper Canada Stone Company Ltd., 55 Cedar Pointe Drive, Unit # 606A, Barrie, Ontario L4N 5R7, Canada; and Dolomitwerk Jettenberg division of Schöndorfer GmbH, Oberjettenberg 7, GERMANY 83458 Schneizlreuth.

TABLE OF CONTENTS

Page

LIST OF FIGURES

LIST OF TABLES

INTRODUCTION

As shallow marine sediments at continental margins, carbonates are commonly deformed during continental collision. As a result, mechanical properties of sediments consisting primarily of calcite and dolomite govern the stresses during collision and the deformation seen in many orogens (Heitzmann, 1987; Burkhard, 1990; Busch and van der Pluijm, 1995; Bestmann et al., 2000; Molli et al., 2000; Ulrich et al, 2002).

Field observations indicate that dolomites are stronger than calcite-rich carbonates. Dolomites often appear fractured while limestones and marbles may exhibit substantial internal strains (Woodward et al., 1988; Erickson, 1994; Busch and van der Pluijm, 1995; Bestmann et al., 2000). Interlayers of dolomites and limestones appear to lead to ramp-flat geometries of thrust faults (Heitzmann, 1987; Burkhard, 1990; Busch and van der Pluijm, 1995; Bestmann et al., 2000; Molli et al., 2000; Ulrich et al, 2002). Flat-lying decollements develop within weak calcite-rich units while ramps and high-angle brittle faults develop across strong dolomite units (e.g., Woodward et al., 1988; Erickson, 1994).

Early experimental studies are in broad agreement with these field studies, with fracture and flow strengths significantly higher for dolomite (Turner et al, 1954; Handin and Fairbairn, 1955; Higgs and Handin, 1959; Handin et al., 1967; Wenk and Shore, 1975; Barber, 1977; Barber and Wenk, 1979; Barber et al., 1981, 1983, 1994) than flow strengths measured for calcite rocks at comparable conditions (Griggs and Miller, 1951;

This thesis follows the style of Tectonophysics.

Handin and Griggs, 1951; Turner and Ch'ih, 1952; Griggs et al., 1951, 1953, 1960; Turner et al., 1956; Heard, 1960, 1963; Heard and Raleigh, 1972; Schmid, 1976; Schmid et al., 1977, 1980; Wenk et al., 1983; Fredrich et al., 1989; Rowe and Rutter, 1990; de Bresser and Spiers, 1993, 1997; Dressen and Evans, 1993; Rutter, 1995; de Bresser, 1996; Wang et al., 1996; Covey-Crump, 1997, 1998; Casey et al., 1998; Paterson and Olgaard, 2000). However, experimental studies of dolomite deformation have been exploratory in nature, and they are limited to a restricted set of conditions (Turner et al, 1954; Handin and Fairbairn, 1955; Higgs and Handin, 1959; Handin et al., 1967; Wenk and Shore, 1975; Barber, 1977; Barber and Wenk, 1979; Barber et al., 1981, 1983, 1994). Only those experiments documented by Barber et al. (1981, 1983) offer evidence for dislocation glide and creep. The conditions that favor different deformation mechanisms in dolomite have not been determined and flow laws describing high temperature creep have not been reported.

While fracture is documented and high strength can be inferred for many dolomite occurrences, field studies have also documented ductile deformation of other dolomites, notably those deformed at greenschist and amphibolite facies conditions (White and White, 1980; Newman and Mitra, 1994; Leiss et al., 1994, 1996; Leiss and Barber, 1999). Motivated by these occurrences of deformed dolomites, I have investigated the strength and deformation mechanisms of polycrystalline dolomites by performing deformation experiments at temperatures of 400° to 850°C, strain-rates of $1.2 \times 10^{-4}\ s^{-1}$ to $1.2 \times 10^{-7}\ s^{-1}$, and effective pressures of 50 to 300 MPa. Over these conditions, I find evidence for a number of different deformation processes that govern mechanical response. At low temperature, dolomites deform by mechanical twinning and dislocation glide, leading to nearly perfect plasticity. At higher temperature, coarse-grained dolomite deforms by dislocation creep at reduced differential stress, and fine-grained dolomite deforms by diffusion creep, marked by nearly linear viscous response and low differential stresses.

PREVIOUS WORK

Previous experimental studies of dolomite deformation have identified several intracrystalline mechanisms of deformation. Mechanical twinning and dislocation glide have been activated in triaxial compression experiments on dolomite single crystals and critical resolved shear stresses determined at temperatures of 250° to 600°C (Barber et al., 1981). These same mechanisms have been observed in experimentally deformed dolomite rocks and flow strengths have been compared with limestones and marbles.

Triaxial compression experiments on crystallographically oriented dolomite single crystals combined with optical and electron microscopy have revealed 1) dislocation glide on the *c* plane parallel to the *a* direction, 2) mechanical twinning on *f* planes, 3) dislocation glide on *f* planes, 4) microcracking on *r* cleavage faces, and 5) minor secondary slip on *r* planes (Table 1, after Wenk et al., 1983; Higgs and Handin, 1959; Barber and Wenk, 1979; Barber et al., 1981, 1983). At any one set of conditions, shear stresses required to activate these mechanisms are greater than those for similar deformation mechanisms in calcite. Over the temperature range of 250°-500°C, critical shear strengths for *f*-twinning in dolomite are 90-100 MPa while *e*-twinning in calcite requires shear stresses of only 6.5-11.5 MPa (Table1). Slip on the *c*- and *f*-planes in dolomite occurs at $T \leq 700$°C with critical shear strengths of 50-130 and 100-170 MPa, respectively, while r^+- and f^+-slip in calcite occur at shear stresses both below 20 MPa. Only when the slip vectors are reversed relative to the calcite structure do the critical shear strengths increase, with r^--slip requiring 18-64 MPa and f^--slip requiring 16-210 MPa. Experimental studies of dolomite single crystal deformation also show an unusual

Table 1. Deformation mechanisms in carbonates (from Wenk et al., 1983)

Deformation mechanisms in rhombohedral carbonates (* = important mechanism).

	System	Burgers vector (if known)	Strain rate -log sec^{-1}	T, °C	Critical shear stress, MPa	Reference
CALCITE	slip					
	*r^- $\{10\bar{1}4\}\langle\bar{2}021\rangle$	1/3$\langle 20\bar{2}1\rangle$	1	300-500	64-18	**Turner et al. (1954)**
			7	300-500	30-13	"
	*r^+		5	600	16	**Spiers & Wenk (1980)**
	*f^- $\{\bar{1}012\}\langle 02\bar{2}1\rangle$		4	25-800	210-16.5	Turner et al. (1954)
	*f^+		5	600	18	Spiers & Wenk (1980)
	c $(0001)\langle 2\bar{1}\bar{1}0\rangle$					Turner & Orozco (1976)
	a $\{\bar{1}2\bar{1}0\}\langle\bar{2}021\rangle$					**Paterson & Turner (1970)**
	twinning					
	*$e^+$$\{\bar{1}018\}\langle\bar{2}021\rangle$		1	25-500	11.5-6.5	**Turner et al. (1954)**
			4	25-500	8.0-8.5	"
	$r^+$$\{10\bar{1}4\}\langle\bar{2}021\rangle$		5	500	>12	**Weiss & Turner (1972)**
DOLOMITE	slip					
	*c$(0001)\langle 2\bar{1}\bar{1}0\rangle$	1/3$\langle 2\bar{1}\bar{1}0\rangle$	5	25-700	50-130	Barber et al. (1981);
		1/3$\langle 1\bar{1}00\rangle$		∿ 300-500		Barber et al. (1983)
	*f^- $\{\bar{1}012\}\langle 2\bar{2}01\rangle$	1/6$\langle 2\bar{2}01\rangle$	5	25-700	170-100	Barber et al. (1981)
	r^- $\{10\bar{1}4\}\langle\bar{1}2\bar{1}0\rangle$		5	> 500		"
	twinning					
	*f $\{\bar{1}012\}\langle 10\bar{1}1\rangle$		5	∿250-600	90-100	"

temperature effect on *c*-slip. Both Higgs and Handin (1959) and Barber et al. (1981) show an inverse temperature dependence for samples that are not well oriented for *f*-slip. Samples that are oriented to allow *f*-slip display a normal temperature dependence, and are weaker with increasing temperature.

Microstructural analyses of experimentally deformed polycrystalline dolomite rocks (Turner et al, 1954; Handin and Fairbairn, 1955; Wenk and Shore, 1975; Barber, 1977, Barber et al., 1983, 1994) have documented many of the same deformation mechanisms as reported for dolomite single crystals. Differential stresses measured in triaxial compression are large compared with those measured for polycrystalline calcite samples. However, flow strengths have not been measured systematically as a function of confining pressure, strain-rate, or temperature. In addition, high temperature experiments on polycrystalline dolomites have been restricted to coarse-grained rocks in which the predominant deformation mechanisms included twinning and slip with little evidence of intergranular deformation mechanisms such as grain boundary diffusion or sliding. The high strength of dolomite relative to calcite is thought to result from differences in crystal structure and the influence of cation ordering on intracrystalline deformation mechanisms. Fine-grained calcite rocks deform by grain boundary diffusion and sliding at elevated temperatures (Schmid, 1976; Schmid et al., 1977, 1987; Walker et al., 1990; Herwegh et al., 2003) and it is not clear whether crystal structure and ordering impose restrictions on these mechanisms in fine-grained dolomite.

EXPERIMENTAL METHODS

The mechanical properties of polycrystalline dolomite rocks and synthetic dolomite aggregates were determined by performing triaxial compression experiments at constant strain-rate. Deformation mechanisms were documented by optical microscopy.

Starting Materials

Four polycrystalline dolomites were investigated in this study, including two coarse-grained dolomite marbles, designated as Madoc dolomite and Kern Mtn. dolomite, a fine-grained natural dolomite, known as Blair dolomite, and a fine-grained synthetic dolomite. The grain sizes and compositions of the starting materials are listed in Tables 2 & 3. Chemical analyses of each starting material were obtained using a Cameca SX-50 electron microprobe in the department of Geology and Geophysics at Texas A&M University. Analyses were conducted using wavelength dispersive spectrometers equipped with LiF, PET and TAP crystals. Backscattered electron (BSE) imaging was used to detect secondary phases in the starting materials.

Coarse-grained Madoc dolomite was obtained from the “Polar White” marble quarry of Upper Canada Stone in Ontario, Canada. Optical examination of this material (Figure 1A) reveals equant grains, 240 ±30 μm in diameter, with straight extinction in crossed-polarized light, some twins, and straight, sharply defined grain boundaries, and negligible porosity (~1%). BSE imaging reveals few secondary phases and electron microprobe analyses indicate a nearly perfect, stoichiometric composition with only a trace of Fe (Table 3).

Table 2. Starting materials

Material	grain size	Chemical formula	mineral impurities
Madoc	240±30μm	$Ca_{0.999}\ Mg_{0.998}\ Fe_{0.001}(CaCO_3)_2$	trace calcite
Kern	80±20μm	$Ca_{1.005}\ Mg_{0.989}\ Si_{0.002}\ Na_{0.002}(CaCO_3)_2$	trace quartz
Blair	10±5μm	$Ca_{1.012}\ Mg_{0.957}\ Fe_{0.006}\ Si_{0.018}\ Al_{0.004}(CaCO_3)_2$	10% quartz, trace mica
synthetic	2.5±1.5μm	$Ca_{1.014}\ Mg_{0.982}(CaCO_3)_2$	

Table 3. Wt.% oxides

Analysis	Madoc	Kern	Synthetic	Blair
SiO2	BDL	0.067	BDL	0.453
Al2O3	BDL	BDL	BDL	0.114
FeCO3	0.082	BDL	BDL	0.343
MnCO3	BDL	BDL	BDL	BDL
MgCO3	45.657	45.439	44.770	43.894
CaCO3	54.202	54.789	54.827	55.087
SO3	BDL	BDL	BDL	BDL
Na2O	BDL	0.031	BDL	BDL
SrCO3	BDL	BDL	BDL	BDL
Total	100.038	100.446	99.752	100.011

Si	BDL	0.002	BDL	0.018
Al	BDL	BDL	BDL	0.004
Fe	0.001	BDL	BDL	0.006
Mn	BDL	BDL	BDL	BDL
Mg	0.998	0.989	0.982	0.957
Ca	0.999	1.005	1.014	1.012
S	BDL	BDL	BDL	BDL
Na	BDL	0.002	BDL	BDL
Sr	BDL	BDL	BDL	BDL

BDL = below detection limit

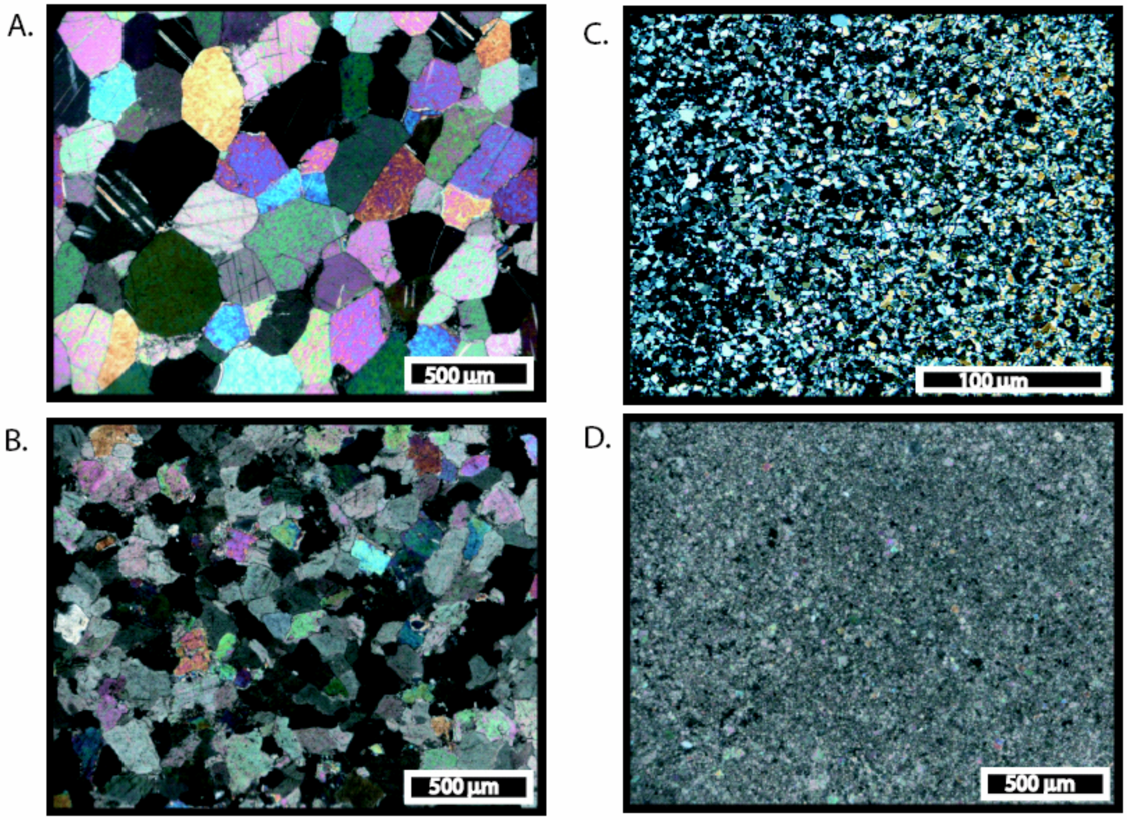

Figure 1. Undeformed dolomite materials in cross-polarized light. A. Madoc dolomite, B. Kern Mtns. dolomite, C. Synthetic dolomite, D. Blair dolomite.

A coarse-grained dolomite (Figure 1B) from the Kern Mountains of eastern Nevada was used in several experiments for comparison with our results for Madoc dolomite. This dolomite marble has a foliation in hand specimen but exhibits relatively equant grains in thin section (Figure 1B) with a grain size of 80 ±20 μm. Dolomite grains exhibit straight extinction and few twins. Electron microprobe analyses reveal that this dolomite is slightly enriched in Ca relative to Mg (Table 2). Trace levels of Na and Si are attributed to fine solid inclusions. BSE imaging reveals trace secondary minerals (<1%) including calcite and mica, and a very low porosity (<1%).

A fine-grained synthetic dolomite starting material was generated by hot-isostatic pressing methods similar to those used to synthesize fine-grained calcite aggregates (Olgaard and Fitz Gerald, 1993; Zhu et al., 1999). A natural, nearly stoichiometric dolomite powder, sieved to <5μm was obtained from the Dolomitwerk Jettenberg division of Schöndorfer GmbH, Oberjettenberg 7, GERMANY 83458 Schneizlreuth. This powder was first cold pressed at a confining pressure of 300 MPa, vacuum-welded into mild steel jacketing and then hot pressed at a confining pressure of 300 MPa and a temperature of 600°C for five days at the Materials Preparation Center of AMES Laboratory on the Iowa State campus in Ames, Iowa (thanks to the assistance and supervision of Paul Wheelock). The resulting synthetic dolomite (Figure 1C) has a grain size of 2.5 ±1.5 μm, a porosity of ~5% and a nearly perfect, stoichiometric composition (Table 2).

A fine-grained, dense (~1% porosity) dolomite known as Blair dolomite (Handin et al., 1967) was used in two experiments to compare with the results obtained for the fine-grained synthetic dolomite. Thin section observations of this dolomite reveal a grain size of 10 ±5 μm (Figure 1D) and microprobe analyses of the dolomite grains reveal a composition that is enriched in Ca relative to Mg and low levels of Fe (Table 2). Trace levels of Si and Al are attributed to fine solid inclusions. This dolomite contains as much as 10% quartz grains, and experiments were limited to low temperatures, to avoid any carbonate-silicate reactions during experiments.

Constant Strain-rate Experiments

Constant-strain-rate triaxial compression experiments were performed on right circular cylinders 20.2 (±0.6) mm in length and 8.8 (±0.05) mm in diameter using a Heard-type gas apparatus (John Handin Rock Deformation Laboratory). The samples were inserted into annealed (700°C) thin-walled (0.25 mm) silver jackets and a pair of aluminum oxide spacers was placed at each specimen end to provide insulation from the tungsten carbide (WC) pistons. The silver jacket was sealed to the tapered ends of the WC pistons by cold swaging using beveled WC push rings (Figure 2). The aluminum oxide spacers directly adjacent to each sample were solid, dense, and impermeable so that experiments are considered to represent undrained tests.

Confining pressures P_c of up to 400 MPa were applied by way of argon gas; confining pressure during experiments was controlled by manual operation during short experiments ($\dot{\varepsilon} \leq 10^{-5}$ s^{-1}) to within ±1 MPa and by servo-control during long experiments to within ±3 MPa. The chemical stability of dolomite was maintained as temperature was increased, owing to the undrained test configuration and generation of an internal CO_2 pore pressure (P_p or P_{CO2}) by the dissociation reaction of dolomite to

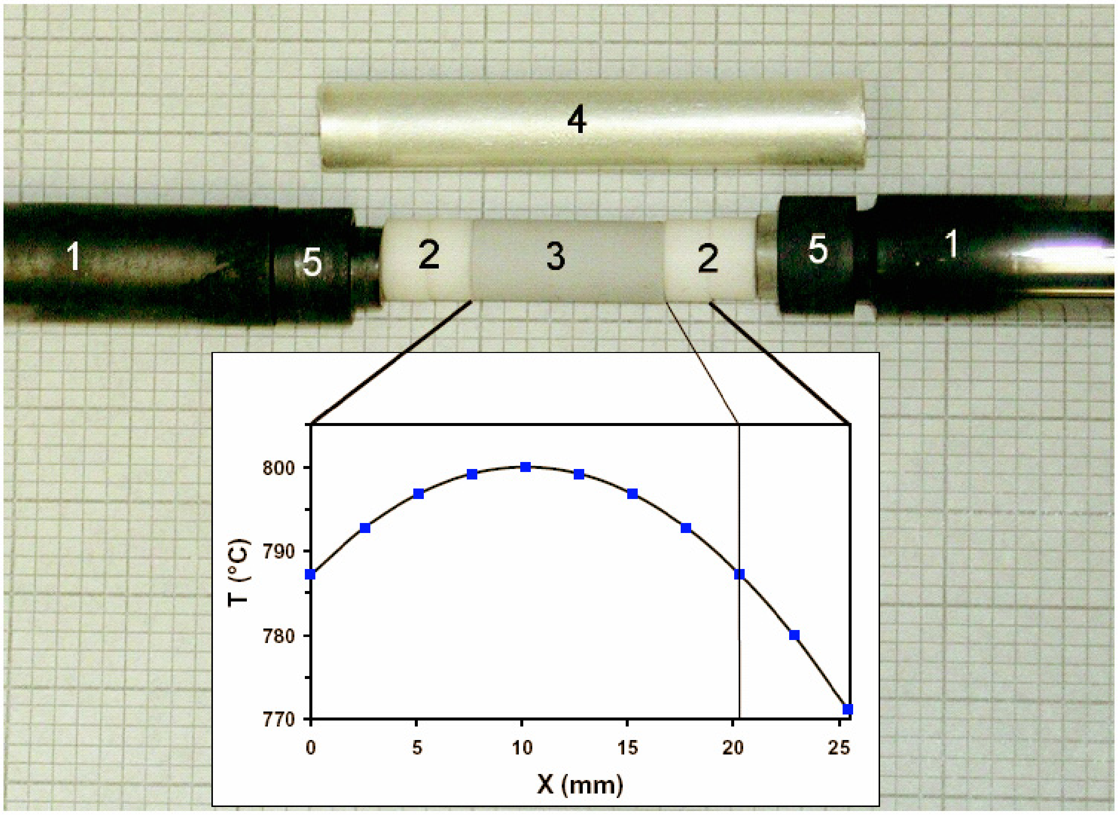

Figure 2. Sample assembly with temperature profile. Parts are: 1. WC pistons, 2. Al_2O_3 Spacers, 3. Sample, 4. Silver jacket, 5. WC sealing push rings. Temperature profile shows maximum temperature, T, at center of sample, and thermocouple measurement location between the 2 Al_2O_3 spacers on the right with the TC inserted through the piston and first spacer on the right.

calcite, periclase, and CO_2 (Goldsmith, 1959). Given that porosities of all starting materials are small, equilibrium CO_2 pore pressures (Figure 3) could be reached by dissociation of surficial traces of the dolomite samples. Equilibrium CO_2 pressures were taken from reaction equilibria for dolomite reported by Goldsmith (1959) and effective pressures, P_e, were determined by subtracting this equilibrium P_{CO2} from P_c ($P_e = P_c - P_{CO2}$).

Temperature was increased by way of an internal platinum wire resistance furnace and measured using an inconel-sheathed Chromel-Alumel thermocouple. The thermocouple was inserted along the center of one of the WC pistons and a hollow aluminum oxide spacer; temperatures were thus monitored in each experiment at one end of a solid aluminum oxide spacer, 4.8 mm from the specimen end. Calibrations of the temperature profile along the axis of a hollow sample and aluminum oxide spacers allow determination of the maximum temperature at the sample center from the temperature measured by the sheathed thermocouple in the aluminum oxide spacer. Temperatures at the thermocouple bead were controlled during experiments to within ±1°C. Temperatures reported for the experiments represent the highest temperature within the sample and the temperatures throughout the samples are within 1% of this value.

Samples were shortened at nearly constant axial strain rates ($1.5\text{x}10^{-7}$ to $1.2\text{x}10^{-4}$ s^{-1}) by way of the WC pistons, driven by a constant speed motor and screw-driven load system. Strains and strain rates were determined from transducer measurements of axial displacement ($l-l_o$) normalized by the original length, l_o. From the shapes and diameters

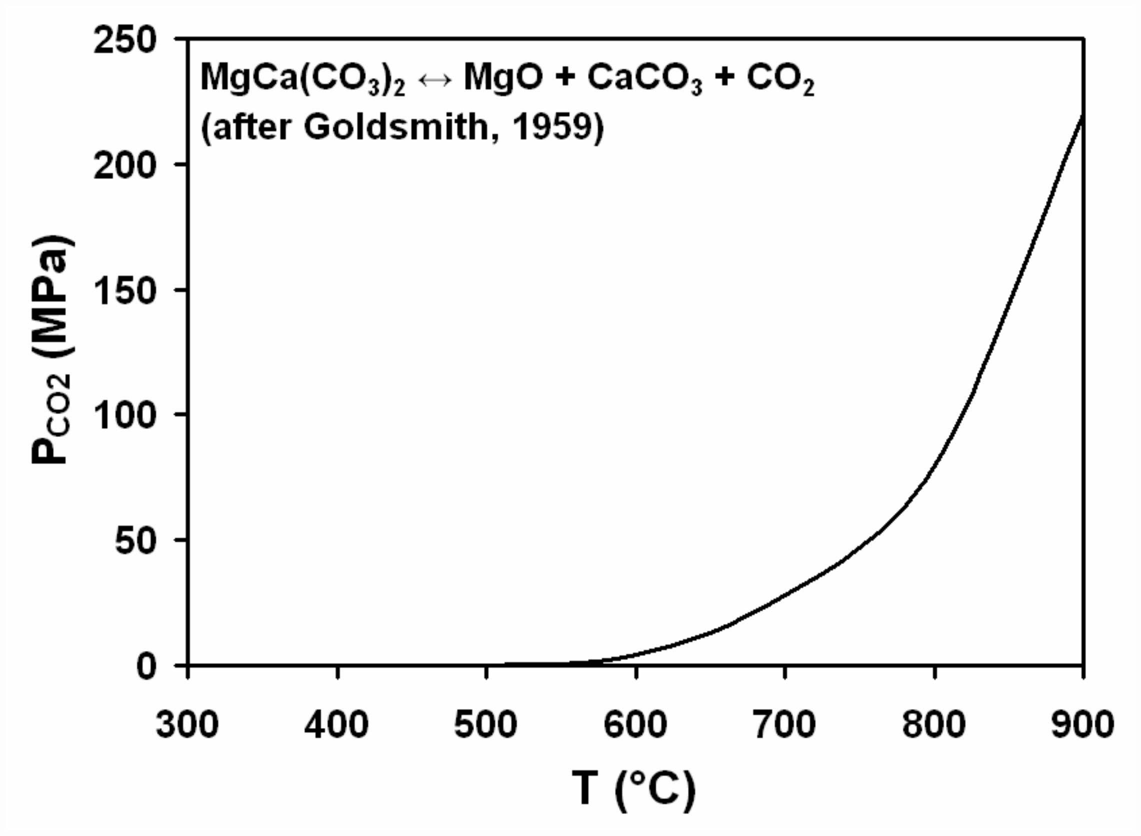

Figure 3. Thermal Dissociation equilibrium of confined dolomite (after Goldsmith 1959). Dissociation begins at approximately 560°C. When samples sealed into their jackets are heated beyond this temperature, dissociation generates a CO_2 pressure given by the equilibrium curve. Owing to negligible pore volumes, the volume fraction of dolomite that dissociates is very small.

of the deformed samples, and deformation microstructures, strains appear to be relatively homogeneous and uncertainties in local internal strains are probably small (±1%). Axial loads before and during triaxial compression were measured using an internal Heard-type force gauge and differential stresses (σ_1-σ_3) determined to within ±1 MPa.

The strain rates used are considerably faster than tectonic rates in the Earth (typically 10^{-12} to 10^{-15} s^{-1}). The common method of adjusting for this is to trade time for temperature, with an increase in temperature used to activate the same deformation mechanisms that are important in the earth at faster strain-rates. Extrapolations to natural strain-rates can then be made using flow laws, assuming similar differential stresses to activate the same mechanisms.

Grain growth in the natural dolomite starting materials is negligible at the temperatures imposed in the experiments reported here. However, grain growth was noted in the extremely fine-grained synthetic dolomite subjected to elevated temperatures. Thus, synthetic samples were annealed for 28 hrs at 800°C, P_c = 380 MPa to promote grain growth prior to each experiment, resulting in a mean grain size of ~2.5 μm. Following this initial annealing period, the confining pressure and temperature of the sample were adjusted to the desired deformation conditions, allowing 1-2 hours for thermal equilibration of the apparatus.

Stress-strain data were obtained for all of the dolomite starting materials by running individual constant strain-rate experiments at different effective pressures, strain rates, and temperatures. In addition, a series of constant strain-rate experiments were performed on individual samples, altering the strain rate in a stepwise manner or changing the temperature in a stepwise manner. Strain-rate-stepping experiments were performed by increasing strain rate by increments of a factor of 10 without unloading and redetermining the point of zero differential load. Temperature-stepping experiments were performed by reducing (and in some cases increasing) the temperature by 100°C, unloading the specimen between each temperature step in order to allow for thermal expansion and redetermining the "hit point" at which differential load becomes non-zero.

Buffered and amplified transducer signals for P_c, σ_1, and $(l-l_o)$ were monitored and recorded by way of a National Instruments data acquisition board and Labview software. Mechanical data are reported as differential stress $(\sigma_1-\sigma_3)$ versus axial strain (ε) with sample strains corrected for apparatus distortion. Corrections to differential stress $(\sigma_1-\sigma_3)$ were made for changing cross-section areas of samples during shortening, assuming that deformed samples remain cylinders of constant volume.

A mechanical steady state was not obtained in most of the experiments. Thus, strengths of dolomite at different conditions are tabulated and compared at the yield point and at a fixed strain ε of 5%. Comparisons of strength for different strain rates of strain-rate-stepping tests and for different temperatures of temperature-stepping tests were made at a common reference strain. Second-order polynomial fits were used to fit the observed strain hardening following yield for each step and differential stresses evaluated at the same strain value for the different strain rate or temperature conditions, extrapolating beyond measured values as little as possible (<3% in axial strain).

Thermally-activated flow laws with exponential and power relationships between strain rate and stress were compared with the mechanical data for the different dolomites and flow law parameters determined by least-squares fitting.

Microstructural Characterization

Deformation microstructures of selected samples deformed at different temperatures and strain rates were examined by optical microscopy in plane-polarized and cross-polarized light. Deformed samples were impregnated with epoxy resin, cut in half parallel to the compression axis and doubly-polished ultra-thin (~5 μm) sections prepared. The extent of microcracking was judged from plane-polarized light scattering and observations of mechanical twinning, undulatory extinction, deformation bands, and recrystallization were made in cross-polarized light.

RESULTS

Mechanical Response

The results of individual constant strain-rate experiments are listed in Table 4, results of strain-rate-stepping experiments are listed in Tables 5 & 6, and results of temperature-stepping experiments appear in Tables 7 & 8. A subset of selected stress-strain curves are used to illustrate the mechanical response of dolomite in the figures of this thesis and all stress-strain data obtained in this study appear in the Appendix, organized alphanumerically by sample number.

Compressive flow strengths of coarse-grained Madoc and Kern Mtns. dolomites are large over the experimental conditions tested (Figure 4A, B) and they compare well with mechanical data obtained previously (Figure 4C) for Dover Plains dolomite (Turner et al., 1954), Hasmark dolomite (Handin and Fairbairn, 1955) , and Crevola dolomite (Barber et al., 1994). Madoc and Kern Mtns. dolomite samples shortened at T = 400-850°C, P_e = 50-300 MPa, and $\dot{\varepsilon}$ = $1.2\text{x}10^{-7}$ to $1.2\text{x}10^{-5}$ s^{-1} begin to yield at differential stresses of 130-420 MPa, as marked by the departure in stress-strain data from linear elastic behavior. Thereafter, their stress-strain curves show considerable strain hardening with differential stress (σ_1-σ_3) reaching 400-685 MPa at ε = 5%, well above the applied effective pressures, P_e ($P_e = P_c$-P_p or $P_e = \sigma_3 - P_p$), and hardening coefficients h, defined as

$$h = \left. \frac{d(\sigma_1 - \sigma_3)}{d\varepsilon} \right|_{\dot{\varepsilon}} \quad (1)$$

of up to $3.4\text{x}10^3$ MPa (or an increase in strength of 34 MPa over 1% strain). Hardening

Table 4. Constant strain-rate experiments

	Sample	T (°C)	$\dot{\varepsilon}$ (s^{-1})	P_c (MPa)	P_e (MPa)^a	$(\sigma_1-\sigma_3)_y$ (MPa)^b	ε_y (%)^c	$(\sigma_1-\sigma_3)_{5\%}$ (MPa)^d	$h_{5\%}$ (10^2 MPa)^e	ε_f (%)^f
Madoc dolomite	MD33	400	1.25×10^{-5}	300	300	374	0.961	600	24	9.14
	MD35	400	1.25×10^{-5}	300	300	263	0.82	413**	18.046**	4.39*
	MD26	500	1.19×10^{-5}	300	300	400	1.01	642	27	7.4
	MD10	600	1.29×10^{-5}	305	300	365	1.1	650	34	7.98
	MD13	700	1.25×10^{-7}	330	300	403	1.29	596	25	7.26
	MD32	700	1.18×10^{-5}	330	300	422	1.21	684	26	7.78+
	MD27	700	1.27×10^{-5}	230	200	321	1.02	650	24	7.92
	MD39	700	1.25×10^{-5}	130	100	372	1.09	608	15	7.94*
	MD20	700	1.25×10^{-5}	80	50	131	0.39	317**	18**	3.54*
	MD25	700	1.35×10^{-4}	330	300	418	1.18	654	24	7.77*
	MD9	800	1.36×10^{-5}	380	300	326	1.22	523	-3	8.3*
	MD34	850	1.25×10^{-5}	400	200	267	1.58	397	2	8.75
Kern	KM1	500	1×10^{-5}	400	400	487	2	612	31	10.3
	KM3	700	1×10^{-7}	400	370	302	2.3	323	-4	11.5
	KM2	700	1×10^{-5}	400	370	352	1.96	502	4	12.8
Synthetic	SD A3-1	400	1.2×10^{-5}	300	300	775	1.71	875**	260**	2.1*
	SD B2-3	600	1×10^{-5}	305	300	638	1.64	842	155	5.16
	SD B3-1	700	1.2×10^{-5}	330	300	155	3.46	197	20	9.43
	SD B1-4	800	1.25×10^{-5}	380	300	0	0.05	0.3	0	9.25
Blair	BD-1	500	1×10^{-5}	400	400	636	1.3	765**	41**	3*
	BD-2	700	1×10^{-5}	400	370	466	2.4	567**	70**	3.7*

a. Assuming $P_e = P_c - P_p$ where $P_p = P_{CO2}$ at equilibrium

b. Differential stress at yield as defined by departure from linear σ - ε response

c. Axial strain at yield

d. Differential stress at 5% axial strain

e. Hardening coefficient at 5% axial strain

f. Final axial strain for experiment

* sample faulted at final strain

** Sample faulted prior to $\varepsilon = 5\%$, $(\sigma_1-\sigma_3)$ and h reported for ε_f

\+ piston bent during deformation

Table 5. Strain rate-stepping experiments coarse-grained dolomite

	Experiment	**$\dot{\varepsilon}$ (s^{-1})**	**$(\sigma_1\text{-}\sigma_3)_y$ (MPa)[b]**	**ε_y (%)[c]**	**$(\sigma_1\text{-}\sigma_3)_{sf}$ (MPa)[d]**	**h_{sf} (10^2 MPa)[e]**	**ε_{sf} (%)[f]**
Madoc dolomite	**Sample MD24 T = 600°C, Pc = 305 MPa, Pe = 300 MPa[a]**						
	MD24E7	$1.20x10^{-7}$	382	1.09	573	64	3.3
	MD24E6	$1.69x10^{-6}$	582	3.5	705	27	6.2
	MD24E5	$1.52x10^{-5}$	709	2.4	732	11	8.1
	MD24E4	$1.2x10^{-4}$	----	----	----	----	8.1[*]
	normalizing to $\dot{\varepsilon} = 1.69x10^{-6}$ at $\varepsilon = 5\%$						
	Sample MD21 T = 700°C, Pc = 330 MPa, Pe = 300 MPa[a]						
	MD21E6	$1.30x10^{-6}$	305	1.19	694	21	8.1
	MD21E5	$1.56x10^{-5}$	706	8.3	734	6	10.4
	MD21E4	$1.2x10^{-4}$	----	----	----	----	10.5[*]
	normalizing to $\dot{\varepsilon} = 1.30x10^{-6}$ at $\varepsilon = 8\%$						
	Sample MD30 T = 700°C, Pc = 330 MPa, Pe = 300 MPa[a]						
	MD30E7	$1.20x10^{-7}$	352	1.23	496	46	2.8
	MD30E6	$1.69x10^{-6}$	511	3	614	27	5.2
	MD30E5	$1.52x10^{-5}$	630	5.4	670	29	6.4
	MD30E4	$1.26x10^{-4}$	684	6.6	709	21	7.9[*]
	normalizing to $\dot{\varepsilon} = 1.69x10^{-6}$ at $\varepsilon = 5\%$						
	For $T \leq 700°C$ $\alpha = 0.079 \pm 0.001$ MPa^{-1}, $n = 49 \pm 7$						
	Sample MD28 T = 800°C, Pc = 380 MPa, Pe = 300 MPa[a]						
	MD28E6	$1.21x10^{-6}$	346	1.35	502	15	4.2
	MD28E5	$1.45x10^{-5}$	502	4.4	611	27	6
	MD28E4	$1.23x10^{-4}$	608	6.2	697	14	8.3[+]
	$\alpha = 0.046 \pm 0.008$ MPa^{-1}, $n = 26 \pm 6$, normalizing to $\dot{\varepsilon} = 1.45x10^{-5}$ at $\varepsilon = 5\%$						

a. Assuming $P_e = P_c - P_p$ where $P_p = P_{CO2}$ at equilibrium

b. Differential stress at yield for first step, or differential stress at 0.2% strain following stepwise change in strain rate

c. Axial strain at yield

d. Differential stress at end of strain rate step

e. Hardening coefficient at end of strain rate step

f. Final cumulative strain for strain rate step

* sample faulted at final strain

\+ piston bent during deformation

Table 6. Strain rate-stepping experiments fine-grained dolomite

	Experiment	$\dot{\varepsilon}$ (s^{-1})	$(\sigma_1-\sigma_3)_y$ (MPa)[b]	ε_y (%)[c]	$(\sigma_1-\sigma_3)_{sf}$ (MPa)[d]	h_{sf} (10^2 MPa)[e]	ε_{sf} (%)[f]
Synthetic dolomite	**Sample SD B1-3 T = 700°C, Pc = 330 MPa, Pe = 300MPa[a]**						
	B1-3E6	$1.33x10^{-6}$	309	4.17	413	6	7
	B1-3E5	$1.1x10^{-5}$	529	7.46	640	76	8.63
	B1-3E4	$1x10^{-4}$	697	8.89	720	121	9
	α = 0.023 ±0.03 Mpa^{-1}, n = 12 ±10, normalizing to $\dot{\varepsilon}$ = $1.1x10^{-5}$ at ε = 8.5%						
	Sample SD B1-2 T = 800°C, Pc = 380 MPa, Pe = 300MPa[a]						
	B1-2E5	$1.62x10^{-5}$	2.26	0.04	4	0	3.1
	B1-2E4	$1.62x10^{-4}$	9.4	3.44	20	1	7.2
	B1-2E5	$1.72x10^{-5}$	3.47	7.32	5	0	9.6
	B1-2E4	$1.61x10^{-4}$	11.9	9.96	32	4	13.9
	n = 1.28 ±0.15 , normalizing to $\dot{\varepsilon}$ = $1.6x10^{-5}$ at ε = 7% and ε = 13.8%						

a. Assuming $P_e = P_c - P_p$ where $P_p = P_{CO2}$ at equilibrium

b. Differential stress at yield for first step, or differential stress at 0.2% strain following stepwise change in strain rate

c. Axial strain at yield

d. Differential stress at end of strain rate step

e. Hardening coefficient at end of strain rate step

f. Final strain for strain rate step

Table 7. Temperature-stepping experiments coarse-grained dolomite

	Experiment	T (°C)	P_c (MPa)	P_e (MPa)[a]	$(\sigma_1\text{-}\sigma_3)_y$ (MPa)[b]	ε_y (%)[c]	$(\sigma_1\text{-}\sigma_3)_{sf}$ (MPa)[d]	h_{sf} (10^2 MPa)[e]	ε_{sf} (%)[f]
Madoc dolomite	**Sample MD12 $\dot{\varepsilon} = 1.25\text{x}10^{-5}\text{s}^{-1}$**								
	MD12T8	800	380	300	344	1.3	526	5	6.1
	MD12T7	700	380	350	517	6.34	655	11	9.3
	MD12T6	600	380	375	631	9.83	673	4	11.4
	normalized to T = 700°C at ε = 7%								
	Sample MD17 $\dot{\varepsilon} = 1.05\text{x}10^{-5}\text{s}^{-1}$								
	MD17T8	800	380	300	381	1.36	586	37	3.8
	MD17T7	700	330	300	560	3.68	699	42	5.6
	MD17T5	500	300	300	598	6.14	725	17	8.4
	normalized to T = 700°C at ε = 5%								
	Sample MD15 $\dot{\varepsilon} = 0.96\text{x}10^{-6}\text{s}^{-1}$								
	MD15T8	800	380	300	350	1.28	505	29	3.5
	MD15T7	700	330	300	496	3.34	631	44	5.4
	MD15T6	600	305	300	517	5.96	694	50	7.7
	normalized to T = 700°C at ε = 6%								
	For T ≤ 700°C, $(2.303R)*\Delta\log(\sigma_1\text{-}\sigma_3)/\Delta(1/T)$ = ~-2 kJ/mol **For T ≥ 700°C, $H^*/n \geq$ 13kJ/mol, $H^*/\alpha \geq$ 370 kJ/mol**								
Kern	**Sample KM4 $\dot{\varepsilon} = 1.25\text{x}10^{-5}\text{s}^{-1}$**								
	KM4T8	800	380	300	370	2	388	-14	7.4
	KM4T7	700	380	350	425	8.5	496	-1	11.3
	KM4T6	600	380	375	475	11.9	548	9	13.7*
	H^*/n = ~13 kJ/mol, normalized to T = 700°C at ε = 9%								

a. Assuming $P_e = P_c - P_p$ where $P_p = P_{CO2}$ at equilibrium

b. Differential stress at yield point of each temperature step

c. Axial strain at yield point of each temperature step

d. Differential stress at end of temperature step

e. Hardening coefficient at end of temperature step

f. Strain at end of temperature step

* sample faulted at final strain

Table 8. Temperature-stepping experiments fine-grained dolomite

	Experiment	T (°C)	P_c (MPa)	P_e (MPa)	$(\sigma_1\text{-}\sigma_3)_y$ (MPa)[d]	ε_y (%)	$(\sigma_1\text{-}\sigma_3)_{sf}$ (MPa)[d]	h_{sf} (10^2 MPa)[e]	ε_{sf} (%)
Synthetic dolomite	**Sample SD A1-1 $\dot{\varepsilon} = 1.63\text{x}10^{-4}\text{s}^{-1}$**								
	A1-1T8	800	380	300	--	--	5	0	4.5
	A1-1T7	700	330	300	449	6.64	577	4	9.3
	A1-1T6	600	305	300	667	9.75	717	195	10.1
	For T ≥ 700°C, H*/n = 218 ±35 kJ/mol, normalized to T = 700°C at ε = 9% **For T ≤ 700°C, (2.303R)*$\Delta\log(\sigma_1\text{-}\sigma_3)/\Delta(1/T)$ = ~-12 kJ/mol**								
	Sample SD B1-1 $\dot{\varepsilon} = 1.48\text{x}10^{-5}\text{s}^{-1}$								
	B1-1T8	800	380	300	18	0.3	19	0	8
	B1-1T7	700	330	300	26	8.23	166	24	13.8
	B1-1T6	600	305	300	428	15.1	597	15	18.1
	For T ≥ 700°C, H*/n = 218 ±35 kJ/mol, normalized to T = 800°C at ε = 13% **For T ≤ 700°C, (2.303R)*$\Delta\log(\sigma_1\text{-}\sigma_3)/\Delta(1/T)$ = ~-0 kJ/mol**								
	Sample SD B2-2 $\dot{\varepsilon} = 1.53\text{x}10^{-6}\text{s}^{-1}$								
	B2-2T7	700	330	300	10.8	0.26	31	7	3.6
	B2-2T6	600	305	300	502	4.93	710	16	4.5
	B2-2T5	500	300	300	746	7.83	867	66	8.9
	For T ≥ 600°C, H*/n = 218 ±35 kJ/mol, normalized to T = 500°C at ε = 7% **For T ≤ 600°C, (2.303R)*$\Delta\log(\sigma_1\text{-}\sigma_3)/\Delta(1/T)$ = ~1 kJ/mol**								

a. Assuming $P_e = P_c - P_p$ where $P_p = P_{CO2}$ at equilibrium

b. Differential stress at yield point of each temperature step

c. Axial strain at yield point of each temperature step

d. Differential stress at end of temperature step

e. Hardening coefficient at end of temperature step

f. Strain at end of temperature step

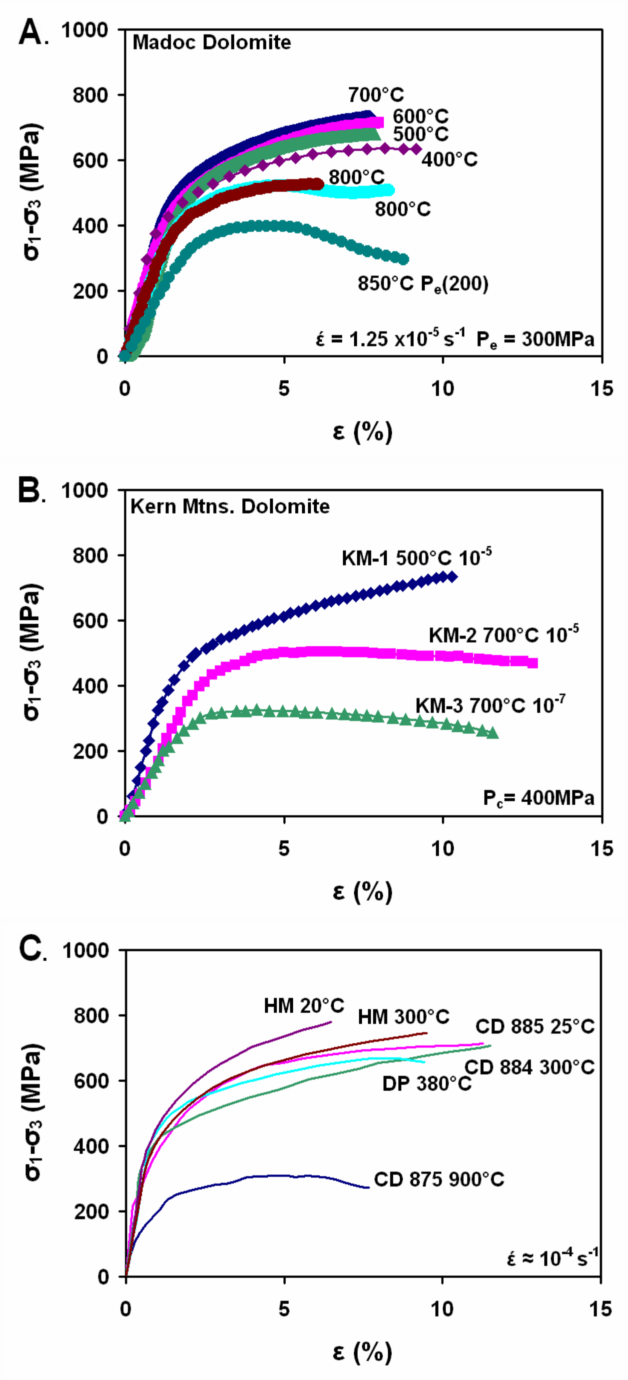

Figure 4. Stress-Strain plots for coarse-grained dolomites. A. Madoc Dolomite, (Samples MD32, MD10, MD26, MD33, MD12T8, MD9, MD34). B. Stress-strain data for Kern Mtns. Dolomite. C. Compilation of previous experiments, HM is Hasmark dolomite (Handin and Fairbairn, 1955), CD is Crevola dolomite (Barber et al., 1994), DP is Dover Plains dolomite (Turner et al., 1954).

is most pronounced at low temperatures ($T \leq 700°C$ for Madoc dolomite and $T < 700°C$ for Kern Mtns. dolomite). Limited strain hardening to strain weakening ($h < 0$) is observed for Madoc dolomite only at $T \geq 800°C$ (Figure 4A). Differential stresses determined are relatively constant with strain for Kern Mtns. dolomite at $T = 700°C$.

Compressive strengths of fine-grained synthetic and Blair dolomites (Figure 5) are somewhat larger than those of the coarse-grained dolomites (~25%) at low temperatures ($400° \leq T \leq 600°C$, $\dot{\varepsilon} = 10^{-5}\ s^{-1}$) and some failed by fracture soon after the onset of inelastic yielding. At $T < 700°C$ both fine-grained dolomites are very strong, with yield strengths of 630-775 MPa differential stress, while at $T \geq 700°C$ the strength drops dramatically, with yield stresses of 150 MPa and less for the synthetic dolomite, and only 470 MPa for Blair dolomite. Both fine-grained dolomites faulted at $T < 600°C$ at differential stresses of 875 MPa for synthetic dolomite and 765 MPa for Blair dolomite. The differential stress at failure is in excess of 2.5 times the P_e at failure for Blair dolomite, and nearly 3x P_e for the synthetic dolomite.

In sharp contrast to the low T deformation, the synthetic dolomite deforms at low differential stresses at higher temperatures ($T \geq 700°C$), with a yield strength of 150 MPa at 700°C and the yield was not detectable at 800°C. At 5% strain the differential stress of synthetic dolomite at 700°C reaches 200 MPa with a hardening coefficient, h, of 2×10^3 MPa, while at 800°C the synthetic dolomite appears to deform in a steady state manner, at a differential stress ≤ 1 MPa with an h of ~1 MPa.

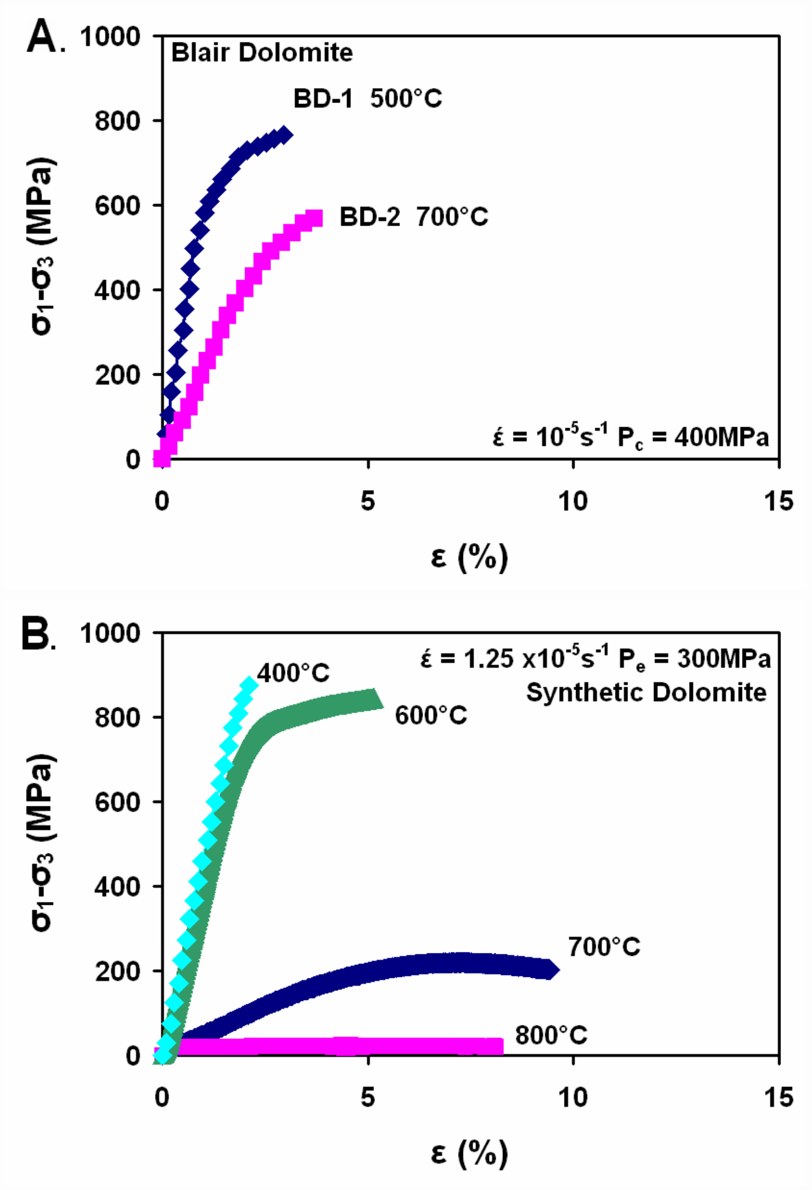

Figure 5. Stress-Strain plots for fine-grained dolomites. A. Blair dolomite prior to failure by fracture. B. Synthetic dolomite data (Samples SD A3-1, SD B2-3, SD B3-1, SD B1-1T8).

Pressure Dependence

Once differential stresses (σ_1-σ_3) reach values equal to or greater than P_e, stresses within polycrystalline rocks may locally be sufficient to initiate microcracking. Contributions of brittle, dilatant mechanisms of deformation to the total sample deformation can be assessed by determining the dependence of strength on effective pressure. Constant-strain-rate experiments were thus conducted on Madoc dolomite samples at constant temperature and strain rate (T = 700°C, $\dot{\varepsilon}$ = 1.25x10^{-5} s^{-1}) at different effective pressures, P_e, from 50 to 300 MPa (Figure 6A, Table 5). Stress-strain data at $100 \leq P_e \leq 300$ MPa are very similar with differential stresses at yield within 50 MPa of each other and stresses measured at $\varepsilon = 5\%$ within 11% of the value (σ_1-σ_3 = 684 MPa) measured at P_e = 300 MPa. The sample deformed at P_e = 50 MPa yielded at 131 MPa, just one-third the value (σ_1-σ_3 = 372 MPa) for the sample deformed at P_e = 100 MPa. The stress-strain curve for P_e = 50 MPa exhibits strain hardening, much as observed at higher pressures, but the experiment terminated when the sample failed at $\varepsilon = 3.5\%$ by shear fracture. The results, recast as (σ_1-σ_3) at $\varepsilon = 5\%$ versus effective pressure, P_e (Figure 6B) show that flow strengths at $P_e > 100$ MPa depend weakly upon effective pressure (with an internal coefficient of friction of μ^* of ~0.1) whereas differential stresses supported at $P_e < 100$ MPa may be described by a Mohr-coulomb criterion (with an internal coefficient of friction of μ^* of ~1.0). The weak dependence of flow strength on effective pressure at $P_e > 100$ MPa is confirmed by comparisons with previous results obtained for Dover Plains dolomite (Turner et al., 1954) and Hasmark

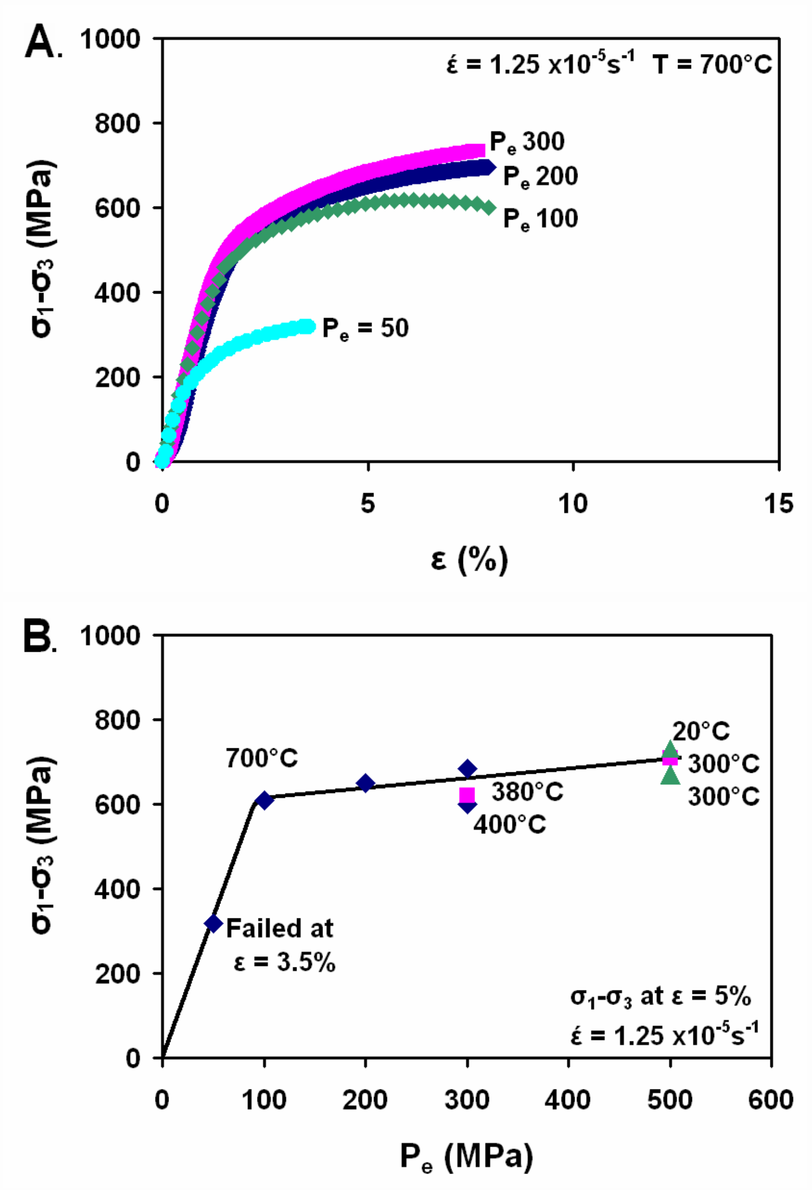

Figure 6. P_e effect on strength of coarse-grained dolomite. A. Stress-strain data for Madoc dolomite deformed at effective pressures, P_e, from 50 to 300 MPa. B. Differential stresses measured at 5% strain verses effective pressure. Madoc dolomite data at T = 700°C and $\dot{\varepsilon} = 1.25\text{x}10^{-5}$ s^{-1} are represented as diamonds. Dover plains data of Turner et al. (1954) are squares, and Hasmark dolomite of Handin and Fairbairn, (1955) are triangles. The Madoc sample deformed at P_e = 50 MPa failed at 3.5% strain.

dolomite (Handin and Fairbairn, 1955) at confining pressures up to 500 MPa (and lower temperatures).

The majority of constant strain-rate experiments in this study were performed at P_e = 300 MPa as determined from the applied confining pressure, P_c, and a pore pressure, P_p, assumed to equal the equilibrium P_{CO2} of dolomite (Goldsmith, 1959). Given the weak dependence of flow strength on P_e at high P_e any uncertainties in pore pressure, P_p are not likely to cause large variations in (σ_1-σ_3).

Strain Rate Dependence

Comparison of differential stresses measured for Madoc and Kern Mtns. dolomite specimens shortened at different strain rates for a given temperature and effective pressure (Table 4) show that strength does not change much with strain-rate over the experimental conditions. Strain-rate-stepping experiments were therefore performed to determine the dependence of flow strength on rate of deformation for individual specimens to eliminate sample-to-sample variations in strength (Tables 5 & 6).

Strain-rate-stepping experiments performed on coarse-grained dolomite samples exhibit small increases in strength at a given temperature and effective pressure associated with stepwise increases in strain-rate that are superposed on strain hardening (Figure 7A). To compare stresses achieved at different strain-rates, strain hardening curves were generated using second order polynomials and extrapolated, as necessary, to a common strain (~5%).

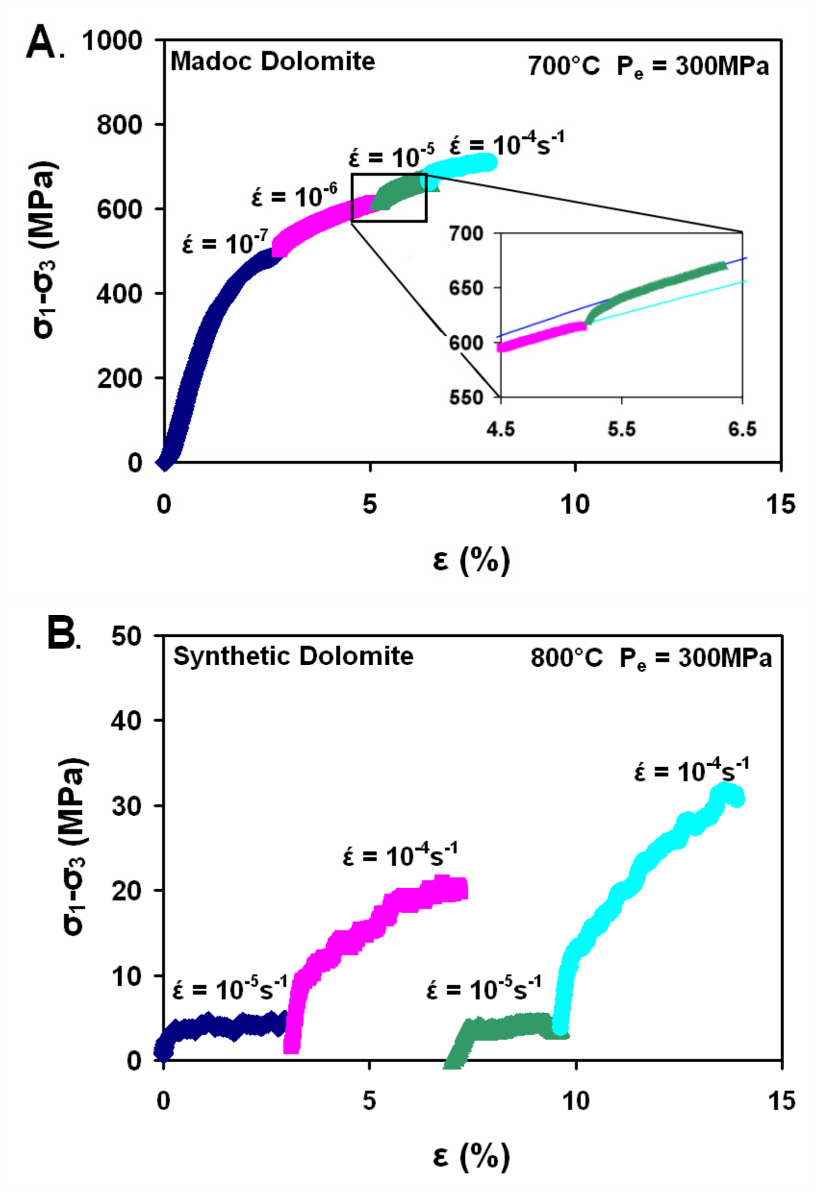

Figure 7. Strain-rate-stepping tests for Madoc and synthetic dolomites. A. Results for Madoc sample MD 30 deformed at 10^{-7} s^{-1} to 10^{-4} s^{-1}, reducing strain rate stepwise by orders of magnitude. The inset shows data in detail for a strain rate step from 10^{-6} s^{-1} to 10^{-5} s^{-1} and curves fit to the two strain rates. B. Results for fine-grained synthetic dolomite SD B1-2 deformed at $\dot{\varepsilon} = 10^{-5}$ s^{-1}, then at $\dot{\varepsilon} = 10^{-4}$ s^{-1}, returning to $\dot{\varepsilon} = 10^{-5}$ s^{-1}, and back to $\dot{\varepsilon} = 10^{-4}$ s^{-1}. Values for the faster rates were taken near the end of each step (~7 and 13% respectively).

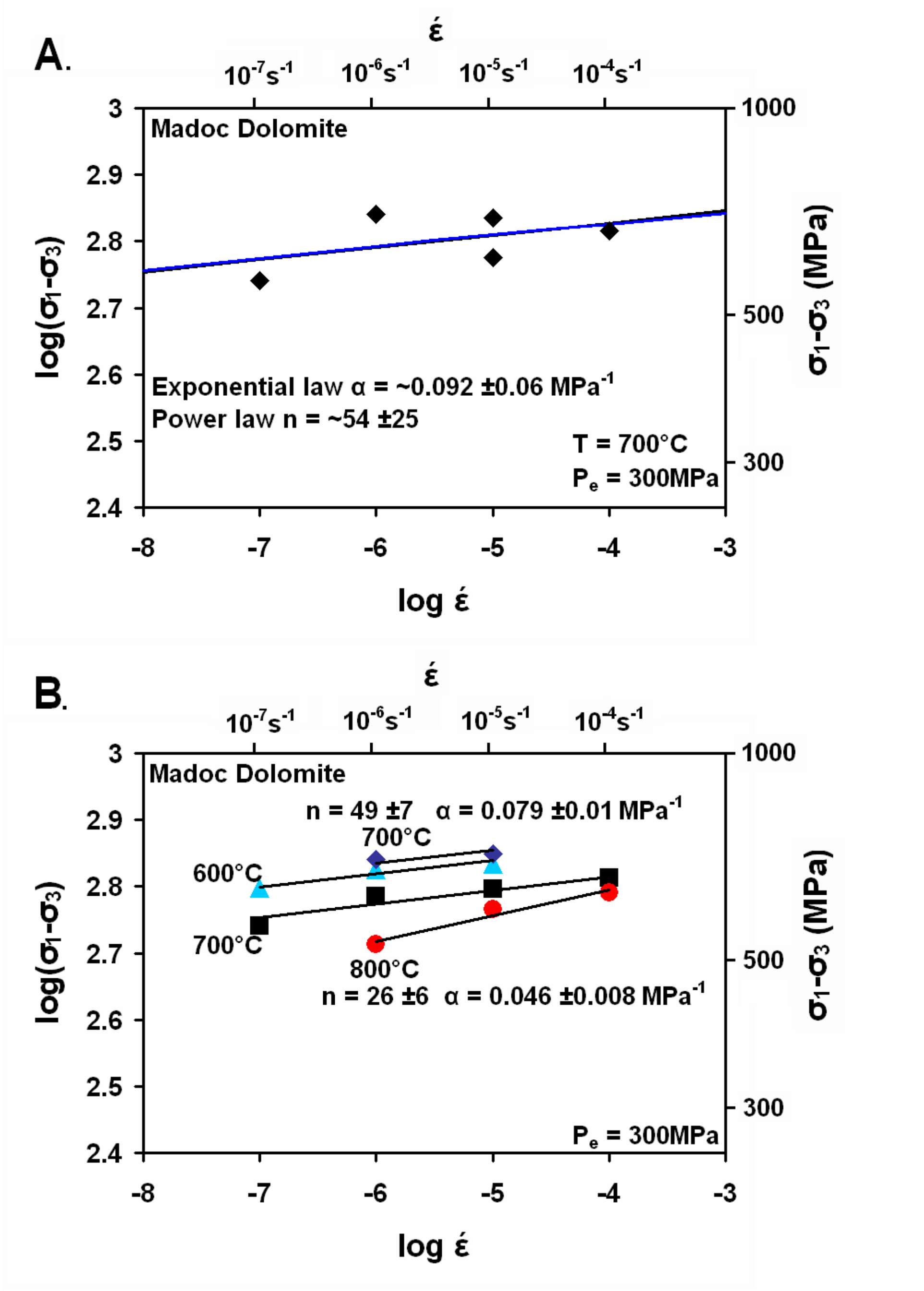

Figure 8. Log stress vs log strain rate for Madoc dolomite. A. Differential stress at ~5% strain for individual specimens deformed at different strain rates shows substantial scatter about best fits to the data. Best fits for exponential law and power law are superposed, shown as a line. (Samples MD30, MD21, MD13, MD32, MD25) B. Results of strain-rate-stepping experiments with best fits to their data using exponential and power laws. (Samples MD30, MD28, MD24, MD21)

The stress – strain rate relations determined from strain-rate-stepping experiments are comparable to those determined from individual experiments performed at different strain-rates, but with less scatter about least-squares fits. Recast as $\log(\sigma_1 - \sigma_3)$ versus $\log \dot{\varepsilon}$ (Figure 8A), stresses measured at $\varepsilon = 5\%$ for individual Madoc dolomite samples shortened at T = 700°C, $P_e = 300$ MPa show a weak positive correlation with strain rate. Similar stress – strain rate correlations are obtained for strain-rate-stepping experiments performed on Madoc dolomite (Figure 8B) at T = 600°C and T = 700°C but a slightly stronger rate dependence is observed at T = 800°C.

Strain-rate-stepping experiments performed on fine-grained synthetic dolomite samples reveal a weak dependence of flow strength on strain rate at T = 700°C ($P_e = 300$ MPa) and a much stronger dependence on strain rate at T = 800°C ($P_e = 300$ MPa). Changes in differential stress with stepwise changes in strain rate at T = 700°C were distinguished from changes in stress due to strain hardening in the same manner as for the coarse-grained dolomite results. However, strain hardening was not observed at the lower strain rates ($10^{-5}\,s^{-1}$) of the strain-rate-stepping test (Figure 7B) performed at T = 800°C (and $P_e = 300$ MPa; SD B1-2). Moreover, differential stresses measured at a given strain rate ($10^{-5}\,s^{-1}$) at T = 800°C appear to be reproducible at different finite axial strain values, and are apparently independent of prior triaxial deformation. Stress-strain rate relations for experiment SD B1-2 were determined from the relatively steady differential stress measurements made at $\dot{\varepsilon} = 10^{-5}\,s^{-1}$ and choosing the differential stress measured at the end of each high strain-rate ($10^{-4}\,s^{-1}$) step (at $\varepsilon = 4\%$ after initiating the $10^{-4}\,s^{-1}$ step).

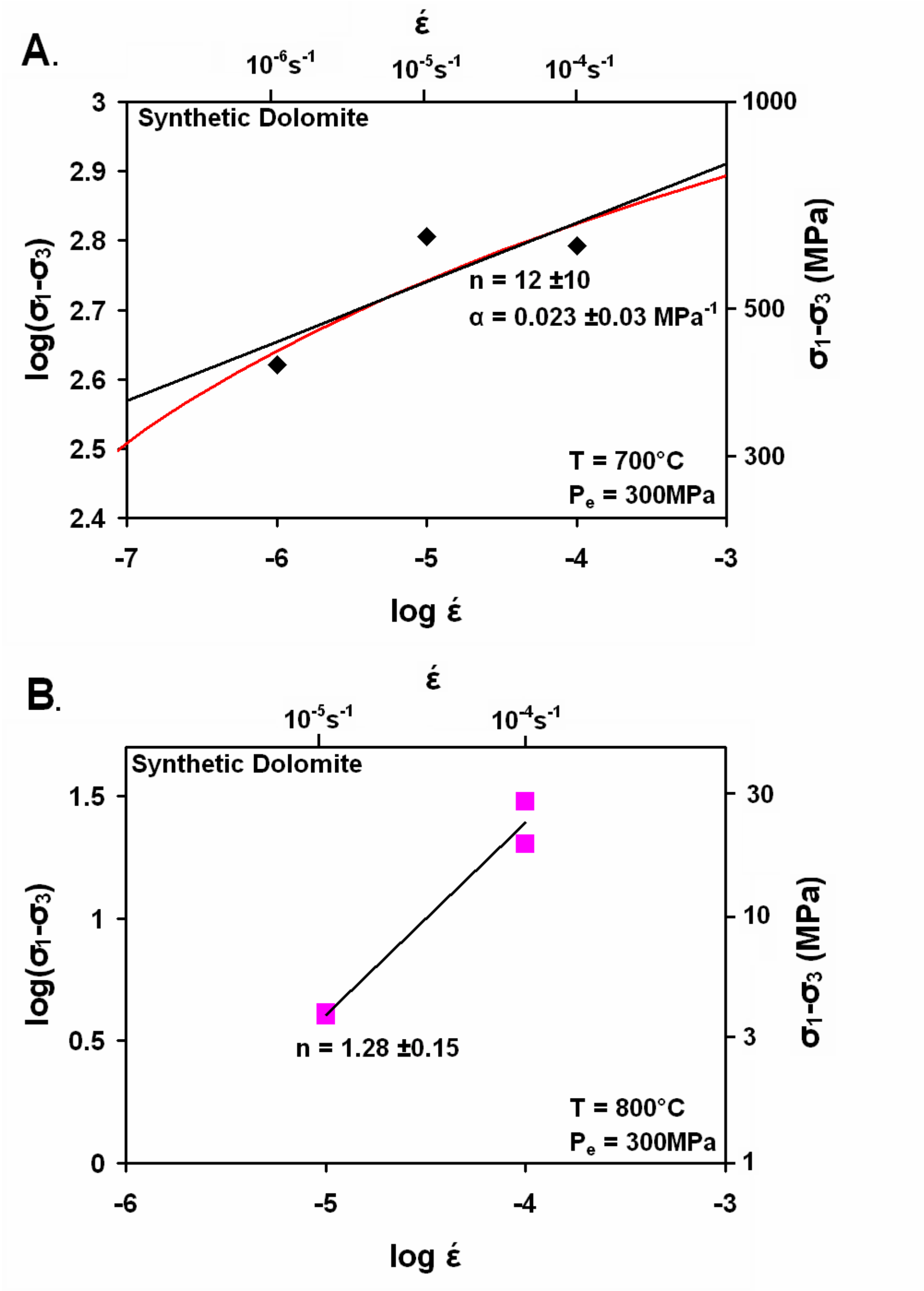

Figure 9. Log stress vs log strain rate for strain-rate-stepping experiments on synthetic dolomite. A. Strain-rate-stepping experiment (SD B1-3) at T = 700°C and P_e = 300MPa, with best fit exponential and power law fits shown. B. Strain-rate-stepping experiment (SD B1-2) at T = 800°C and P_e = 300MPa, fit by power law.

Results of strain-rate-stepping experiments displayed as log(σ_1-σ_3) versus log $\dot{\varepsilon}$ (Figure 9) show that flow strengths are weakly dependent on strain rate at T = 700°C and are strongly dependent on strain rate at T = 800°C. Flow strengths of fine grained dolomite at T = 700°C increase by 60% for an order of magnitude increase in strain rate, while at T = 800°C, differential stresses are 6 times larger for an increase in strain-rate of 10.

Temperature Dependence

The dependence of flow strength on temperature was determined for the coarse- and fine-grained dolomites from individual constant strain rate experiments (Table 4) and temperature-stepping experiments (Tables 7 & 8). Differential stresses measured at ε = 5% at different temperatures and a given strain rate and effective pressure require several stress-temperature relations.

Coarse-grained Madoc dolomite samples deformed at $T \leq 700$°C show a remarkable stress temperature relationship with differential stresses reaching higher values at higher temperatures (Figure 4A). While the increase in strength with temperature is small (~35 MPa for a temperature increase of 100°C), it is systematic and cannot be accounted for by sample-to-sample scatter (± 20 MPa). This relationship is inconsistent with simple, thermally activated deformation processes and cannot be described by an Arrhenius relationship.

In contrast to the lower temperature results, stresses measured for Madoc dolomite samples at temperatures $T > 700$°C show a marked reduction in strength with increasing temperature. At a strain rate of $\dot{\varepsilon} = 10^{-5}\ s^{-1}$ and $P_e = 300$ MPa, differential stresses measured at $\varepsilon = 5\%$ drop from 684 MPa at 700°C to 523 MPa at 800°C. The differential stress measured at $\varepsilon = 5\%$, $T = 850°C$, and $\dot{\varepsilon} = 10^{-5}\ s^{-1}$ was only 397 MPa Because of the high equilibrium P_{CO2} generated at $T = 850°C$ and the confining pressure, P_c, limit of the pressure vessel, the effective pressure, P_e, of the experiment performed at $T = 850°C$ (experiment MD 39) was only 200 MPa. However, based on determinations of P_e (Figure 6), the reduction in differential stress at this temperature is attributed largely to thermally activated processes, not to the departure in P_e from 300 MPa as imposed in the other experiments.

Temperature-stepping experiments for Madoc dolomite reveal stress-temperature relations like those determined for individual experiments at different temperatures. Normalizing to a common axial strain using second-order polynomial fits to stress-strain curves of temperature-stepping experiments (Figure 10A), differential stresses are relatively insensitive to temperature at $T \leq 700°C$ whereas $(\sigma_1\text{-}\sigma_3)$ measured at $T = 800°C$ are distinctly lower than at $T \leq 700°C$.

Differential stresses measured at different temperatures for coarse-grained Kern Mtns. dolomite do not show the distinct stress-temperature relations observed for Madoc dolomite. However, this may be due to the relatively small number of experiments performed on this starting material. Comparisons of individual experiments performed at $T = 500°C$ and 700°C (Figure 4B) at $\dot{\varepsilon} = 10^{-5}\ s^{-1}$ and $P_c = 400$ MPa ($P_e = 400$ and 370 MPa, respectively for KM1 and KM2) reveal a significant drop in strength with increased temperature and a change from strain hardening to a stress-strain curve characterized by a steady stress at $\varepsilon > 5\%$. A somewhat smaller temperature dependence

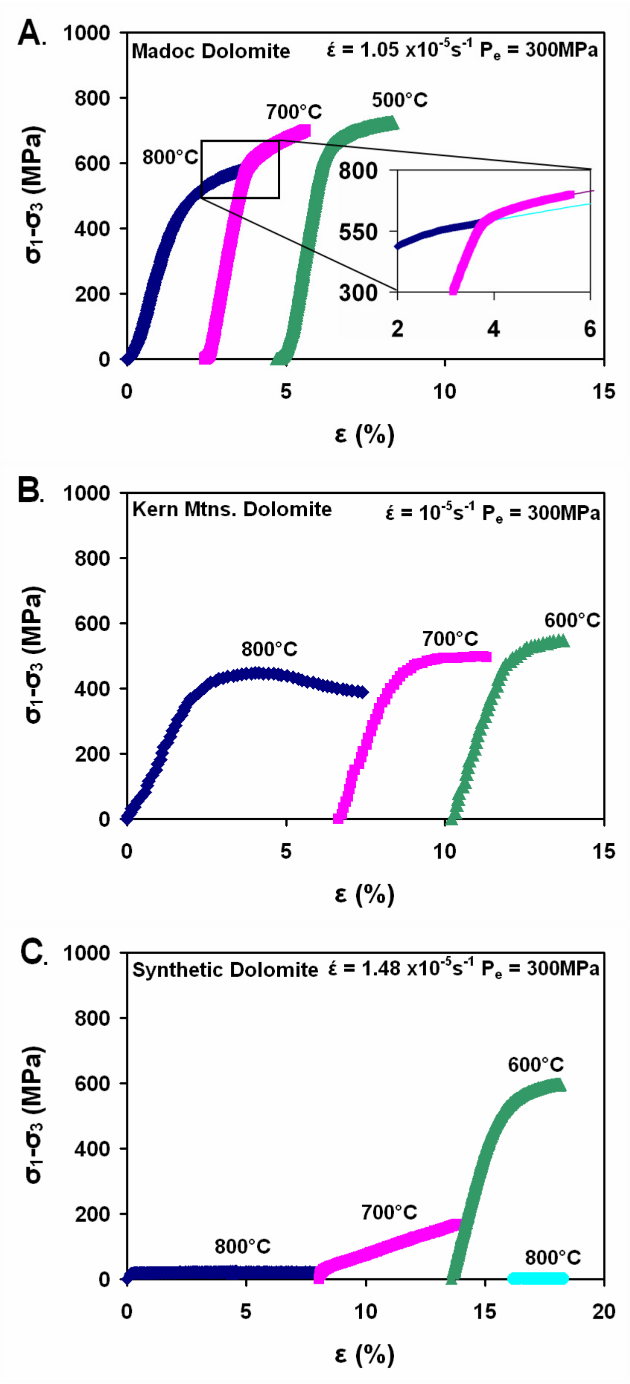

Figure 10. Results of temperature-stepping experiments. A. Series of stress-strain curves for Madoc dolomite (MD17). Inset shows the fit to strain hardening data at T = 800°C and 700°C, used to separate temperature dependence from strain dependence. B. Series of stress-strain curves for Kern Mtns. dolomite (KD-4) C. Temperature-stepping results for synthetic dolomite (SD B1-1).

is apparent from temperature-stepping results on Kern Mtns. dolomite at T = 600° and 700°C (Figure 10B) and a stronger temperature dependence is apparent at T = 700° and 800°C.

Fine-grained synthetic and natural Blair dolomites are very strong at low temperatures (T <700°C, Figure 5) with differential stresses at ε = 5% (or at fracture) that exceed coarse-grained dolomite strengths by 18-35% and show little variation with temperature. At high temperatures (T ≥ 700°C), however, stresses measured for synthetic dolomite are low and show a strong temperature dependence. Differential stresses measured at T = 700°C in individual constant strain-rate experiments (Figure 5B) and temperature-stepping experiments (Figure 10C) performed on synthetic dolomite are less than 30% of the stresses measured at T = 600°C at comparable $\dot{\varepsilon}$ and P_e. Differential stresses measured for synthetic dolomite (~4 MPa) at T = 800°C, $\dot{\varepsilon} = 10^{-5}\ s^{-1}$, and P_e = 300 MPa are just resolvable using the internal force gauge (±1 MPa). Temperature-stepping experiments (experiment SD B1-1, Figure 10C) further demonstrate that the low strength of synthetic dolomite at high temperature (T = 800°C) is reproducible, independent of earlier temperature steps at low temperature (T = 600°C).

The different dependencies of flow strength on temperature can be distinguished in terms of $\log(\sigma_1\text{-}\sigma_3)$ and 1/T, where T is absolute temperature, compiling results for coarse-grained dolomites (Figure 11) and for fine-grained dolomites (Figure 12).

$\mathrm{Log}(\sigma_1\text{-}\sigma_3)$ - 1/T data for Madoc dolomite define a relationship at low temperatures (T ≤ 700°C) with a shallow, negative slope, both for independent constant-strain-rate experiments (Figure 11A) and for temperature-stepping experiments (Figure

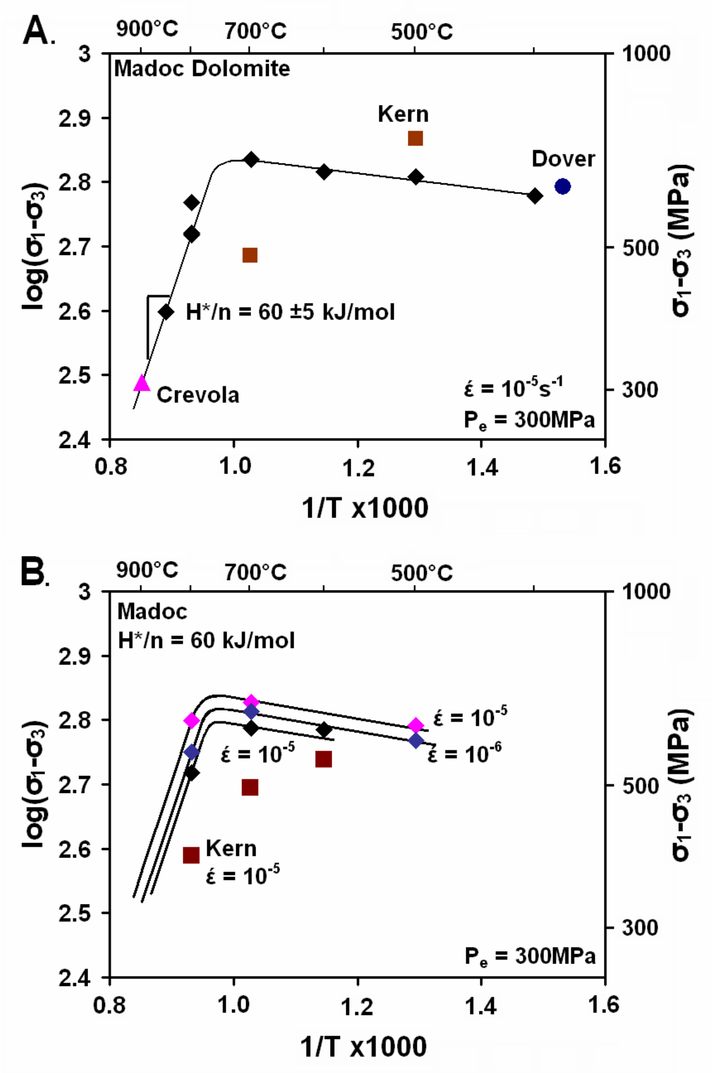

Figure 11. Strength of Madoc dolomite as a function of temperature, shown as log(σ_1-σ_3) versus 1/T. A. Results of individual experiments performed at P_e = 300MPa and strain rates of 10^{-5} s^{-1}. In addition to Madoc dolomite results (diamonds), results are shown for other coarse-grained dolomites (Kern, squares; Crevola, Barber et al. 1994, triangle; Dover, Turner et al. 1954, circle). At low temperatures, strengths are not sensitive to temperature, with a slight increase in strength with an increase in temperature. At temperatures above 700°C, strengths are strongly dependent on temperature with an apparent ratio of flow law parameters H^*/α = 24 kJ MPa/mol if an exponential $\sigma - \dot{\varepsilon}$ relationship is assumed, or a ratio H^*/n = 60 kJ/mol if a power law is assumed. B. Temperature-stepping results for $\dot{\varepsilon} = 10^{-6}$ s^{-1} (MD15), and $\dot{\varepsilon} = 10^{-5}$ s^{-1} (MD17 , MD12) for Madoc dolomite (diamonds). The same transition in slope is apparent in these results as obtained by compiling results of individual constant-strain-rate experiments. Temperature-stepping results for Kern Mtns. dolomite are shown for comparison (squares, KD-4).

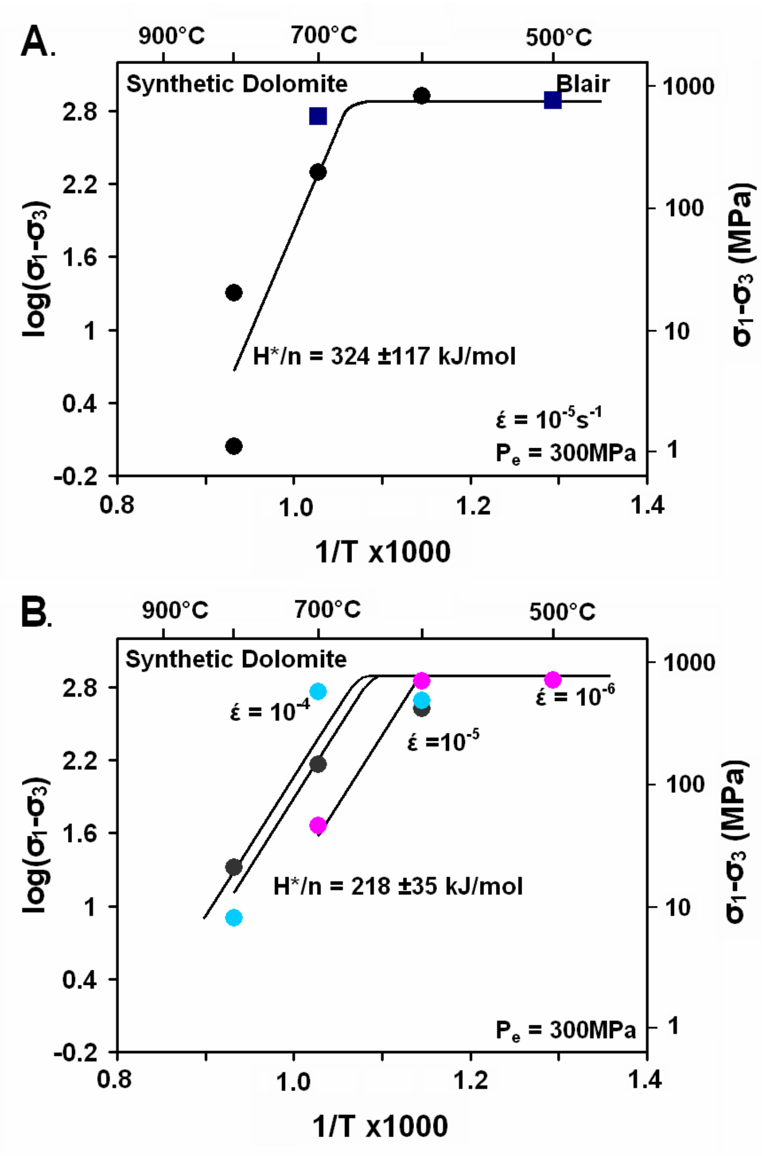

Figure 12. Strength of fine-grained synthetic dolomite as a function of temperature, shown as $\log(\sigma_1-\sigma_3)$ versus 1/T. A. Results of individual experiments performed at P_e = 300 MPa and $\acute{\varepsilon} = 10^{-5}\,s^{-1}$. In addition to synthetic dolomite results (circles, SD B1-1T8, B2-3, B3-1, B1-4), results are shown for fine-grained Blair dolomite (squares, BD-1, BD-2). At low temperatures, strengths of the fine-grained dolomites are insensitive to temperature and comparable, or slightly higher by 20%, to those of the coarse-grained dolomites. At temperatures above 600°C, strengths are strongly dependent on temperature with a slope given by H*/n = 324 ±117 kJ/mol. B. Temperature-stepping results for $\acute{\varepsilon} = 10^{-4}$ (SD A1-1), $\acute{\varepsilon} = 10^{-5}$ (SD B1-1), and $\acute{\varepsilon} = 10^{-6}$ (SD B2-2) for synthetic dolomite. The same transition in slope is apparent in these results as obtained by compiling results of individual constant strain-rate experiments, with a slope given by H*/n = 218 ±35 kJ/mol.

11B). Madoc dolomite strengths at low temperatures compare favorably with the strength of Kern Mtns. dolomite measured at T = 500° and 600°C and that reported for Dover Plains dolomite at T = 380°C ($\dot{\varepsilon}$ = 10^{-4} s^{-1}, and P_c = 500 MPa, Turner et al.,1954). The strength of Kern Mtns. dolomite at T = 700°C, $\dot{\varepsilon}$ = 10^{-4} s^{-1}, P_e = 370 MPa, appears to be low relative to Madoc dolomite results. Log(σ_1-σ_3) - 1/T data for Madoc dolomite at T = 800° and 850°C define a relationship at high temperatures with a steep, positive slope that is consistent with the flow strength reported for Crevola dolomite at T = 900°C ($\dot{\varepsilon}$ = 10^{-4} s^{-1}, P_c = 500 MPa, Barber et al., 1994). Given that the transition in stress-temperature relationships occurs between T = 700° and 800°C, the slopes evaluated at high temperatures of the temperature-stepping experiments are considered to be lower bounds of the high temperature stress-temperature relationship. Temperature-stepping results for Kern Mtns. dolomite (Figure 11B) appear to give a constant slope in terms of log(σ_1-σ_3) - 1/T. However, given the available data, two stress-temperature relationships might fit Kern Mtns. dolomite results with slopes similar to those of Madoc dolomite, if the transition temperature for Kern Mtns. dolomite is lower (between T = 600° and 700°C).

Differential stresses measured for synthetic and Blair dolomite at low temperatures (T < 700°C) are large and appear to be independent of temperature as illustrated in log(σ_1-σ_3) - 1/T plots for individual constant strain-rate experiments (Figure 12A) and temperature-stepping experiments (Figure 12B). At higher temperatures (T ≥ 700°C), however, log(σ_1-σ_3) - 1/T plots show a very strong stress-temperature relationship for both individual constant-strain-rate experiments (Figure 12A) and temperature-stepping experiments (Figure 12B). The $\log(\sigma_1\text{-}\sigma_3)$ - 1/T slope obtained from the individual constant strain-rate experiments is 5 times steeper than for the coarse-grained individual constant strain-rate experiments, while fine-grained temperature-stepping experiments indicate a slope up to 16 times steeper than the coarse-grained temperature-stepping experiments. However, the transition between low and high temperature behavior occurs between T = 700° and 800°C, suggesting that the slope for the coarse-grained stepping experiments may well be steeper, and more similar to the results from the individual experiments. If the high temperature portion of the coarse-grained temperature-stepping experiments is similar to the individual condition experiments, the slope difference is reduced to 3.6 times steeper.

Additionally, the transition from the low temperature behavior in $\log(\sigma_1\text{-}\sigma_3)$ - 1/T space to high temperature behavior in the synthetic is strain-rate dependent, with the transition occurring around 700°C at $\dot{\varepsilon} = 10^{-4}\ \mathrm{s}^{-1}$ and $10^{-5}\ \mathrm{s}^{-1}$ but the transition is closer to 600°C at $\dot{\varepsilon} = 10^{-6}\ \mathrm{s}^{-1}$. Thus, the transition in temperature dependence is distinctly different for synthetic and Madoc dolomites.

Microstructures

Optical deformation microstructures of coarse-grained Madoc and Kern Mtns. dolomites differ for samples deformed at low temperatures ($T \leq 700$°C) and high stresses and those deformed at high temperatures ($T \geq 800$°C) and lower stresses (Figure 13). Coarse-grained dolomite samples deformed at low temperatures exhibit *f*-twins (Figure 13C) with densities that exceed those observed in the starting materials (Figure 13A) and undulatory extinction. Optically visible subgrains are absent and there is no evidence of

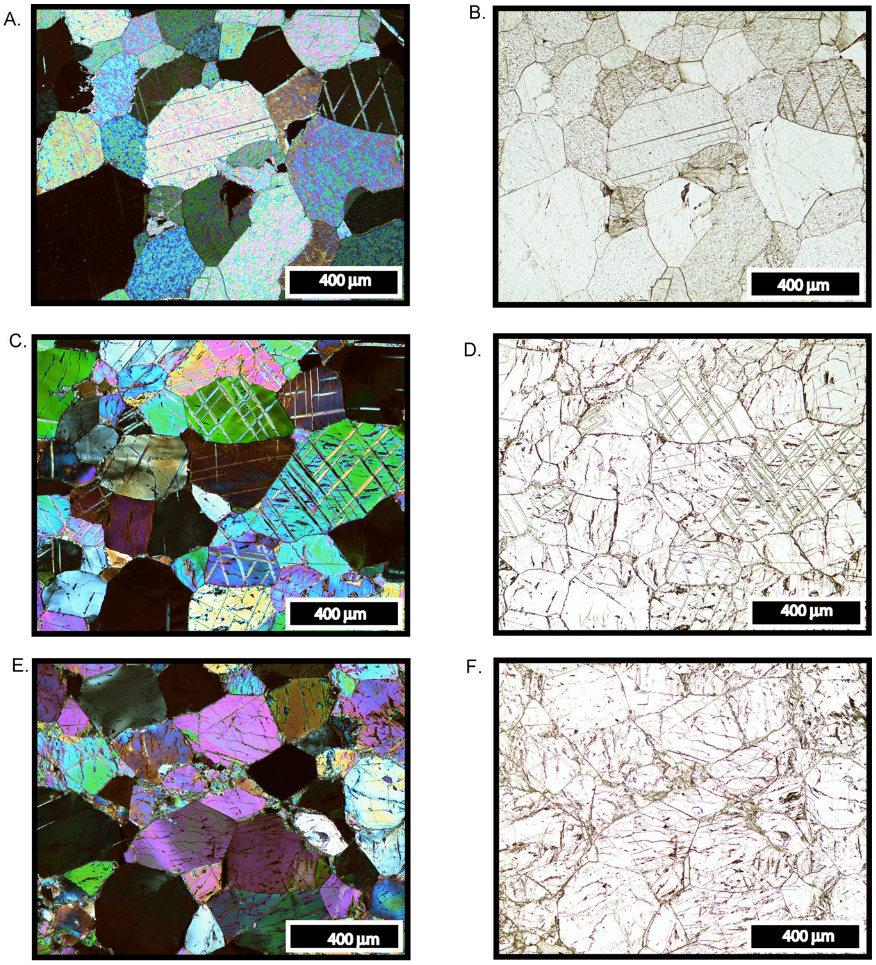

Figure 13. Optical microstructures of Madoc Dolomite. Cross-polarized light (A, C, E) and plane-polarized light (B, D, F). Maximum shortening direction is vertical in deformed samples (C-F). A. & B. Madoc dolomite prior to deformation. Individual grains show straight extinction, low twin densities (A.), and low intergranular crack densities (B.) C. & D. Madoc dolomite deformed at T = 700°C to $\varepsilon = 7.8\%$ (P_e = 300MPa, $\dot{\varepsilon} = 1.18\text{x}10^{-5}\text{s}^{-1}$, MD32). Sample is dominated by mechanical f-twins and undulatory extinction (C.), while intergranular crack densities are low (D.). E. & F. Madoc dolomite deformed to $\varepsilon = 8.8\%$ at 850°C (E., F., P_e = 200MPa, $\dot{\varepsilon} = 1.25\text{x}10^{-5}\text{s}^{-1}$, MD34). Microstructures include undulatory extinction, fine recrystallized grains at grain boundaries with twin densities that are comparable to that in the starting material (E.). Crack densities are somewhat greater than observed in the starting material (F.).

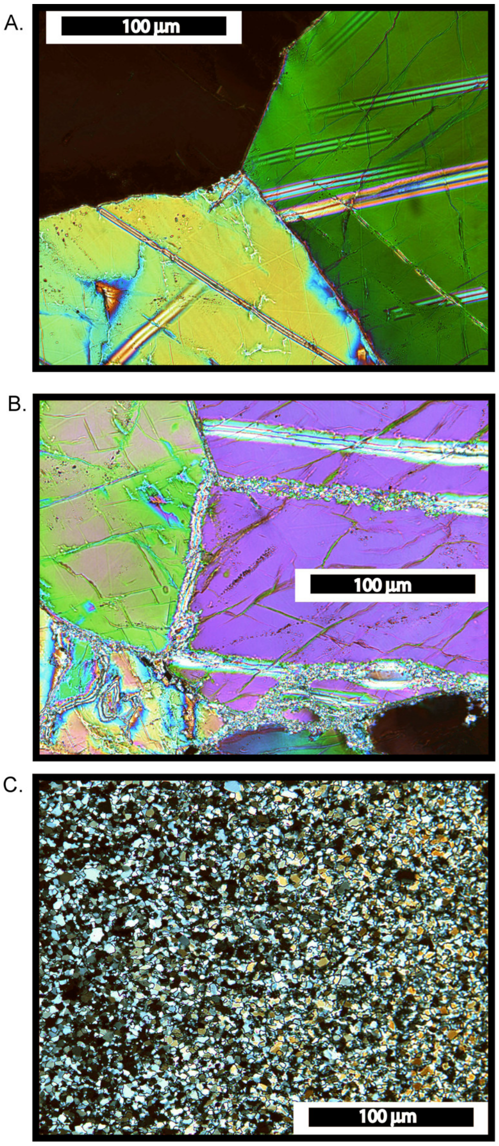

Figure 14. Optical grain boundary microstructures in crossed polarized light. A. MD32 deformed to $\varepsilon = 7.8\%$ at 700°C ($P_e = 300$MPa, $\dot{\varepsilon} = 1.18\text{x}10^{-5}\text{s}^{-1}$). B. MD34 deformed to $\varepsilon = 8.8\%$ at 850°C ($P_e = 200$MPa, $\dot{\varepsilon} = 1.25\text{x}10^{-5}\text{s}^{-1}$). C. SD B1-4 deformed to $\varepsilon = 9.25\%$ at 800°C ($P_e = 300$MPa, $\dot{\varepsilon} = 1.25\text{x}10^{-5}\text{s}^{-1}$). Grain boundaries of Madoc dolomite deformed at $T \leq 700$°C are straight and sharply defined, much as observed for the starting material. In contrast, grain boundaries following deformation at $T \geq 800$°C are decorated by fine recrystallized grains. Recrystallization is also noted within grains, particularly at twins and zones that may have involved shear and/or cracking. Grain boundaries and intragranular microstructures of deformed synthetic dolomite samples appear little changed from those of the HIP starting material. The shortening direction is vertical in all micrographs.

recrystallization, either at grain boundaries or in twins (Figure 14A). Despite the large differential stresses (σ_1-σ_3) achieved at the lower temperatures, relative to the effective pressure, P_e, samples imaged in plane polarized light show little scattering of light due to microcracks (Figure 13D) over that observed for the starting materials (Figure 13B).

Coarse-grained dolomite samples deformed at higher temperatures (T = 800, 850°C at $\dot{\varepsilon} = 10^{-5}\ s^{-1}$, and $P_e = 300$, 200 MPa, respectively) have twin densities (Figure 13E) similar to the starting materials (Figure 13A). Individual dolomite grains show smooth undulatory extinction and fine recrystallized grains are observed at grain boundaries and within grains, localized on twins and deformation zones that may have involved shear and/or cracking (Figure 14B). Some of the light scattering noted in plane polarized light for these samples may be due to microcracks but some scattering appears to be due to plucking of the thin section where finely recrystallized grains are abundant (Figure 13F).

Optical microstructures of fine-grained synthetic and Blair dolomite appear unchanged by deformation, except for the macroscopic brittle shear fractures that formed in some of the samples. In contrast to the coarse-grained dolomites deformed at low temperatures, deformed fine-grained dolomites do not exhibit any twins that are optically detectible. Undulatory extinction is also not observed for the fine-grains of deformed synthetic dolomite (Figure 14C) and Blair dolomite samples. However, dislocation nucleation and glide cannot be ruled out for these samples since optical methods to detect distortions of the fine grains of these samples are not very sensitive. For fine-grained dolomite samples with no visible faults, shortening strains of up to 18%

must be accounted for, despite the lack of optical deformation microstructures (e.g., sample SD B1-1, Table 8).

Flow Laws

Coarse- and fine-grained dolomites deformed at low temperatures (T ≤ 600°C at $\dot{\varepsilon} = 10^{-5}\ s^{-1}$, $P_e = 300$ MPa) exhibit mechanical behavior that is nearly plastic, with differential stresses (at yield and at $\varepsilon = 5\%$) that increase little with increases in strain-rate. Differential stresses of coarse-grained Madoc dolomite deformed at these conditions exhibit a small dependence on temperature that cannot be described by an Arrhenius relation and stresses measured for the fine-grained dolomites show little or no dependence on temperature. Deformation microstructures corresponding to this mechanical response indicate that the high stresses measured at these conditions reflect the critical resolved shear stresses for mechanical twinning and dislocation slip in the coarse polycrystalline dolomites and, by inference, dislocation slip in the fine-grained dolomites. Local microcracking may play an accommodating role in plastic deformation but the relatively modest microcrack densities cannot account for large fractions of the total accumulated strains. The observed strain hardening and the lack of a strong temperature effect on mechanical properties suggest that dislocation recovery is limited, and this is consistent with the absence of optically visible subgrains or recrystallized grains.

To describe the high crystal-plastic flow strengths of polycrystalline dolomites at these low temperature conditions, I use two non-linear relationships between strain-rate, $\dot{\varepsilon}$, and stress, $(\sigma_1\text{-}\sigma_3)$, assuming that any thermal activation terms are negligible:

$$\dot{\varepsilon} = \dot{\varepsilon}_o \left(\frac{\sigma_1 - \sigma_3}{\mu} \right)^n \tag{2}$$

and

$$\dot{\varepsilon} = \dot{\varepsilon}_o \exp[\alpha(\sigma_1 - \sigma_3)] \tag{3}$$

where the pre-exponential terms $\dot{\varepsilon}_o$ in eqns. 2 and 3 are in units of strain-rate (s^{-1}), (σ_1-σ_3) is taken at ε = 5%, μ is the shear modulus (45.7 GPa; Bass, 1995), and parameters *n* (dimensionless) and α (MPa^{-1}) are fitting parameters, respectively, of the assumed power and exponential laws. Fits of the power law (eqn. 2) to experimental data yield a value of n that can be compared with idealized mechanical relations for viscous ($n = 1$) and plastic ($n = \infty$) response. However, micromechanical models suggest that an exponential form (eqn. 3) of the flow law best describes dislocation glide (Poirier, 1985).

Mechanical results for coarse-grained Madoc dolomite were plotted as log(σ_1-σ_3) versus $\log \dot{\varepsilon}$ (Figure 8) and least-squares methods used to find values of *n*,

$$\left(\frac{\Delta \log(\sigma_1 - \sigma_3)}{\Delta \log \dot{\varepsilon}} \right) = 1/n \tag{4}$$

while plots of (σ_1-σ_3) versus log $\dot{\varepsilon}$ and least-squares methods were used to find best values of *α*

$$\left(\frac{\Delta(\sigma_1 - \sigma_3)}{\Delta \log \dot{\varepsilon}} \right) = \frac{2.303}{\alpha} \tag{5}$$

The power and exponential laws fit the experimental measurements equally well, with values of $n = \sim 54$ (±30) or $\alpha = \sim 0.092$ (±0.059) MPa^{-1} describing the results of individual strain-rate experiments at T = 700°C and P_e = 300 MPa (Figure 8A) and values of n = ~49 (±7) or α = ~0.076 (±0.01) MPa^{-1} describing strain-rate-stepping results obtained at T = 600° and 700°C at P_e = 300 MPa (Figure 8B). Scatter in differential stresses measured for different samples leads to large uncertainties in flow law parameters and the best determinations of n and α come from the strain-rate-stepping experiments, which eliminate sample-to-sample variations. The values of n are much larger than expected for dislocation creep ($3 \leq n \leq 5$) and reflect the nearly perfect plastic response of dolomite at low temperatures.

Strain-rate-stepping results for fine-grained synthetic dolomite, at T = 700°C and P_e = 300 MPa, fitted by power and exponential laws (Figure 9A) yield values of n = ~12 (±10) or α = ~0.023 (±0.03) MPa^{-1}. While these values are considerably smaller than determined for Madoc dolomite at the same conditions, they characterize flow strengths that are similarly insensitive to changes in strain rate.

Flow strengths of coarse- and fine-grained dolomites depend more strongly on strain-rate at high temperatures (T ≥ 800°C) than at low temperatures (Figures 8 & 9) and they exhibit pronounced temperature dependencies (Figures 11 & 12). However, the flow strengths of coarse- and fine-grained dolomites deformed at high temperatures are not generally comparable. Differential stresses measured at (5%) for fine-grained synthetic dolomite show much stronger dependencies on strain-rate and temperature than do stresses measured for the coarse-grained dolomites. Microstructures of the coarse-grained dolomite samples deformed at high temperatures suggest that mechanisms of dislocation recovery and dynamic recrystallization are important at T ≥ 800°C (at $\dot{\varepsilon}$ =

10^{-5} s^{-1}, P_e = 300 MPa). Optical microstructures of deformed synthetic dolomite samples do not provide evidence for dislocation recovery mechanisms nor do they disprove that recovery is important. However, the nearly linear changes in flow strength with strain-rate suggest some form of diffusion creep rather than dislocation creep.

To describe the high temperature deformation of coarse-grained dolomites, I use the same nonlinear functions as used to describe the low temperature deformation, but with an Arrhenius term added to describe reductions in flow strength with increasing temperature:

$$\dot{\varepsilon} = \dot{\varepsilon}_o \left(\frac{\sigma_1 - \sigma_3}{\mu} \right)^n \exp\left(\frac{-H^*}{RT} \right) \tag{6}$$

and

$$\dot{\varepsilon} = \dot{\varepsilon}_o \exp[\alpha(\sigma_1 - \sigma_3)] \exp\left(\frac{-H^*}{RT} \right) \tag{7}$$

where H^* is an activation enthalpy (in kJ/mol), R is the ideal gas constant and absolute T is in Kelvin. In the absence of mechanical data for fine-grained dolomites of varying grain size, eqn. 6 can be used to fit the high temperature results of synthetic dolomite. However, assuming that the nearly linear (Newtonian) stress-strain rate relation for fine-grained dolomite at high temperatures results from Coble (grain boundary diffusion) creep, I fit the high temperature mechanical data of synthetic dolomite by

$$\dot{\varepsilon} = \dot{\varepsilon}_o \left(\frac{\Omega}{d^3} \right) \left(\frac{\sigma_1 - \sigma_3}{\mu} \right)^n \exp\left(\frac{-H^*}{RT} \right) \tag{8}$$

where *d* is the grain size in μm, the grain size exponent is assumed to equal 3, and Ω, the unit cell volume, is used to normalize the diffusional length scale.

Strain-rate-stepping results for coarse-grained Madoc dolomite deformed at T = 800°C (P_e = 300 MPa, Figure 8B) fitted with power and exponential laws yield values of $n = \sim 26$ (±6) or $\alpha = \sim 0.046$ (±0.008) MPa^{-1}. While the *n* value is still large compared to the expected values for dislocation creep ($3 \leq n \leq 5$, Poirier, 1985), *n* determined at T = 800°C is significantly lower than *n* for low temperature experiments. Although microstructures of samples deformed at T ≥ 800°C suggest that recovery and recrystallization are important, the large value of *n* suggests dislocation glide rather than dislocation creep. The value of *α* may thus describe dislocation glide best. However, the stress-strain relation at T > 800°C may differ from that determined at T = 800°C as recovery processes become more important, and the values of *n* decreases correspondingly.

Synthetic dolomite deformed at T = 800°C (P_e = 300 MPa) deforms with a nearly linear (Newtonian) viscous behavior, in contrast to the low temperature (plastic) behavior. From the slope determined in $\log(\sigma_1\text{-}\sigma_3) - \log\dot{\varepsilon}$ at T = 800°C, $n = 1.28 \pm 0.15$ (Figure 9B). The viscous response of fine-grained synthetic dolomite is very different from the nonlinear behavior of Madoc dolomite at 800°C ($n = 26$).

The high temperature data for coarse-grained Madoc dolomite, plotted as $\log(\sigma_1\text{-}\sigma_3)$ versus1/T (Figure 11) yield a slope of:

$$\left(\frac{\Delta\log(\sigma_1-\sigma_3)}{\Delta(1/T)}\right)_{\dot{\varepsilon}} = \frac{H^*}{2.303nR} \tag{9}$$

From the results of individual constant-strain-rate experiments performed at T > 700°C (including the result for Crevola dolomite at T = 900°C; Barber et al., 1994) the ratio H^*/n = 60 ±6 kJ/mol, in contrast to the shallow, negative slope noted at low temperature. Alternatively, if the thermally activated exponential law (eqn. 7) is assumed, the same data fitted in terms of $(\sigma_1-\sigma_3)$ versus1/T yield a slope of:

$$\left(\frac{\Delta(\sigma_1-\sigma_3)}{\Delta(1/T)}\right)_{\dot{\varepsilon}}=\frac{H^*}{\alpha R} \tag{10}$$

with the ratio of H^*/α = 22,907 ±1,078 kJ-MPa/mol. If n or α values from the strain-rate-stepping experiments at T = 800°C are adopted (n = ~26 or α = ~0.046 MPa^{-1}), and I take H^*/n = 60 kJ/mol or H^*/α = 22,907 kJ-MPa/mol, the inferred value of H^* is very large. This result, and the microstructural evidence for dislocation creep suggest that the value of n (and α) is too large. If, on the other hand, n is taken to be ~7, adopting the value reported for dislocation creep of Carrara marble (Schmid et al., 1980), the ratio H^*/n = 60 kJ/mol for Madoc dolomite implies that H^* is ~420kJ/mol. Similarly, the temperature dependence of Madoc dolomite flow strength at high temperatures can be described by the exponential law with α = ~0.018 MPa^{-1} and H^* = ~420kJ/mol.

Temperature-stepping results for Kern Mtns. dolomite yield ratios of H^*/n = 13 ±4 kJ/mol or H^*/α = 6,136 ±1,580 kJ-MPa/mol. However, given the temperature interval over which these data were obtained, it is likely that there values are intermediate between high temperature and low temperature values for crystal plasticity and dislocation creep of dolomite.

The high temperature data for fine-grained synthetic dolomite, plotted as $\log(\sigma_1-\sigma_3)$ versus1/T (Figure 12) yields ratios of H^*/n = 324 ±155 kJ/mol for individual constant strain-rate experiments and H^*/n = 218 ±35 kJ/mol for temperature-stepping experiments. Given the much larger uncertainty in H^*/n from the individual constant-strain-rate experiments, I conclude that the best determination of H^*/n comes from the temperature-stepping experiments. From H^*/n = 218 kJ/mol and n = 1.28, the activation enthalpy H^* = 280 ±45 kJ/mol for high temperature synthetic dolomite (Figure 9B).

Best-fit flow law parameters for the different dolomite starting materials are summarized in Table 9. Values of log $\dot{\varepsilon}_o$ are given for the different flow laws, using a shear modulus, μ, for dolomite of 45.7 GPa (Bass, 1995) and unit cell volume Ω of $3.2\text{x}10^{-10}$ μm^3 (Deer et al., 1992).

Table 9. Flow law parameters

Material	**conditions**	**$\log \dot{\varepsilon}_o$**	**α**	**n**	**H***	**flow law**
Madoc	low T	85.7	----	49±7	----	eqn 2
	low T	-27.1	0.079±0.01	----	----	eqn 3
	high T	29.0	----	7[*]	420±44[*]	eqn 6
	high T	11.8	0.018[**]	----	430 ±8[**]	eqn 7
Kern	high T	13.9	----	7[+]	91±28[+]	eqn 6
	high T	-2.8	0.018[++]	----	108±26[++]	eqn 7
Synthetic	low T	15.8	----	12±10	----	eqn 2
	low T	-10.3	0.023±0.03	----	----	eqn 3
	high T	24.7	----	1.28±0.15	280±45	eqn 8

[*] H^*/n = 60 kJ/mol and H* determined assuming $n = 7$

[**] H^*/α = 25447 kJ/mol and H* determined assuming $\alpha = 0.018$

[+] H* determined assuming $n = 7$

[++] H* determined assuming $\alpha = 0.018$

Dolomite shear stress, μ, 45.7 GPa (Bass, 1995)

Dolomite unit cell, Ω, 3.2×10^{-10} μm^3 (Deer et al., 1992)

DISCUSSION

The results of this study compare favorably with results from previous experimental studies of dolomite deformation (Figure 4). Most of the previous experimental work on dolomite deformation was carried out at low temperatures (25-300°C) and the stress-strain data obtained for Madoc dolomite at 400°C (MD 33) are similar in form to results from these early studies and strengths are of similar magnitude. Madoc dolomite deformed at 400°C, yields at 374 MPa and it's strength at 5% strain is 600 MPa while the results of Turner et al. (1954) for Dover Plains dolomite deformed at 380°C show a yield strength of 360 MPa and a strength at 5% strain of 620 MPa. Handin and Fairbairn (1955) report a strength of 364 MPa at yield and 660 MPa at 5% strain for Hasmark dolomite deformed at 300°C and Barber et al. (1994) report a strength of 395 MPa at yield and 570 MPa at 5% strain for Crevola dolomite deformed at 300°C. Only Barber et al. (1994) report data for dolomite deformed at higher temperatures, and their results for Crevola dolomite deformed at 900°C (σ_1-σ_3 =106 MPa at yield and 308 MPa at 5% strain) are consistent with my results for Madoc dolomite deformed at 850°C (σ_1-σ_3 =267 MPa at yield and 397 MPa at 5% strain). At low temperatures ($T \leq 600$°C) the fine-grained dolomites exhibit stresses higher than the coarse-grained dolomites. The strength of the synthetic dolomite at 400°C is 775 MPa at yield and 875 MPa at 2% strain just prior to faulting (Figure 5), and the strength of Blair dolomite at 500°C is 636 MPa at yield and 765 MPa at 3% strain prior to faulting. At high temperatures ($T \geq 700$°C) the fine-grained synthetic dolomite exhibits weaker behavior than the coarse-grained dolomite at similar conditions.

The unusual increase in strength with increasing temperature displayed by the Madoc dolomite at T ≤ 700°C has not been reported in previous experimental deformation studies of polycrystalline dolomite. However, a similar trend of increasing strength with increasing temperature has been observed for oriented dolomite single crystals (Higgs and Handin, 1959; Barber at al., 1981).

Deformation Mechanisms

Optical microscopy of Madoc dolomite deformed at T ≤ 700°C reveal abundant *f*-twins and thus mechanical twin glide is important at these conditions (Figure 13C). At T ≥ 800°C, microstructures exhibit evidence for dislocation glide, relatively little twin glide, and recovery processes with undulatory extinction and fine recrystallized grains (Figure 13E). These observations are consistent with the relative magnitudes of critical resolved shear stresses (τ_c) for twinning and dislocation slip for oriented single crystals deformed at different temperatures (Figure 15B; Higgs and Handin, 1959; Barber at al., 1981). At T ≤ 700°C, the τ_c for *f*-twinning is less than that for *f*-slip (Barber at al., 1981),while at T > 700°C the τ_c for *f*-slip is less than that for *f*-twinning. The temperature interval over which Madoc dolomite exhibits mechanical twinning corresponds to conditions where dislocation slip on the *f*-plane requires shear stresses that exceed those for twinning on the same plane. In addition to twinning, some dislocation slip must occur, and the increase in Madoc dolomite strength with increasing temperature at T ≤ 700°C corresponds to the increase in critical resolved shear stress of *c*-slip (Barber et al., 1981), though with a shallower negative slope. This comparison

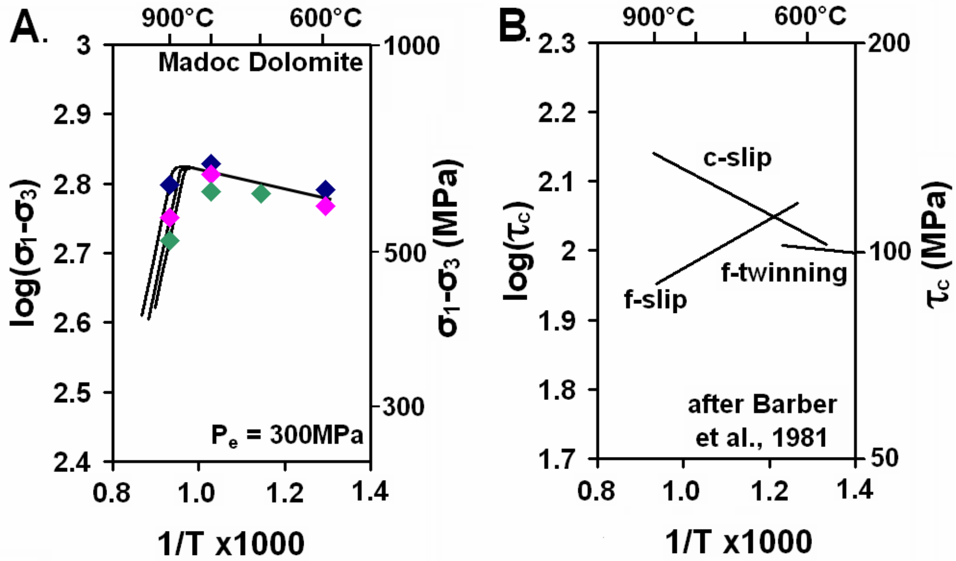

Figure 15. Comparison of temperature effects on strength of Madoc dolomite (A.) with critical resolved shear stresses τ_c of intracrystaline deformation mechanisms (B.) determined for experimentally deformed single crystals (Barber et al., 1981). The temperature interval over which Madoc dolomite exhibits mechanical twinning corresponds to conditions where dislocation slip on the f-plane (f-slip) requires shear stresses that exceed those for twinning on the same plane. The increase in Madoc dolomite strength with increasing temperature at $T \leq 700°C$ corresponds to the increase in critical resolved shear stress of c-slip reported for single crystals (Barber et al., 1981) though with a shallower negative slope. The Arrhenius temperature dependence exhibited by Madoc dolomite at $T \geq 800°C$ is larger than reported for f-slip and may reflect the role of recrystalization and recovery processes that differ between the polycrystalline and single crystal dolomites.

suggests that *c*-slip is one of the important deformation mechanisms in Madoc dolomite at T ≤ 700°C in addition to mechanical twinning.

At higher temperatures (T ≥ 800°C), the temperature dependence of Madoc dolomite strength is larger than that reported by Barber et al. (1981) for *f*-slip. The strong temperature dependence exhibited by Madoc dolomite flow strengths at these conditions may reflect recovery processes and recrystallization in the polycrystalline aggregates that are not as important in the single crystal experiments (Figure 14B).

Many of the deformation and recovery processes of dolomite have been identified by transmission electron microscopy of experimentally deformed single crystals and polycrystalline rocks (Barber et al., 1981, 1994). In polycrystalline Crevola dolomite, Barber et al. (1994) observed evidence for *f*-twinning at all conditions explored (25°C ≤ T ≤ 500°C at $\dot{\varepsilon} = 10^{-4}$ s^{-1}, 700°C ≤ T ≤ 900°C at $\dot{\varepsilon} = 10^{-6}$ s^{-1}), but the highest twin densities were observed in samples deformed at 500° and 700°C. *f*-slip and *c*-slip were also active at all temperatures, with *f*-slip becoming dominant over *c*-slip at T ≥ 700°C. Evidence for dislocation climb was only observed in a single sample deformed at 900°C (Barber et al., 1994). Thus, the high stresses measured at T < 700°C and the nearly plastic behavior of coarse- and fine-grained dolomites correspond to deformation by *f*-twinning and *c*-slip. The reduced strengths determined for coarse-grained Madoc and Kern Mtns. dolomites at high temperatures (T ≥ 800°C) corresponds to reductions in critical resolved shear stress of *f*-slip and processes of dislocation recovery and recrystallization. Mechanical twinning and *c*-slip are of less importance at these higher temperatures.

Transitions in Flow Law

The low temperature mechanical behavior of coarse- and fine-grained dolomites corresponds to temperature- and strain-rate-insensitive crystal plasticity and twinning (Figure 16A). Fine-grained dolomite is stronger than coarse-grained dolomite, as expected if grain boundaries serve as barriers to twin glide and dislocation glide. However, both follow similar exponential flow laws (Table 9; coarse $\dot{\varepsilon}_o = 7.2\text{x}10^{-28}\text{s}^{-1}$ $\alpha = 0.079$ MPa^{-1}, fine $\dot{\varepsilon}_o = 5.0\text{x}10^{-11}\text{s}^{-1}$ $\alpha = 0.023$ MPa^{-1}).

At higher temperatures both coarse- and fine-grained dolomites exhibit transitions to strain-rate- and temperature-dependent strengths (Figure 16A). However, the transitions occur at different temperatures and the slopes are distinct (Figure 16A). Mechanical and microstructural evidence indicates that coarse-grained Madoc dolomite deforms by dislocation creep at high temperature while fine-grained synthetic dolomite deforms by diffusion creep. Over a wide range of high temperatures, fine-grained synthetic dolomite is weaker than the coarse-grained Madoc dolomite.

The transition from crystal plasticity and twinning to dislocation creep in coarse-grained Madoc dolomite occurs between T = 700°C and 800°C at $\dot{\varepsilon} = 10^{-5}\text{s}^{-1}$. This transition is expected to shift to lower temperatures at lower (i.e. geologic) strain rates but it should not be strongly affected by grain size. Given that the compound parameter H^{*}/n (or H^{*}/α) at high temperatures is well determined for Madoc dolomite, the transition temperature at laboratory strain rates is known. However, dependable prediction of the transition temperature at lower, geologic strain rates must await better determinations of the individual parameters, H^{*} and n (or potentially α).

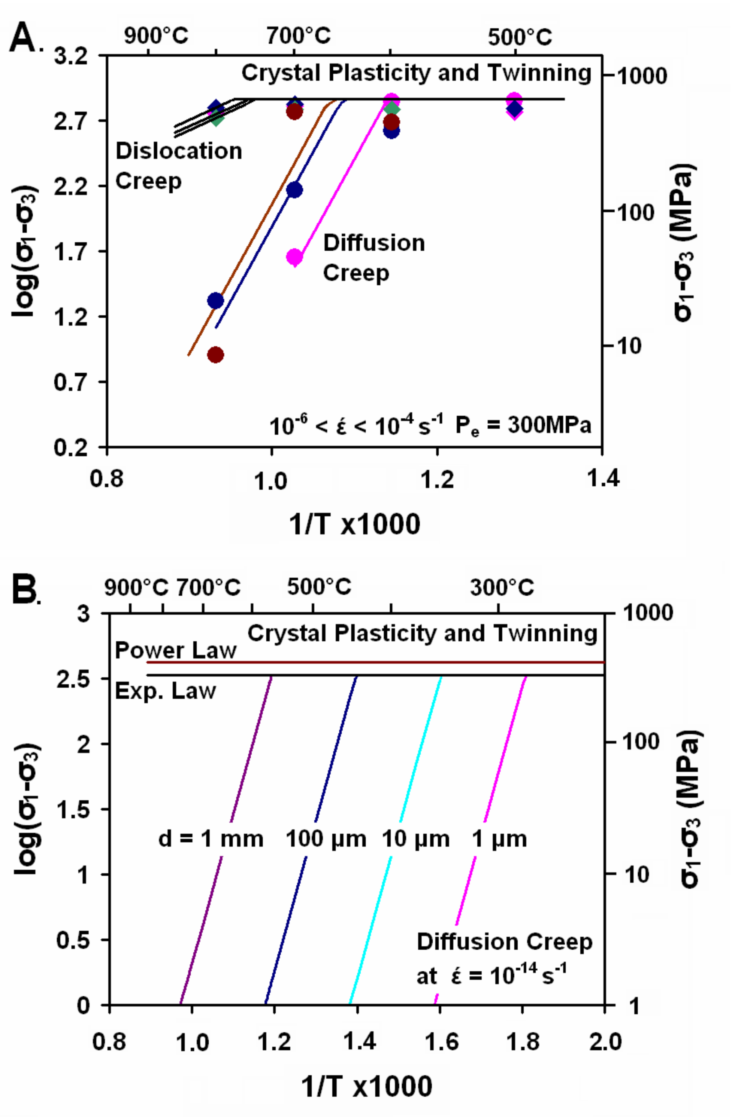

Figure 16. Transitions from crystal plasticity and mechanical twinning at low temperature and high stress to dislocation creep and diffusion creep at higher temperatures and reduced stresses. A. Comparison of strengths measured for coarse-grained Madoc dolomite (diamonds) and for fine-grained synthetic dolomite (circles). Both starting materials show high, temperature-insensitive, strength at low temperatures. However the transitions to temperature-dependent creep differ; critical temperatures for the transitions differ and the slopes in $\log(\sigma_1-\sigma_3)$ - 1/T differ, corresponding to deformation by dislocation creep ($n = \sim 7$, $\alpha = \sim 0.018$ MPa^{-1}, $H^* = 420$ kJ/mol; Madoc dolomite) and deformation by diffusion creep ($n = 1.28$, $H^* = 280$ kJ/mol; synthetic). B. Extrapolating the diffusion creep relation determined for fine-grained synthetic dolomite to a geologic strain rate of $\dot{\varepsilon} = 10^{-14}\mathrm{s}^{-1}$, the transition from crystalline plasticity and twinning to diffusion creep shifts to lower temperature. Assuming a grain size dependence according to Coble creep, dolomite strengths are inferred at $\dot{\varepsilon} = 10^{-14}\mathrm{s}^{-1}$ and grain sizes of 1 μm to 1 mm.

The transition from crystal plasticity and twinning to diffusion creep in the fine-grained synthetic dolomite (with a grain size of d = 2.5 μm) occurs at temperatures between 600° and 700°C at laboratory strain-rates. Assuming that the high temperature deformation is described by grain boundary (Coble) diffusion creep (eqn. 8), the transition from crystal plasticity to diffusion creep should occur at lower temperatures at lower (geologic) strain-rates. Extrapolating eqn. 8 with the creep law parameters determined for synthetic dolomite (Table 9; $\dot{\varepsilon}_o = 4.7\text{x}10^{24}\text{s}^{-1}$, $n = 1.28$, $H^* = 280$ kJ/mol) to a geological strain-rate of $10^{-14}\ \text{s}^{-1}$, the transition from crystal plasticity and twinning to diffusion creep can be predicted for varying grain sizes (Figure 16B). For example, the transition from crystal plasticity to diffusion creep is predicted to occur at T = 280°C for fine-grained dolomites (d = 1 μm) while the transition is predicted at T = 450°C for d = 100 μm, and at T = 580°C for d = 1 mm. Thus dolomite may be strong (deforming by crystal plasticity and twinning) or weak (deforming by diffusion creep), depending critically on temperature and grain size.

Comparison of Dolomite and Calcite Strengths

Coarse-grained Madoc and Kern Mtns. dolomite are strong over the range of conditions tested, with flow strengths that exceed those reported for calcite rocks by an order of magnitude (at T = 600° to 800°C; Figure 17; Heard and Raleigh, 1972; Schmid et al., 1980; Walker et al., 1990; Renner et al., 2002). At low temperatures (T ≤ 700°C), deformation of dolomite by twinning and dislocation glide is insensitive to temperature and strain rate, while deformation of coarse-grained calcite rocks occurs by dislocation creep at the same conditions with significant temperature and strain rate sensitivities.

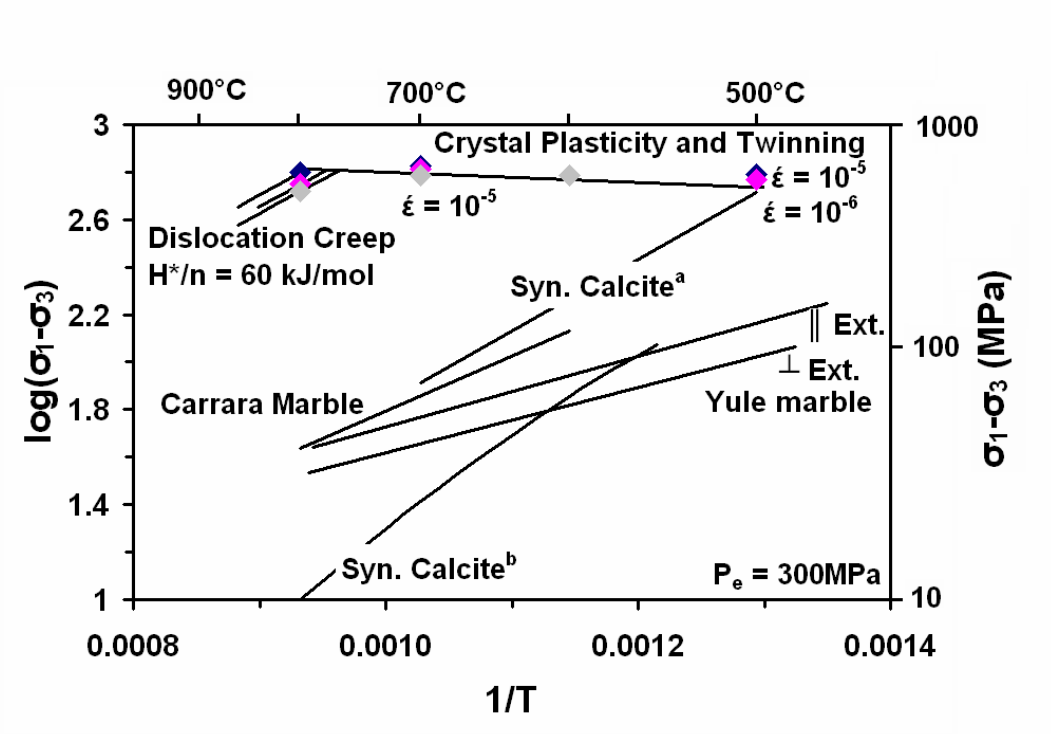

Figure 17. Comparison of Madoc dolomite strength with calcite marble data for dislocation creep at $\dot{\varepsilon} = 10^{-5}s^{-1}$ (Yule marble results of Heard and Raleigh, 1972; Carrara marble, Schmid et al., 1980; synthetic calcite[a], Walker et al., 1990; synthetic calcite[b], Renner et al., 2002)

At higher temperatures (T ≥ 800°C), coarse-grained dolomite deforms by dislocation creep with a compound parameter H^*/n = 60 kJ/mol that is larger than H^*/n ratios for Yule marble (H^*/n = 28 kJ/mol; Heard and Raleigh, 1972), and Carrara marble (H^*/n = 44 kJ/mol; Schmid et al., 1980) but similar to H^*/n for coarse synthetic marbles (H^*/n = 57 kJ/mol Walker et al., 1990; and effective temperature dependence of synthetic marble or Renner et al., 2002).

The high strength of dolomite compared with calcite has been attributed to differences in its structure and Ca, Mg ordering that offer greater lattice resistance to twin glide and dislocation slip (Barber, 1977; Barber et al., 1981, 1983; Wenk et al., 1983; Barber and Wenk, 2001). The results of this study confirm the high resistance to intracrystalline deformation mechanisms.

Coarse-grained dolomites deformed in the laboratory are stronger than calcite rocks at all experimental conditions tested, and flow laws extended to geologic conditions indicate that coarse-grained dolomite will be strong relative to calcite-rich units, as observed by Carter (1992) and Bestmann et al. (2000). However, strengths of fine-grained dolomite and calcite aggregates deformed by diffusion creep show much less contrast in rheology (Figure 18). Diffusion creep strengths of dolomite are comparable (at T = 800°C, $\dot{\varepsilon} = 10^{-5}\ \mathrm{s}^{-1}$) to those measured for Solenhofen limestone (Schmid et al., 1977), and a factor of 10 higher than calculated for synthetic calcite aggregates of a comparable grain size (Walker et al. 1990). Given that grain growth is more rapid for calcite (Olgaard and Evans, 1988; Olgaard and Fitz Gerald, 1993; Zhu et al., 1999) than for dolomite and high Mg calcite (Kronenberg et al., 2003; Herwegh et

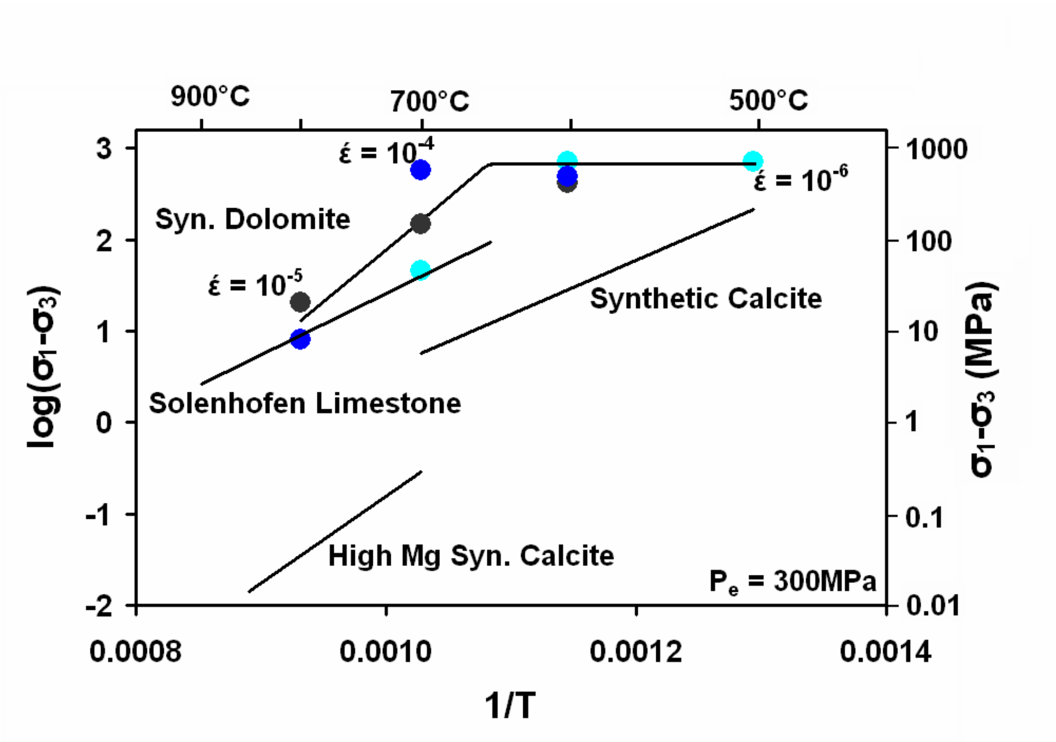

Figure 18. Comparison of synthetic dolomite strength with fine-grained limestone and synthetic calcites deformed by diffusion creep (results shown for $\dot{\varepsilon}$ = $10^{-5}s^{-1}$; Solenhofen limestone, Schmid et al., 1977; synthetic calcite marble with calculated grain size d = 2.5μm, Walker et al., 1990; high Mg synthetic calcite marble with calculated grain size d = 2.5μm, Herwegh et al., 2003).

al., 2003), dolomites may have finer grain sizes than limestones and marbles subjected to comparable thermal history reducing further the strength contrast between these carbonates.

For diffusion creep in dolomite, the best-fit value of $n = 1.28$ is similar to values reported for diffusion creep in calcite ($n = 1.66$ Schmid et al., 1977; $n = 1.67$ Walker et al., 1990; $n = 1.1$ Herwegh et al., 2003). The value of H^* determined for diffusion creep in the synthetic dolomite aggregates is 280 kJ/mol, somewhat higher than values reported for diffusion creep in calcite ($H^* = 213$, Schmid et al., 1977; $H^* = 190$, Walker et al., 1990; $H^* = 200$, Herwegh et al., 2003)

While large differences in crystal plastic strengths and dislocation creep strengths of dolomite and calcite can be explained by differences in crystal structure, the obstacles to internal strain in dolomite are of no consequence to diffusion at grain boundaries or to grain boundary sliding. Diffusion creep of polycrystalline dolomite requires the net transport along grain boundaries of the same cations and anions as must diffuse along grain boundaries of calcite during diffusion creep, with the addition of Mg. Thus, rates of diffusion creep for these carbonates may be comparable at laboratory and geologic conditions. Herwegh et al. (2003) report similar rheologies for diffusion creep of magnesian calcite aggregates, of varying Mg-contents, with creep rates that depend on grain size but not directly on Mg content.

Application to Geologic Deformation Rates

The experimental results for the coarse-grained dolomites constrain the flow law parameters for crystal plastic deformation at low temperatures and dislocation creep at high temperatures. The experimental results for fine-grained dolomites provide further evidence of crystal plasticity at low temperatures, while flow law parameters at high temperature correspond to diffusion creep. Taken together, the flow laws for coarse- and fine-grained dolomites constrain the fields over which different deformation mechanisms are predominant (Figure 19). The rheologies listed in Table 9 can be used to construct a deformation mechanism map for dolomite of a given grain size (d = 100μm) in log $[(\sigma_1-\sigma_3)/\mu]$ versus T/T_m space (Figure 19), normalizing differential stress by a shear modulus $\mu = 45.7$ GPa (Bass, 1995), and normalizing temperature by a melting temperature, $T_m =$ 1373 K (inferred as the metastable extension of higher pressure melting determinations to P = 300MPa, Wyllie and Huang, 1976).

Three fields are displayed on the deformation mechanism map for dolomite (Figure 19): crystal plasticity at high stresses, dislocation creep at high temperatures and relatively high stresses, and diffusion creep at elevated temperatures. Strain-rate contours are shown from the laboratory values $\dot{\varepsilon} = 10^{-5}\ s^{-1}$ to geologic values $\dot{\varepsilon} = 10^{-14}\ s^{-1}$. The transition between crystal plasticity and dislocation creep is documented by experiments on Madoc dolomite (data shown and strain-rate contours for dislocation creep are shown for assumed $n = 7$ and $H^* = 420$ kJ/mol). The transition between crystal plasticity and diffusion creep is documented by experiments on synthetic dolomite (for d = 2.5 μm) and calculated for d = 100 μm based on flow laws for crystal plasticity and diffusion creep (Table 9).

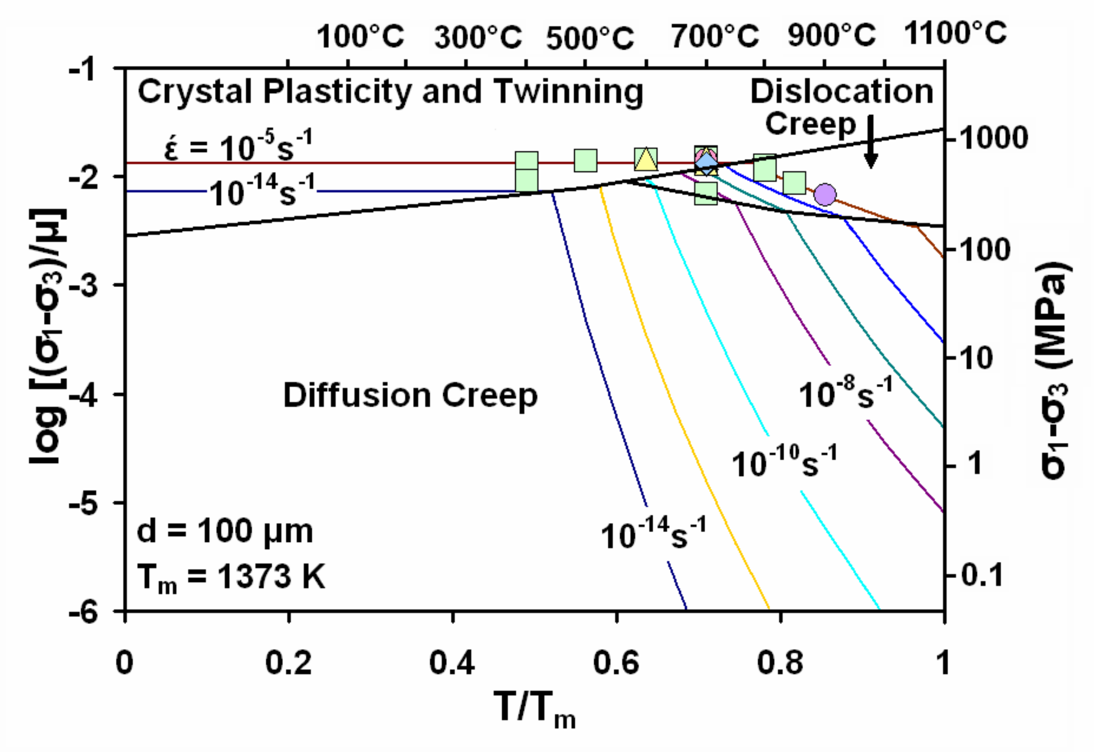

Figure 19. Deformation mechanism map for dolomite. With a grain size of 100µm, normalizing temperature by a melting temperature, T_m, of 1100°C (metastable extension from high pressure measurements; Wyllie and Huang, 1976) and normalizing differential stress by a shear modulus of 45.7GPa (Bass, 1995). Dislocation glide and twinning is restricted to high stresses and (Coble) diffusion creep extrapolated to geologic strain rates is inferred to be predominate over a wide range of differential stress, temperature, and grain size. The field of dislocation creep inferred from the measurement of $H^*/n = 60$ and a value of $n \sim 7$ (assuming a value similar to that reported for Carrara marble; Schmid et al., 1980) is restricted to conditions of high stress and temperature for coarse dolomite marbles. Data shown for Madoc dolomite (squares are 10^{-5}, yellow triangle is 10^{-6}, blue diamond 10^{-7}, red circle is 10^{-4}) and the high temperature Crevola dolomite (Purple circle 10^{-4}).

Deformation by crystal plasticity occurs only at very high stresses, irrespective of strain-rate, so it is unlikely to be common under geologic conditions. The extent of the dislocation creep field is dependent on grain size, but at d = 100 µm, this field is limited to high temperature (T > 600°C) and relatively high stress. Therefore, dislocation creep in dolomite is expected to be restricted to high temperature and high tectonic stress environments. Over most geologic strain-rates, 10^{-10} s^{-1} to $\dot{\varepsilon} = 10^{-14}$ s^{-1}, and low tectonic stresses, the predominant deformation mechanism for dolomite is predicted to be diffusion creep.

Comparisons with Naturally Deformed Dolomites

Studies of naturally deformed dolomites emphasize the roles of brittle fracture at low temperatures (Woodward et al., 1988; Erickson, 1994; Bestmann et al., 2000) and crystal plasticity and dislocation creep at higher temperatures (White and White, 1980; Leiss and Barber, 1999; Newman and Mitra, 1994). Diffusion creep has been reported only once, for the fine grain size fraction of dolomites that were previously recrystallized (White and White, 1980). The results of this study have implications for the conditions required to activate mechanical twinning and dislocation creep, and they suggest that diffusion creep has been under-reported as an important deformation mechanism.

The inferred high strength of dolomite in many tectonic settings is consistent with the high stresses required for crystal plasticity and dislocation creep. Similarly, examples of dolomites that deform by fracture without any evidence of intracrystalline slip (Woodward et al., 1988; Erickson, 1994; Bestmann et al., 2000) are consistent with the results of this study and imply deformation at low effective pressures.

In dolomites surrounding fault rocks deformed at conditions of lower greenschist facies (T < 300°C), Newman and Mitra (1994) reported twins and undulatory extinction associated with crystal plasticity. Microstructures of dolomites within the fault zone include subgrains, serrated grain boundaries and fine recrystallized grains associated with dislocation creep. Based on the results of this study, the activation of dislocation glide and mechanical twinning required large differential stresses. The evidence for dislocation recovery and recrystallization at low shear stress conditions, is difficult to reconcile with the limited range of conditions this study determined for dislocation creep. However, the apparent strain localization of the fault zone may be explained by the development of fine (~10 μm) recrystallized grains that deformed by diffusion creep.

In carbonates of the Damara Orogen (of Namibia) deformed at upper greenschist facies conditions (~400 - 500°C), Leiss and Barber (1999) reported dislocation creep microstructures and lattice preferred orientations for dolomite porphyroclasts within a finely recrystallized matrix. The coarse dolomite grains (~500 μm in diameter) exhibit undulatory extinction, *f*-twins and serrated grain boundaries. Recrystallized grains, 30-80 μm in size, exhibit lattice preferred orientations that are consistent with *c*-slip, while the finest recrystallized grains, 5-10 μm in size, exhibit only weak crystallographic alignments. Again, the microstructures related to mechanical twinning and dislocation creep suggest that these rocks were deformed at high differential stresses. Based on the results of this study, the finest recrystallized grains (d = 5-10 μm) of the Damara Orogen dolomites may have deformed by diffusion creep (Figure 16B) while the coarsely recrystallized grains (d = 30-80 µm) may have been deformed by transitional dislocation/diffusion creep.

In metaconglomerates deformed in the amphibolite facies (T ~ 600°C), White and White (1980) reported creep microstructures in dolomite pebbles, including undulatory extinction, grain flattening, recrystallization, and dislocation of the *c*-slip, *f*-slip, and *r*-slip systems. Unlike the studies of dolomites deformed at lower temperatures, mechanical twins are not reported for these dolomites. Moreover, dislocations were observed in the coarse dolomite grains (40-100 µm) but not in the finest recrystallized grains (~10 µm). The highest temperatures of deformation for these rocks are consistent with the dislocation creep field of dolomite (Figure 19) and stresses were likely lower than for the other field examples for which mechanical twinning played a role in their crystal plastic response. White and White (1980) proposed that the coarser dolomite grains of these metaconglomerates deformed by dislocation creep while the fine, dislocation free dolomite grains deformed by diffusion creep and grain boundary sliding. These interpretations are consistent with the deformation mechanism map for dolomite, and we infer that once significant populations of fine grains were generated, deformation could continue at reduced differential stresses.

CONCLUSIONS

Deformation experiments performed on natural and hot isostatically pressed dolomite aggregates (grain sizes d = 2.5, 10, 80, 230 μm) at effective pressures $P_e = 50 - 400$ MPa, temperatures T = 400 – 850°C, and strain rates $\dot{\varepsilon} = 1.2\text{x}10^{-4}\ \text{s}^{-1}$ to $1.2\text{x}10^{-7}\ \text{s}^{-1}$ define three fields of deformation: 1) crystal plasticity, 2) dislocation creep, and 3) diffusion creep. Coarse- and fine-grained dolomite deformed at low temperature (T ≤ 700°C for coarse-grained, T < 700°C for fine-grained) exhibit mechanical behavior that is nearly plastic and microstructures show that mechanical *f*-twinning and dislocation glide are important. For coarse-grained dolomite, this behavior can be described either by a power law relationship with $n = 49$ (±7), or by an exponential law with $\alpha = 0.079$ (±0.01) MPa^{-1}. The mechanical behavior of fine-grained dolomite can be described similarly by $n = 12$ (±10), or $\alpha = 0.023$ (±0.03)MPa^{-1}. At low temperatures, coarse-grained dolomite is somewhat stronger with increase of temperatures and fine grained dolomite exhibits strengths that are nearly independent of temperature.

At high temperatures (T ≥ 800°C), flow strengths of coarse- and fine-grained dolomite depend more strongly on strain-rate and exhibit pronounced temperature dependencies. Coarse-grained dolomite samples deform by dislocation glide, accommodated by recovery and recrystallization while fine-grained dolomite samples appear to deform by diffusion creep. The high temperature creep of coarse-grained dolomite is characterized by a highly nonlinear strain rate-stress relation ($n \leq 26$ or $\alpha \leq 0.046\ \text{MPa}^{-1}$) while creep of fine-grained dolomite is nearly linearly viscous ($n = 1.28$ ±0.15).

The temperature dependence of coarse-grained dolomite strength is given by H^*/n = 60 kJ/mol, or H^*/α = 25447 kJ/mol but independent determinations of H^* and n are still needed to fully characterize the rheology associated with dislocation creep. The activation enthalpy for diffusion creep of fine-grained dolomite is $H^* = 280 \pm 45$ kJ/mol.

This study confirms that coarse-grained dolomite deformed by intracrystalline mechanisms of dislocation glide and twinning is much stronger than calcite-rich limestone or marble deformed at comparable conditions. However, when mechanical properties are not governed by lattice resistance to intracrystalline deformation mechanisms, as for diffusion creep involving grain boundary diffusion and sliding, strengths of fine-grained dolomite and calcite are more similar. Fine-grained dolomite and calcite deformed by diffusion creep show little contrast in rheology.

Flow laws for coarse- and fine-grained samples constrain the deformation mechanism map for dolomite. Crystal plasticity and twinning require high differential stresses, irrespective of strain rate. The extent of the dislocation creep field depends on grain size, but at d = 100 μm, this field is limited to high temperatures and relatively high stresses. Diffusion creep is predicted to be the most common mechanism of deformation for all but the coarsest polycrystalline dolomite over geologic strain rates of $\dot{\varepsilon} = 1.2\text{x}10^{-10}\ \text{s}^{-1}$ to $1.2\text{x}10^{-14}\ \text{s}^{-1}$.

REFERENCES

Barber, D.J., 1977. Defect microstructures in deformed and recovered dolomites. Tectonophysics 39, 193-213.

Barber, D.J. and Wenk, H.R., 1979. Deformation twinning in calcite, dolomite, and other rhombohedral carbonates. Physics and Chemistry of Minerals 5, 141-165.

Barber, D.J., Heard, H.C. and Wenk, H.R., 1981. Deformation of dolomite single crystals from 20°-800°C. Physics and Chemistry of Minerals 7, 271-286.

Barber, D.J., Freeman, L.A. and Smith, D.J., 1983. Analysis of high-voltage, high-resolution images of lattice-defects in experimentally-deformed dolomite. Physics and Chemistry of Minerals 9, 102-108..

Barber, D.J., Wenk, H.R. and Heard, H.C., 1994. The plastic deformation of polycrystalline dolomite: Comparison of experimental results of theoretical predictions. Materials Science and Engineering A – Structural Materials Properties Microstructure and Processing 175, 83-104.

Barber, D.J. and Wenk, H.R., 2001. Slip and dislocation behavior in dolomite. European Journal of Mineralogy 13, 221-243.

Bass, J.D., 1995. Elasticity of minerals, glasses and melts. In: Mineral Physics and Crystallography, A Handbook of Physical Constants, AGU Reference Shelf 2, T.J. Ahrens (Ed.), American Geophysical Union, Washington, DC., 45-63

Bestmann, M., Kunze, K., Matthews, A., 2000. Evolution of a calcite marble shear zone complex on Thassos Island, Greece: microstructural and textural fabrics and their kinematic significance. J. Struct. Geol. 22, 1789-1807.

Burkhard, M., 1990. Ductile deformation mechanisms in micritic limestones naturally deformed at low temperatures (150-350°C). In: Knipe, R.J. and Rutter, E.H. (Eds.), Deformation Mechanisms, Rheology and Tectonics. Geological Society Special Publication No. 54, 241-257.

Busch, J.P. and van der Pluijm, B.A., 1995. Calcite textures, microstructures and rheological properties of marble mylonites in the Bancroft shear zone, Ontario, Canada. J. Struct. Geol. 17, 677-688

Carter, K.E., 1992. Evolution of stacked, ductile shear zones in carbonates from mid-crustal levels: Tuscan Nappe, N. Apennines, Italy. J. Struct. Geol. 14, 181-192.

Casey, M., Kunze, K., and Olgaard, D.L., 1998. Texture of Solenhofen limestone deformed to high shear strains in torsion. J. Struct. Geol. 20, 255-267.

Covey-Crump, S.J., 1997.The high temperature static recovery and recrystallization behavior of cold-worked Carrara marble. J. Struct. Geol. 19, 255-241.

Covey-Crump, S.J., 1998. Evaluation of mechanical state in Carrara marble during deformation at 400° to 700°C. J. Geophys. Res. 103, B12, 29781-29794.

de Bresser, J.H. and Spiers, C.J., 1993. Slip systems in calcite single-crystals deformed at 300° to 800°C. J. Geophys. Res. 98, 6397-6409.

de Bresser, J.H.P., 1996. Steady state dislocation densities in experimentally deformed calcite materials: Single crystal verses polycrystals. J. Geophys. Res. 101, B10, 22189-22201.

de Bresser, J.H.P. and Spiers, C.J., 1997. Strength Characteristics of the r, f, and c slip systems in calcite. Tectonophysics 272, 1-23.

Deer, W.A., Howie, R.A., Zussman, J., 1992. An Introduction to the Rock-Forming Minerals; second edition. Addison Wesley Longman Limited, Essex, England, 696p.

Dressen, G. and Evans, B., 1993. Brittle and semibrittle deformation of synthetic marbles composed of two phases. J. Geophys. Res. 98, B7, 11921-11933.

Erickson, S.G., 1994. Deformation of shale and dolomite in the Lewis Thrust-fault zone, Northwest Montana, USA. Canadian Journal of Earth Sciences, 31, 1440-1448.

Fredrich, J.T., Evans, B., and Wong, T., 1989. Micromechanics of the brittle to plastic transition in Carrara marble. J. Geophys. Res. 94, B4, 4129-4145.

Goldsmith, J.R., 1959. Some aspects of the geochemistry of carbonates. In: Abelson, P.H. (Ed.), Researches in Geochemistry, Vol. 1, 336-358.

Griggs, D. and Miller, W.B., 1951. Deformation of Yule marble, Part I. Compression and extension on dry Yule marble at 10000atmospheres confining pressure, room temperature. GSA Bulletin 62, 853-862.

Griggs, D.T., Turner, F.J., Borg, I. and Sosoka, J., 1951. Deformation of Yule marble, Part IV. Effects at 150°C. GSA Bulletin 62, 1385-1486.

Griggs, D.T., Turner, F.J., Borg, I. and Sosoka, J., 1953. Deformation of Yule marble, Part V. Effects at 300°C. GSA Bulletin,64, 1327-1342.

Griggs, D.T., Turner, F.J., Heard, H.C., 1960. Deformation of rocks at 500°c to 800°C. In: Griggs, D.T. and Handin, J., (Eds.), Rock deformation, Memoirs of the Geological Society of America 79, 39-104.

Handin, J. and Griggs, D. 1951. Deformation of Yule marble, Part II. Predicted fabric changes. GSA Bulletin 62, 863-886.

Handin, J. and Fairbairn, H.W., 1955. Experimental deformation of Hasmark dolomite. GSA Bulletin 66, 1257-1274.

Handin, J., Heard, H.C., and Magourick, J.N., 1967. Effects of intermediate principle stress on the failure of limestone, dolomite, and glass at different temperatures and strain rate. J. Geophys. Res. 72, 611-640.

Heard, H.C., 1960. Transition from brittle fracture to ductile flow in Solenhofen limestone as a function of temperature, confining pressure, and interstitial fluid pressure. In: Griggs, D.T. and Handin, J. (Eds.), Rock deformation, Memoirs of the Geological Society of America 79, 193-226.

Heard, H.C., 1963. Effect of large changes in strain rate in the experimental deformation of Yule marble. Journal of Geology 71, 162-195.

Heard, H.C. and Raleigh, C.B., 1972. Steady-state flow in marble at 500°to 800°C. GSA Bulletin 83, 935-956.

Heitzmann, P., 1987. Calcite mylonites in the central Alpine “root zone”. Tectonophysics 135, 207-215.

Herwegh, M., Xio, X. Evans, B., 2003. The effect of dissolved magnesium on diffusion creep in calcite. Earth Planet. Sci. Lett. 212, 457-470.

Higgs, D.V. and Handin, J., 1959. Experimental deformation of dolomite single crystals. GSA Bulletin 70, 245-278.

Kronenberg, A.K., Davis, N.E., Wheelock, P., Newman, J., 2003. Grain growth kinetics of dolomite and magnesite. American Geophysical Union Fall Meeting abstract, San Francisco.

Leiss, B., Siegesmund, S., Webber, K., Olesen, N.Ø., 1994. Localized texture components of a naturally deformed dolomite – a contribution to the analysis of texture-forming processes. In: Bunge, H.J., Siegesmund, S., Skrotzki, W., Weber, K., (Eds.), Textures of Geological Materials. DGM Press, Oberusel, pp. 261-275.

Leiss, B., Siegesmund, S., Webber, K., 1996. The development of different texture-types in ductile deformed dolomite rocks. International Geology Congress Beijing. p. 265.

Leiss, B. and Barber, D.J., 1999. Mechanisms of dynamic recrystallization in naturally deformed dolomite inferred from EBSP analyses. Tectonophysics 303, 51-69.

Molli, G. Conti, P., Giorgetti, G., Meccheri, M., Oesterling, N., 2000. Microfabric study on the deformational and thermal history of the Alpi Apuane marbles (Carrara marbles), Italy. J. Struct. Geol. 22, 1809-1825.

Newman, J. and Mitra, G., 1994. Fluid-influenced deformation and recrystallization of dolomite at low temperatures along a natural fault zone, Mountain City window, Tennessee. GSA Bulletin 106, 1267-1280.

Olgaard, D.L. and Evans, B., 1988. Grain growth in synthetic marbles with added mica and water. Contributions to Minerology and Petrology 100, 246-260.

Olgaard, D.L. and Fitz Gerald, J.D., 1993. Evolution of pore microstructures during healing of grain boundaries in synthetic calcite rocks. Contributions to Minerology and Petrology 115, 138-154.

Paterson, M.S. and Olgaard, D.L., 2000. Rock deformation tests to large shear strains in torsion. J. Struct. Geol. 22, 1341-1358.

Paterson, M.S. and Turner, F.J., 1970. Experimental deformation of constrained crystals of calcite in extension. In: Paulitsch, P. (Ed.), Experimental and Natural Rock Deformation. Springer-Verlag, Berlin.

Poirier, J.P., 1985. Creep of Crystals: High-Temperature Deformation Processes in Metals, Ceramics, and Minerals, Cambridge University Press, Cambridge, 260p.

Renner, J., Evans, B., Siddiqi, G., 2002. Dislocation creep of calcite. J. Geophys. Res. 107, B12, 2364 ECV 6 1-16

Rowe, K.J. and Rutter, E.H. 1990. Paleostress estimation using calcite twinning: Experimental calibration and application to nature. J. Struct. Geol. 12, 43-61.

Rutter, E.H., 1995. Experimental study of the influence of stress, temperature, and strain rate on the dynamic recrystallization of Carrara marble. J. Geophys. Res. 100, B12, 24651-24663.

Schmid, S., 1976. Rheological evidence for changes in the deformation mechanism of Solenhofen limestone towards low stresses. Tectonophysics 31, T21-T28.

Schmid, S., Boland, J.N. and Paterson, M.S., 1977. Super-plastic flow in fine-grained limestone. Tectonophysics, 43, 257-292.

Schmid, S., Paterson, M.S. and Boland, J.N., 1980. High temperature flow and dynamic recrystallization in Carrara marble. Tectonophysics 65, 245-280.

Schmid, S.M., Panozzo, R., and Bauer, S., 1987. Simple shear experiments on calcite rocks: rheology and microfabric. J. Struct. Geol. 9, 747-778.

Spiers, C.G. and Wenk, H.R., 1980. Evidence for slip on r and f in the positive sense in deformed calcite single crystals. EOS Trans. Am. Geophys. Union 61, 1128.

Turner, F.J. and Ch'ih, C.S., 1951. Deformation of Yule marble, Part III: Observed fabric changes due to deformation at 10,000 atmospheres confining pressure, room temperature, dry. GSA Bulletin 62, 887-906.

Turner, F. J., Griggs, D.T., Heard, H., Weiss, L.W., 1954. Plastic deformation of dolomite rock at 380°C. American Journal of Science 252, 477-488.

Turner, F.J., Griggs, D.T., Clark, R.H. and Dixon, R.H., 1956. Deformation of Yule marble, Part VII: Development of oriented fabrics at 300°C-500°C. GSA Bulletin 67, 1259-1294.

Turner, R.J. and Orozco, M., 1976. Crystal bending in metamorphic calcite and its relation to associated twinning. Contrib. Mineral. Petrol. 57, 83-97.

Ulrich, S., Schulmann, K., Casey, M., 2002. Microstructural evolution and rheological behaviour of marbles deformed at different crustal levels. J. Struct. Geol. 24, 979-995.

Walker, A.N., Rutter, E.H., Brodie, K.H., 1990. Experimental study of grain-size sensitive flow of synthetic, hot-pressed calcite rocks. In: Knipe, R.J. and Rutter, E.H. (Eds.), Deformation Mechanisms, Rheology and Tectonics. Geological Society Special Publication No. 54, 259-284.

Wang, Z.C., Bai, Q., Dresen, G. and Wirth, R., 1996. High-temperature deformation of calcite single crystals. J. Geophys. Res. 101, 20377-20390

Weiss, L.E. and Turner, F.J., 1972. Some observations on translation gliding and kinking in experimentally deformed calcite and dolomite. In: Heard, H.C., et al. (Eds.), Flow and Fracture of Rocks. Geophys. Monogr. Ser. 16, Am. Geophys. Union, Washington D.C.

Wenk, H.R. and Shore, J., 1975. Preferred orientation in experimentally deformed dolomite. Contributions to Mineralogy and Petrology 50, 115-126.

Wenk, H.R., Barber, D.J., Reeder, R.J., 1983. Microstructures in carbonates. In: Reeder, R.J. (Ed.), Carbonates: Mineralogy and Chemistry. Reviews in Mineralogy, 11, Mineralogical Society of America, Bookcrafters Inc., Chelsea, Michigan, 301-367.

White, J.C. and White, S.H., 1980. High-voltage transmission electron microscopy of naturally deformed polycrystalline dolomite. Tectonophysics 66, 35-54.

Woodward, N.B., Wojtal, S., Paul, J.B., Zadins, Z.Z., 1988. Partitioning of deformation within several external thrust zones of the Appalachian orogen. Journal of Geology 96, 351-361.

Wyllie, P.J., Huang, W.L., 1976. Carbonation and melting reactions in the system CaO – MgO – SiO_2 – CO_2 at mantle pressures with geophysical and petrological applications. Contributions to Mineralogy and Petrology 54, 79-107.

Zhu, W.L., Evans, B. and Bernabe, Y., 1999. Densification and permeability reduction in hot-pressed calcite: A kinetic model. J. Geophys. Res. 104, 25501-25511.

APPENDIX

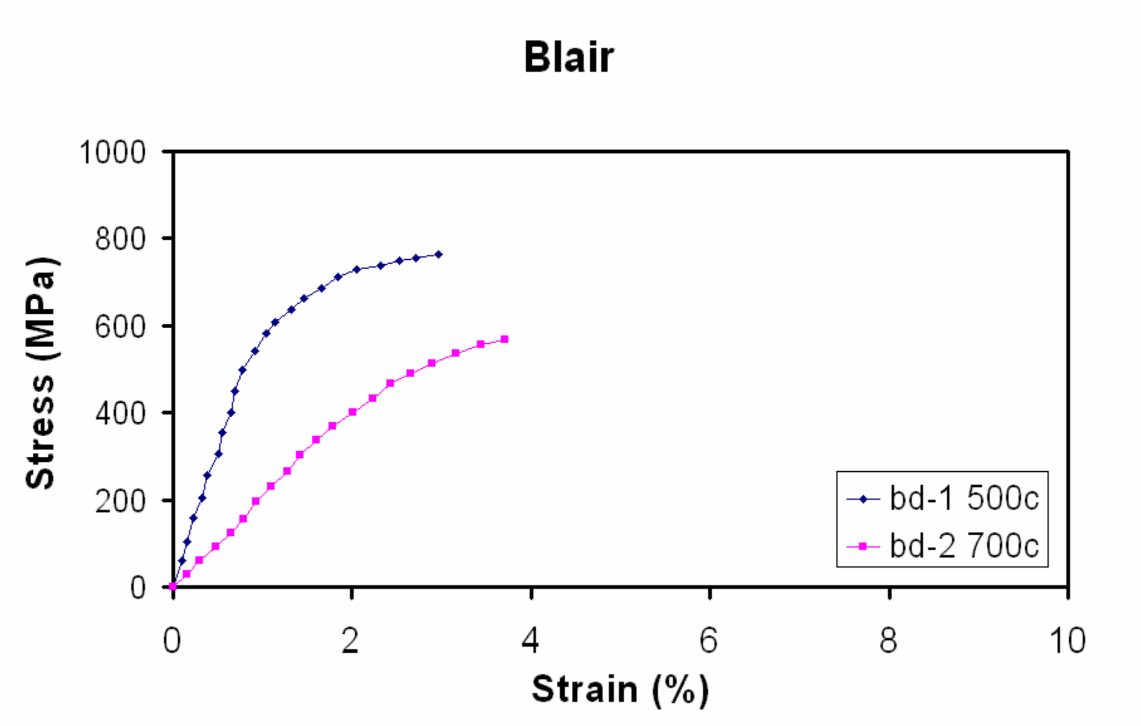
Blair
1000
800
600
400
200
0
Stress (MPa)
0
2
4
6
8
10
Strain (%)
bd-1 500c
bd-2 700c

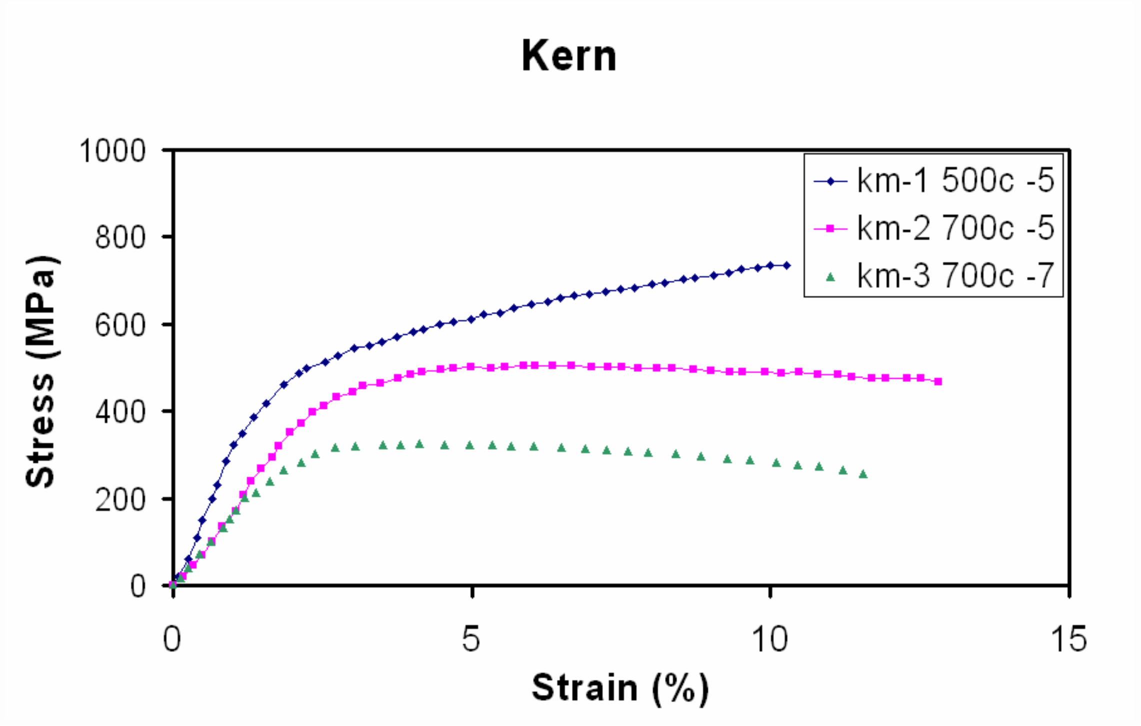
Kern
1000
800
600
400
200
0
Stress (MPa)
0
5
10
15
Strain (%)
km-1 500c -5
km-2 700c -5
km-3 700c -7

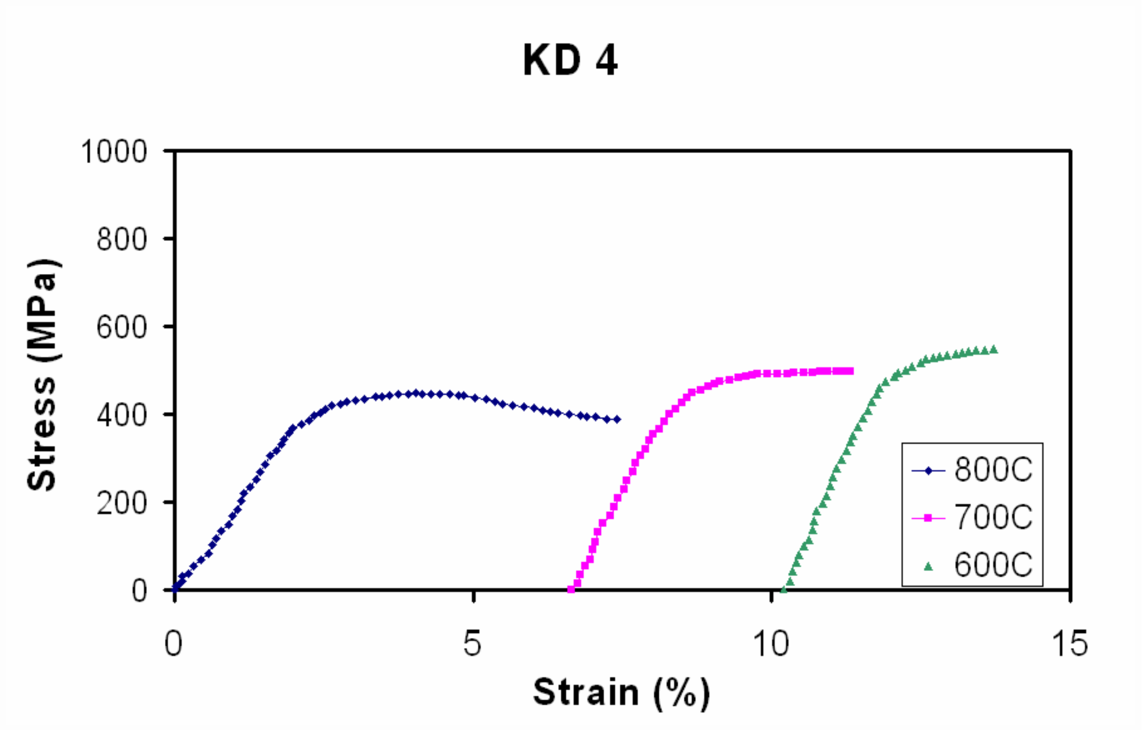
KD 4
Stress (MPa)
1000
800
600
400
200
0
0
5
10
15
Strain (%)
800C
700C
600C

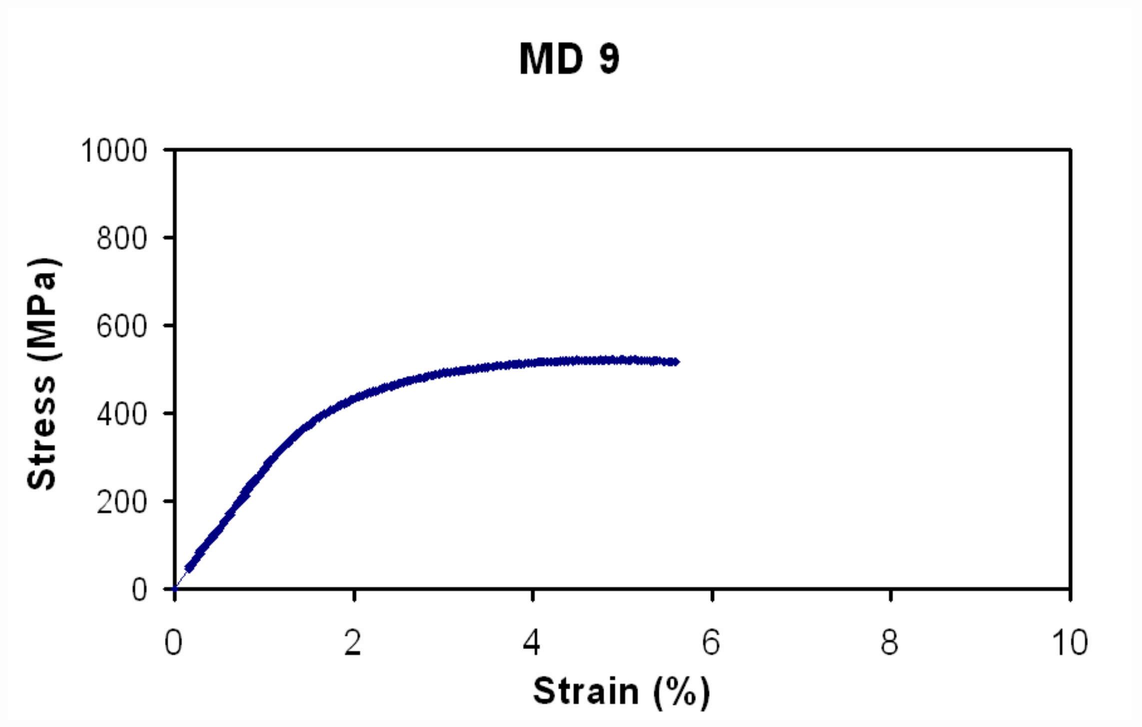
MD 9
Stress (MPa)
1000
800
600
400
200
0
0
2
4
6
8
10
Strain (%)

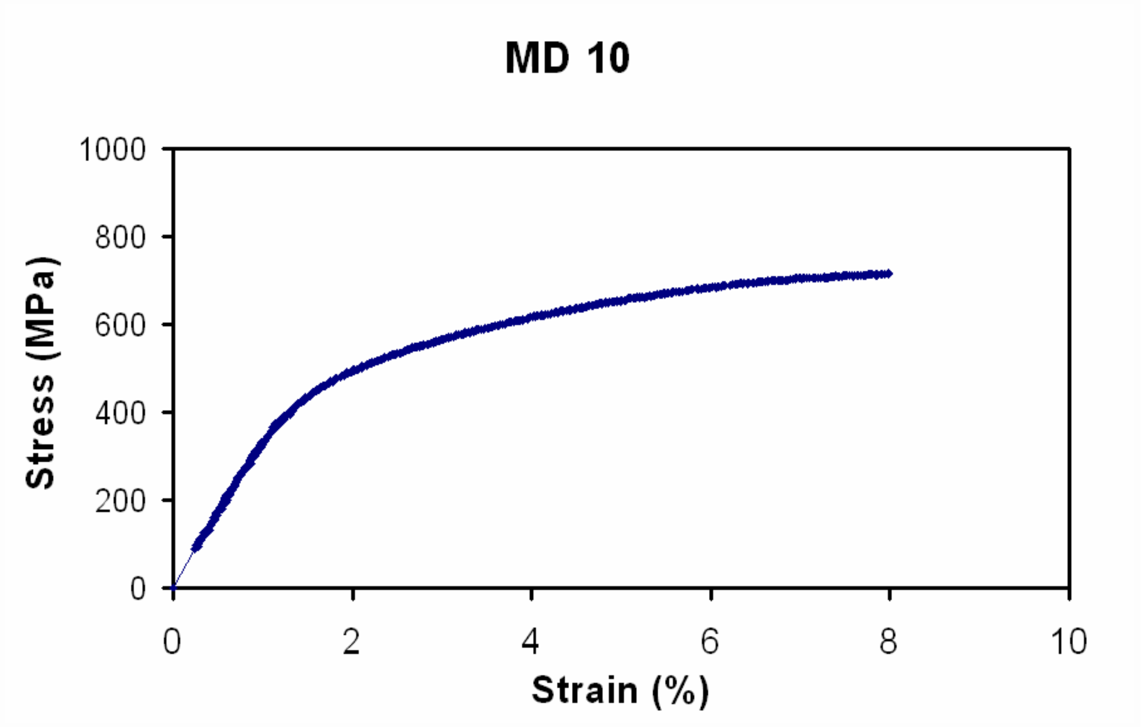
MD 10
Stress (MPa)
1000
800
600
400
200
0
0
2
4
6
8
10
Strain (%)

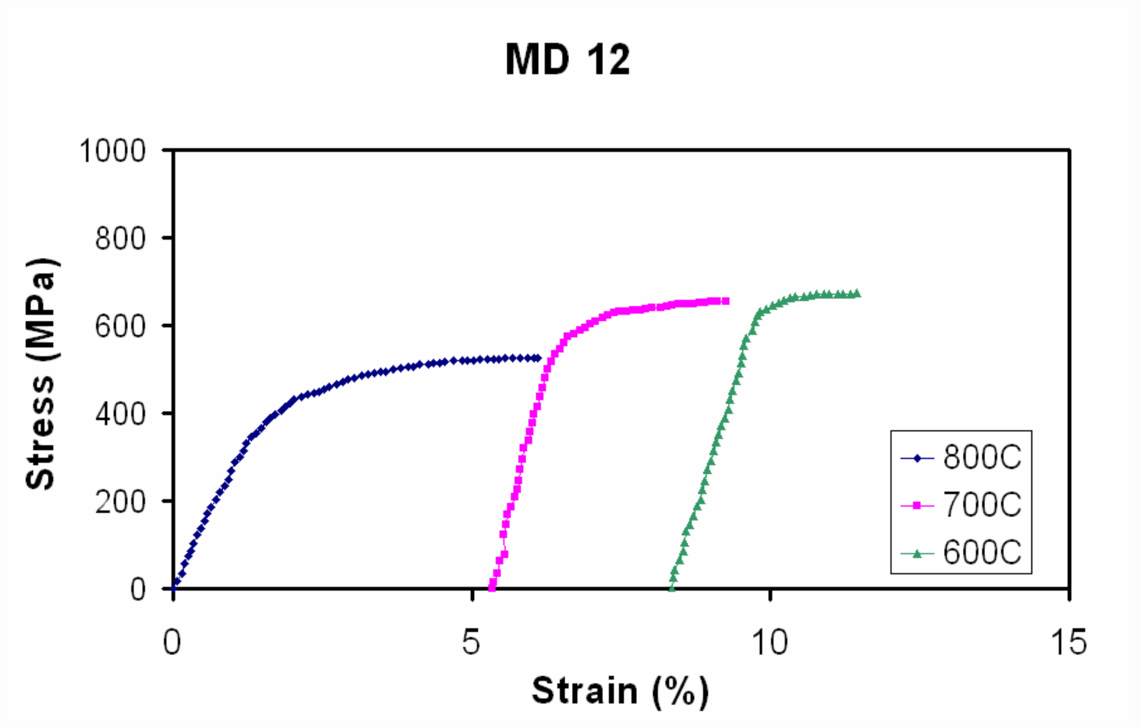
MD 12
Stress (MPa)
1000
800
600
400
200
0
0
5
10
15
Strain (%)
800C
700C
600C

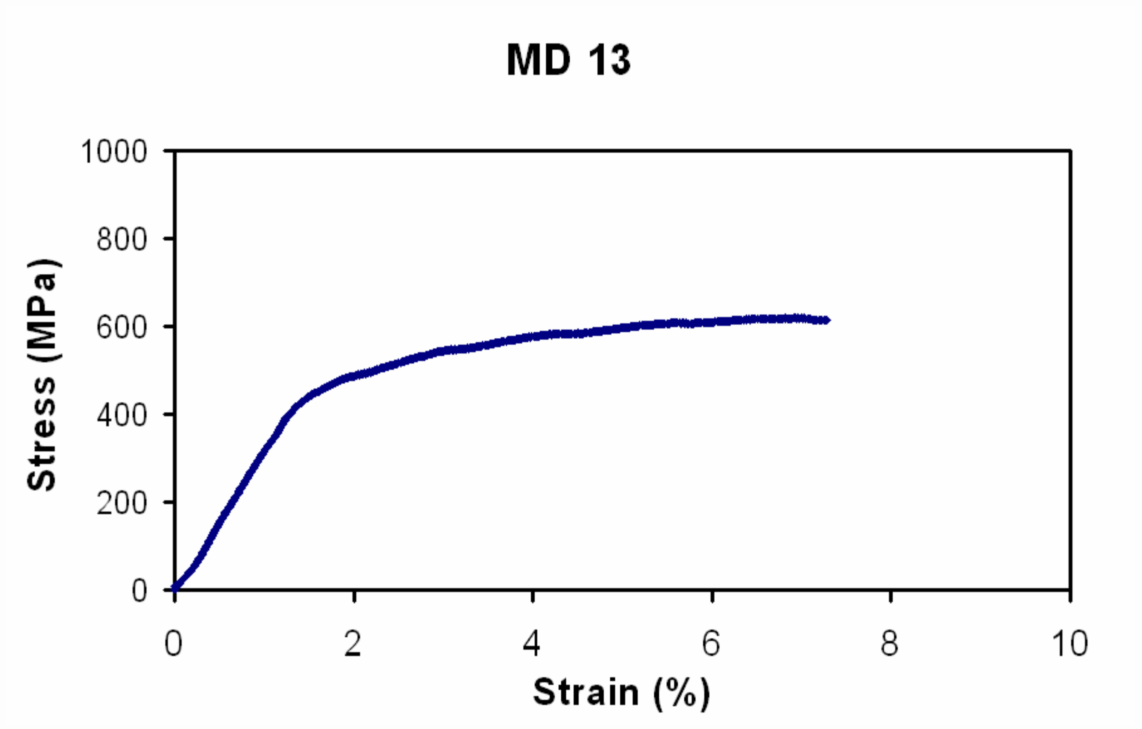
MD 13
Stress (MPa)
1000
800
600
400
200
0
0
2
4
6
8
10
Strain (%)

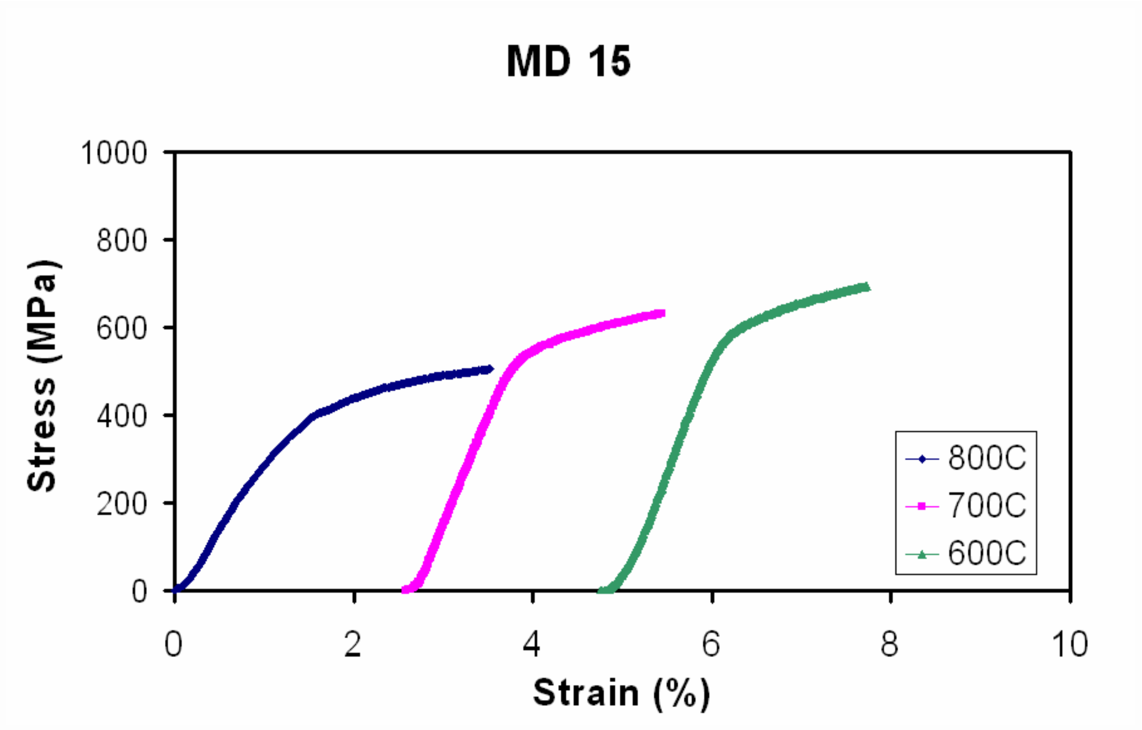
MD 15
Stress (MPa)
1000
800
600
400
200
0
0
2
4
6
8
10
Strain (%)
800C
700C
600C

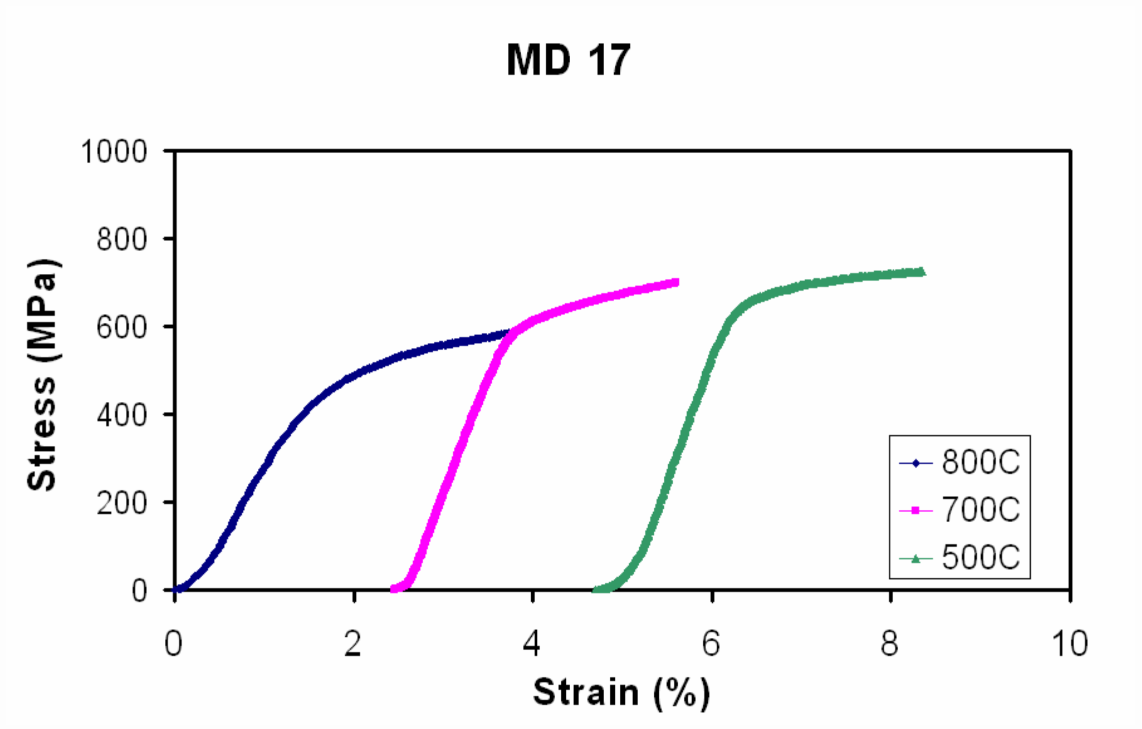
MD 17
Stress (MPa)
1000
800
600
400
200
0
0
2
4
6
8
10
Strain (%)
800C
700C
500C

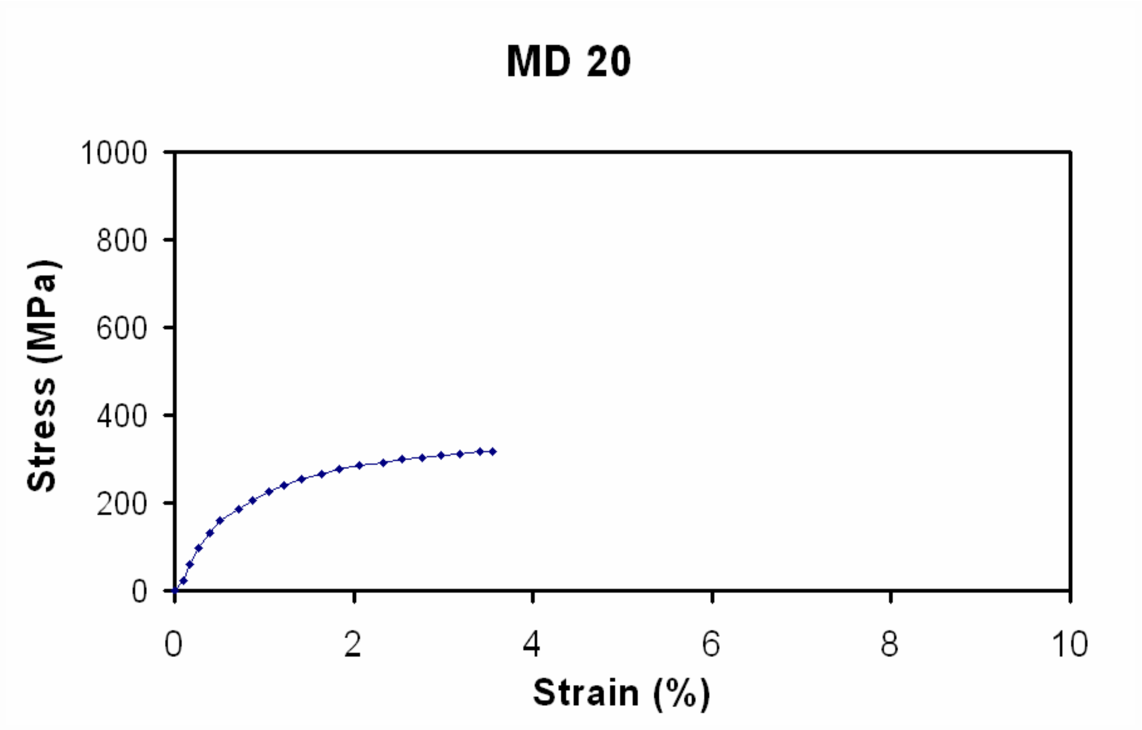
MD 20
Stress (MPa)
1000
800
600
400
200
0
0
2
4
6
8
10
Strain (%)

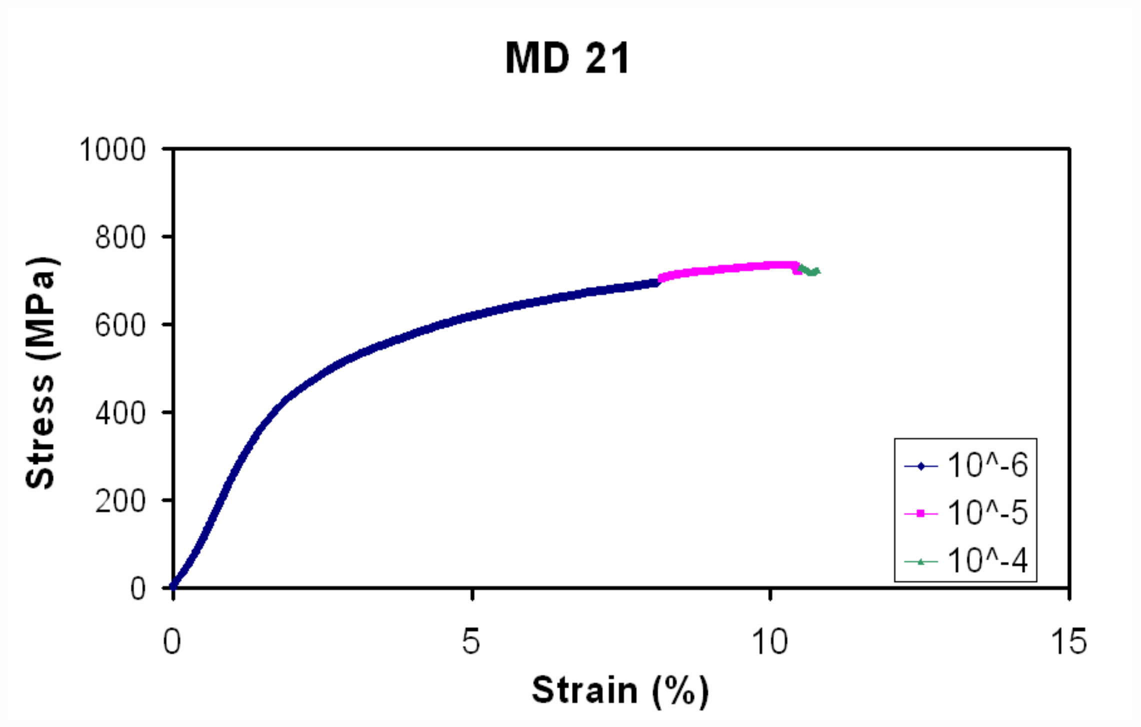
MD 21
Stress (MPa)
1000
800
600
400
200
0
0
5
10
15
Strain (%)
10^-6
10^-5
10^-4

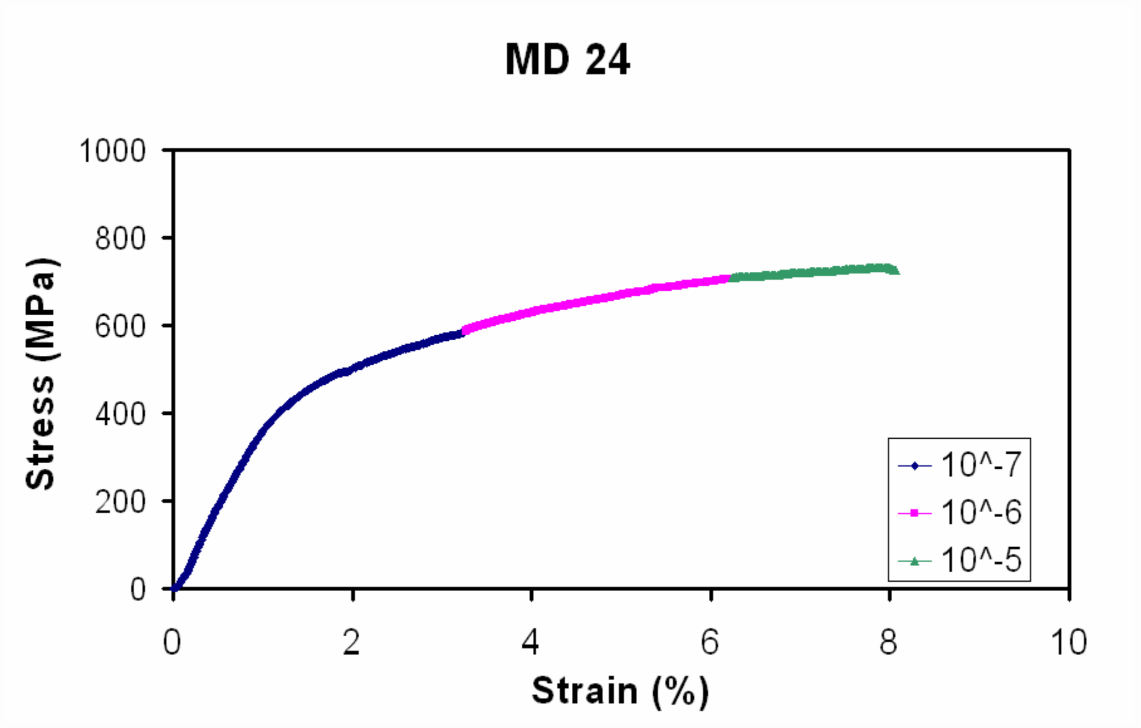
MD 24
Stress (MPa)
1000
800
600
400
200
0
0
2
4
6
8
10
Strain (%)
10^-7
10^-6
10^-5

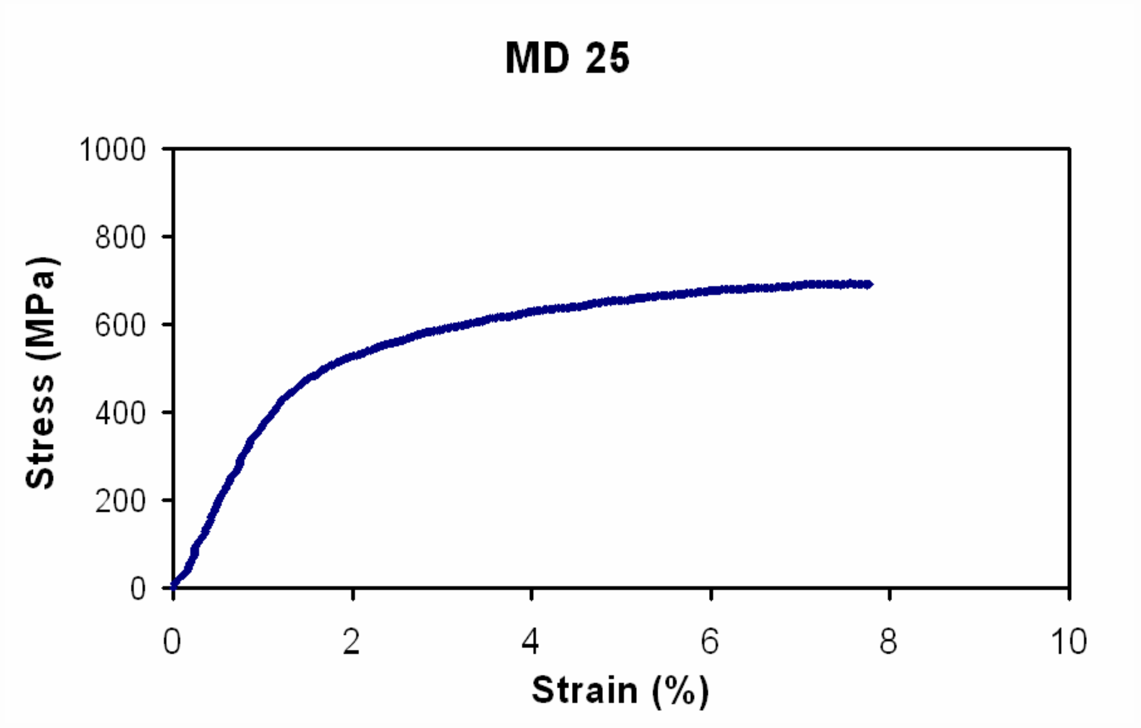

MD 25

1000
800
600
400
200
0
Stress (MPa)
0
2
4
6
8
10
Strain (%)

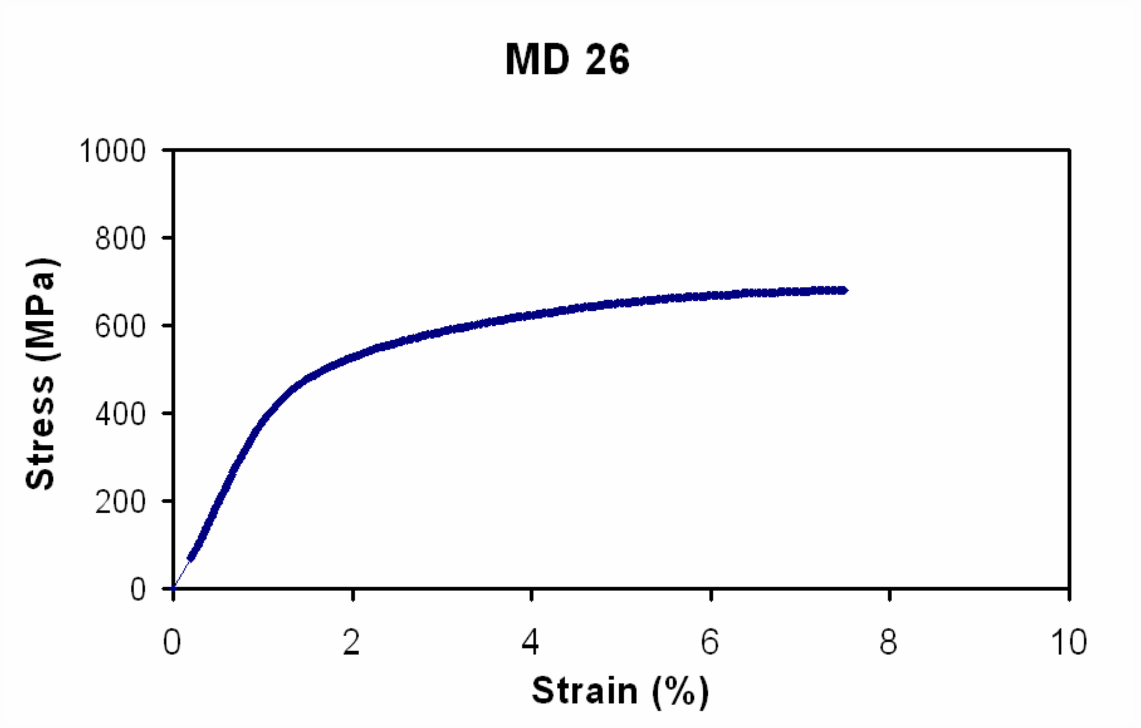

MD 26

1000
800
600
400
200
0
Stress (MPa)
0
2
4
6
8
10
Strain (%)

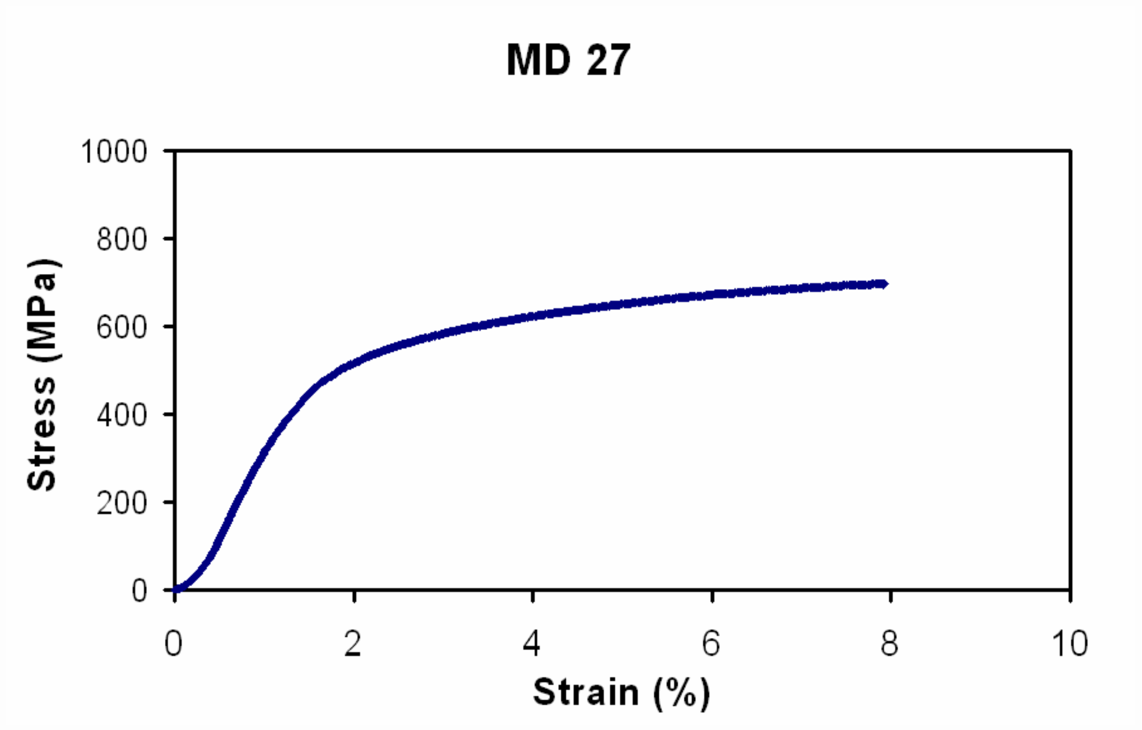
MD 27
Stress (MPa)
1000
800
600
400
200
0
0
2
4
6
8
10
Strain (%)

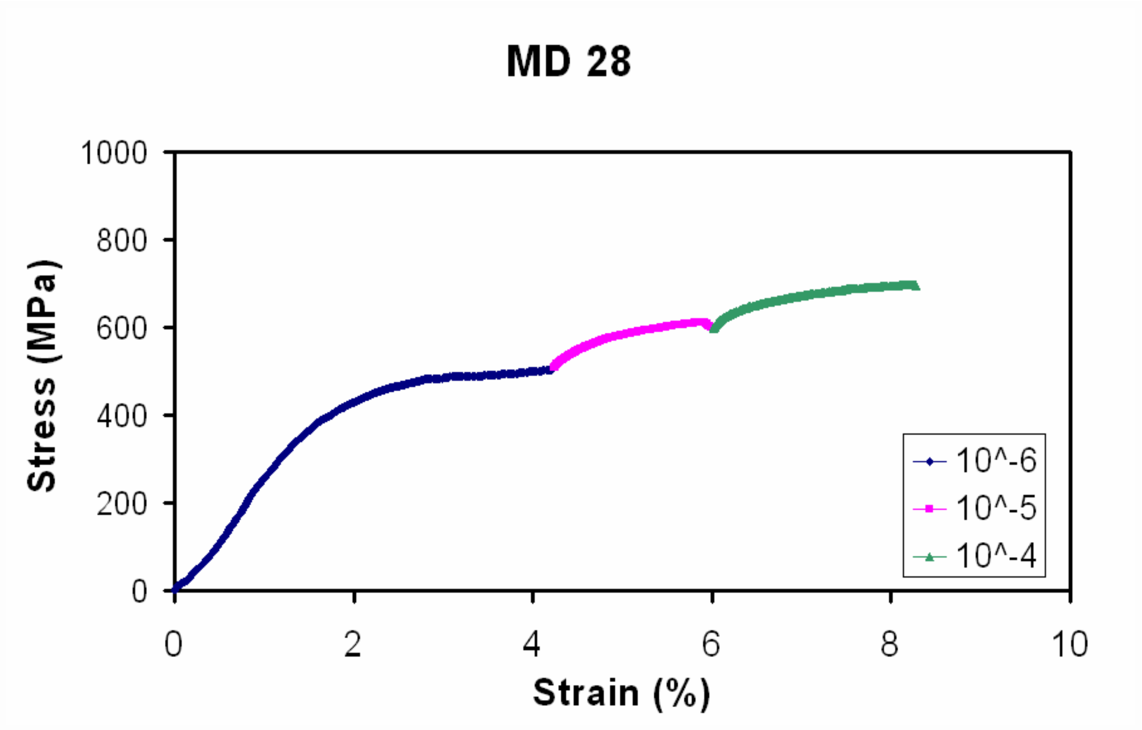
MD 28
Stress (MPa)
1000
800
600
400
200
0
0
2
4
6
8
10
Strain (%)
10^-6
10^-5
10^-4

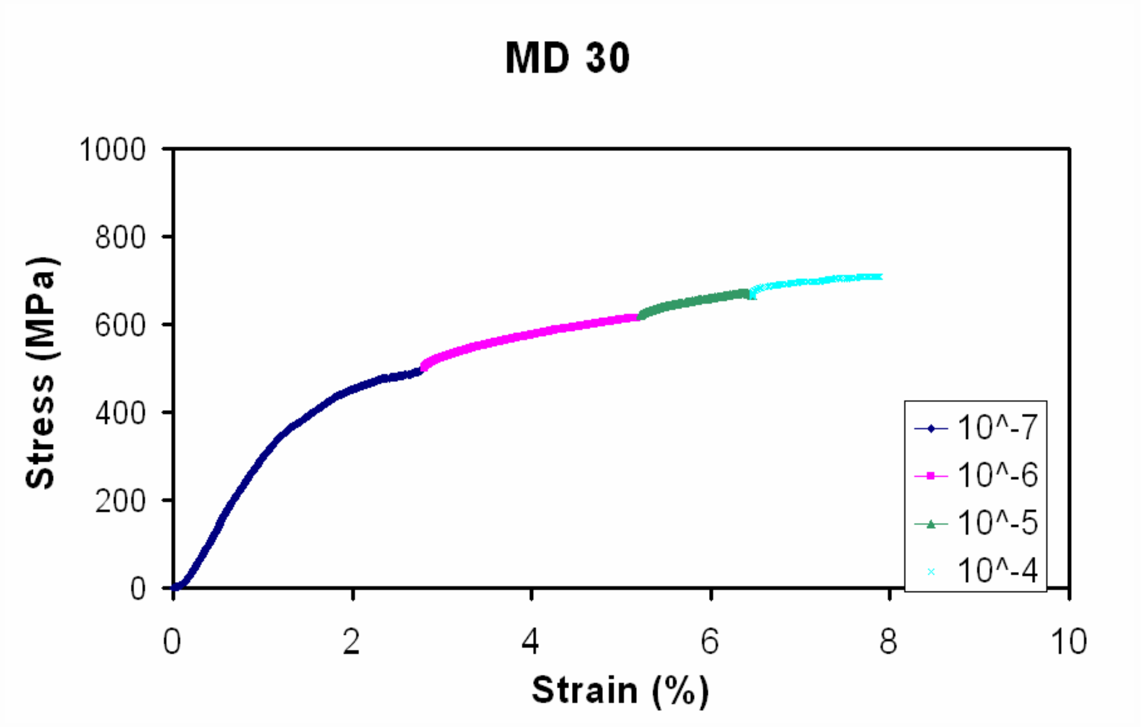
MD 30
Stress (MPa)
1000
800
600
400
200
0
0
2
4
6
8
10
Strain (%)
10^-7
10^-6
10^-5
10^-4

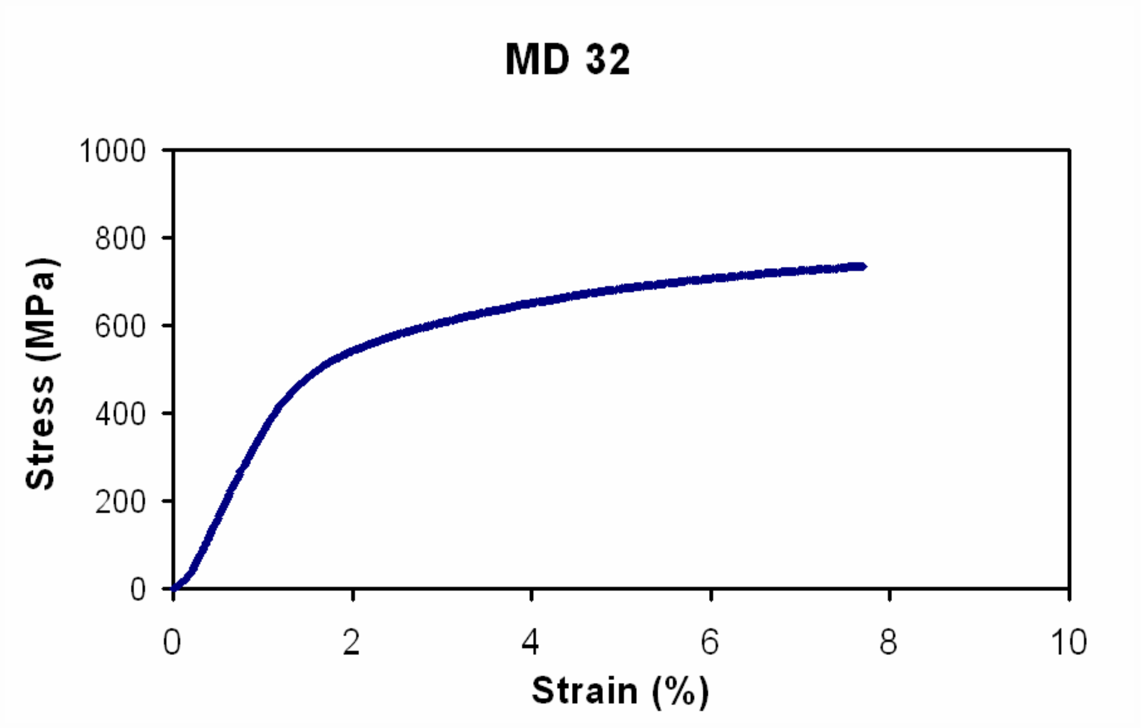
MD 32
Stress (MPa)
1000
800
600
400
200
0
0
2
4
6
8
10
Strain (%)

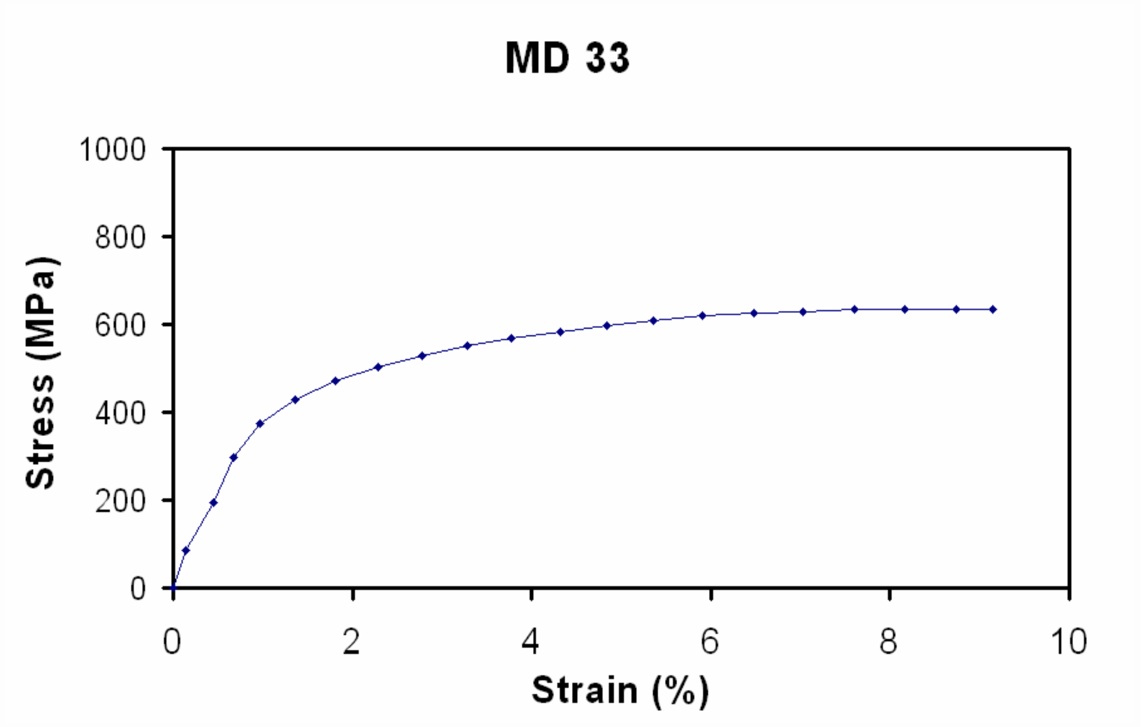
MD 33
Stress (MPa)
1000
800
600
400
200
0
0
2
4
6
8
10
Strain (%)

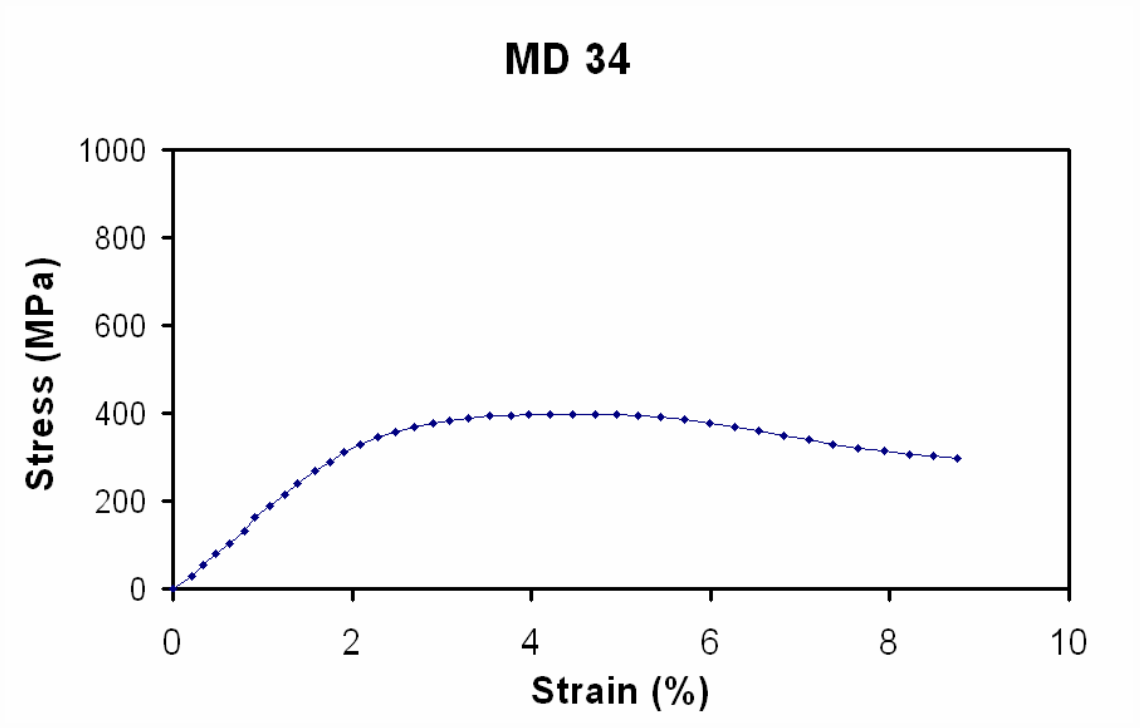
MD 34
Stress (MPa)
1000
800
600
400
200
0
0
2
4
6
8
10
Strain (%)

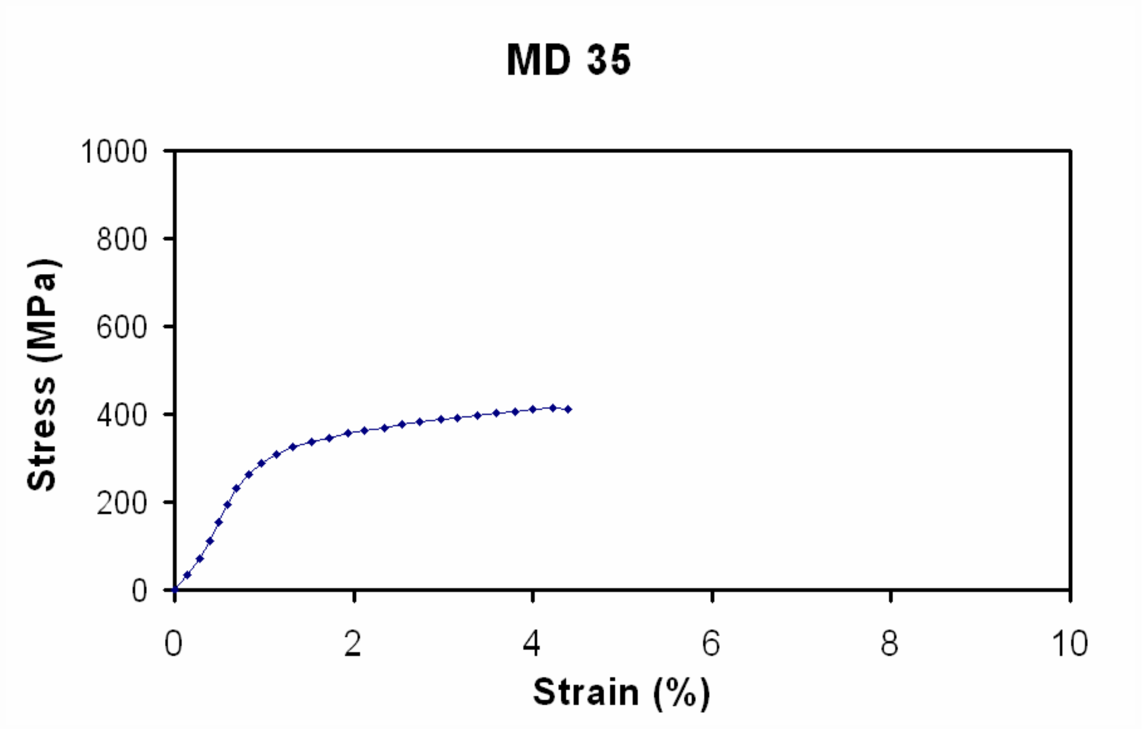
MD 35
1000
800
600
400
200
0
Stress (MPa)
0
2
4
6
8
10
Strain (%)

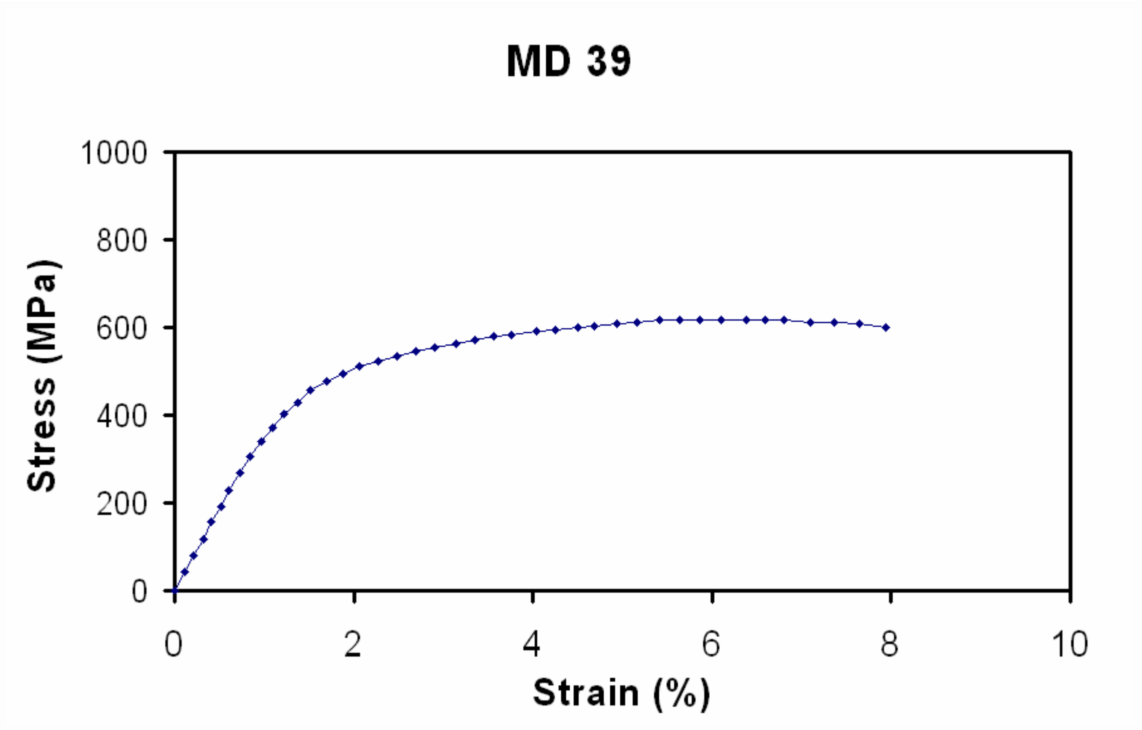
MD 39
1000
800
600
400
200
0
Stress (MPa)
0
2
4
6
8
10
Strain (%)

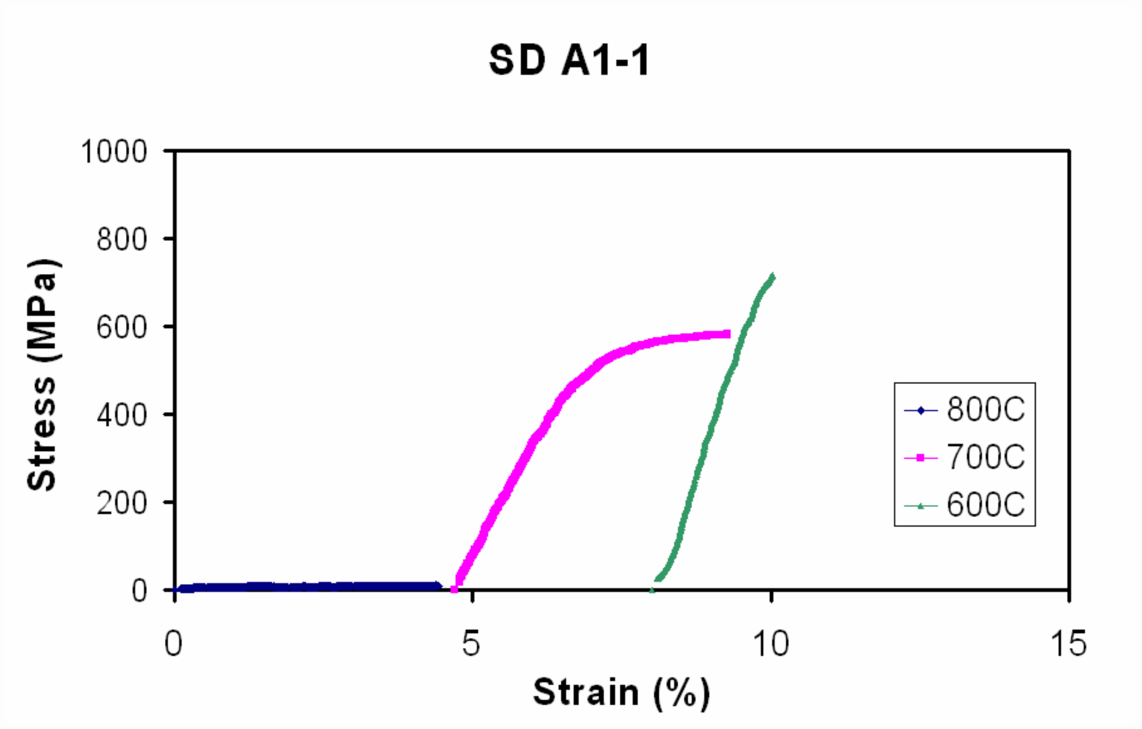
SD A1-1
1000
800
600
400
200
0
Stress (MPa)
0
5
10
15
Strain (%)
800C
700C
600C

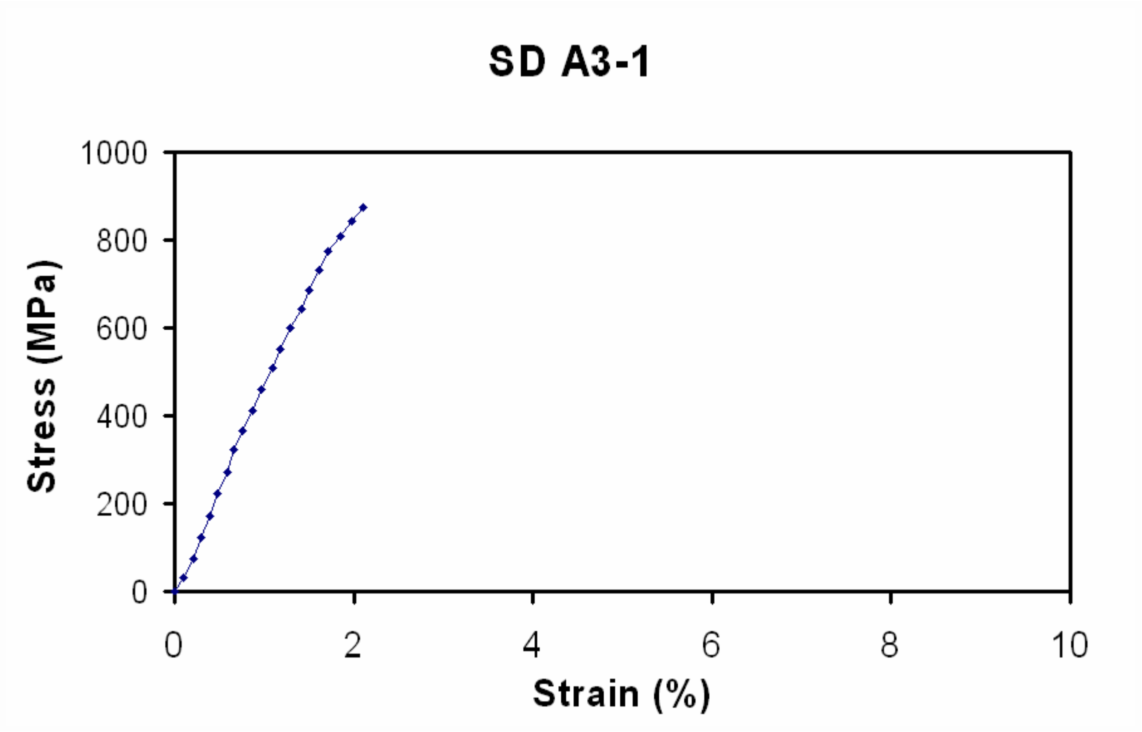
SD A3-1
1000
800
600
400
200
0
Stress (MPa)
0
2
4
6
8
10
Strain (%)

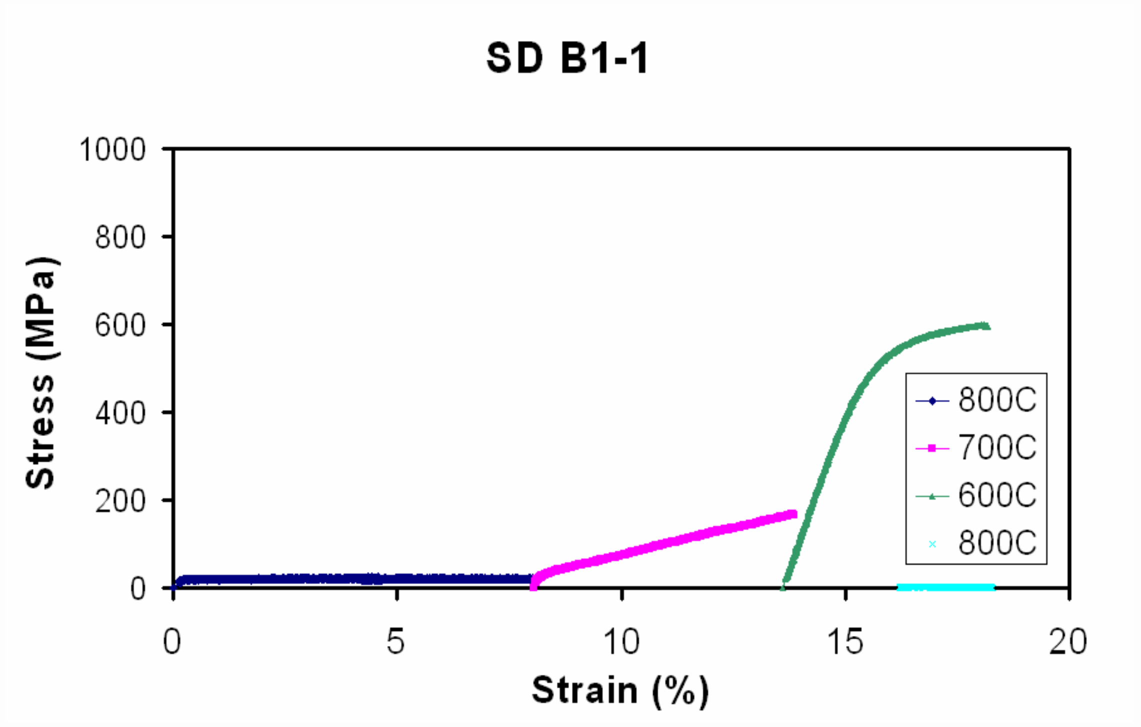
SD B1-1
Stress (MPa)
1000
800
600
400
200
0
0
5
10
15
20
Strain (%)
800C
700C
600C
800C

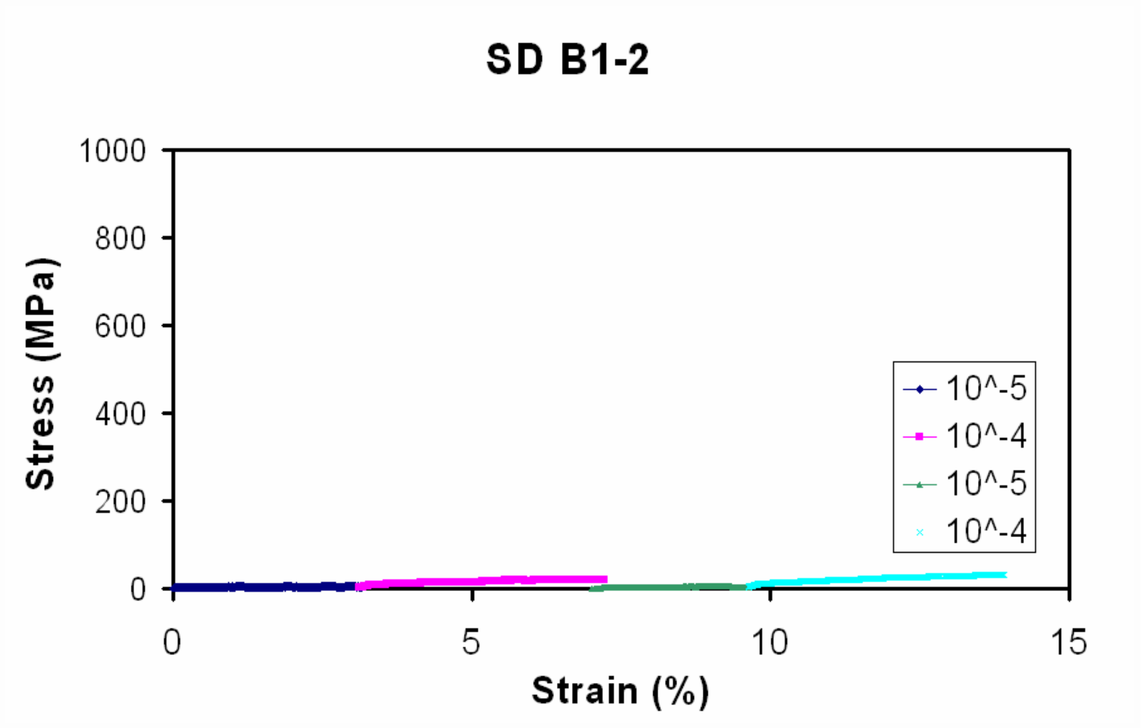
SD B1-2
Stress (MPa)
1000
800
600
400
200
0
0
5
10
15
Strain (%)
10^-5
10^-4
10^-5
10^-4

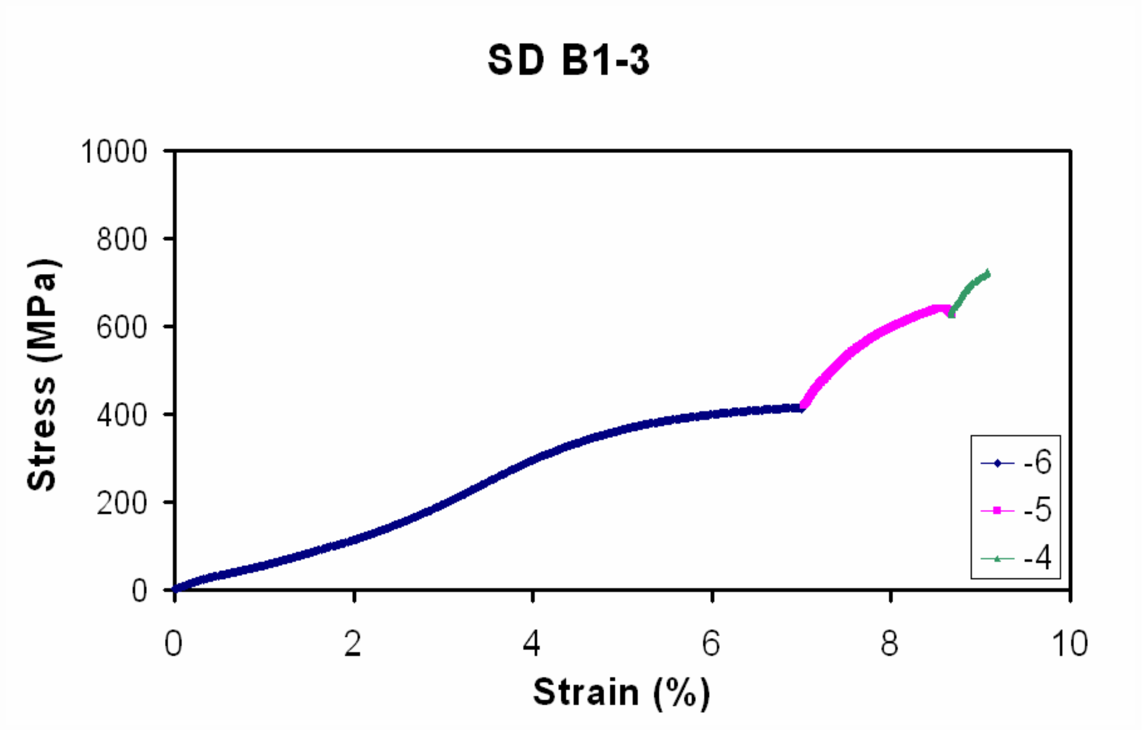
SD B1-3
Stress (MPa)
1000
800
600
400
200
0
Strain (%)
0
2
4
6
8
10
-6
-5
-4

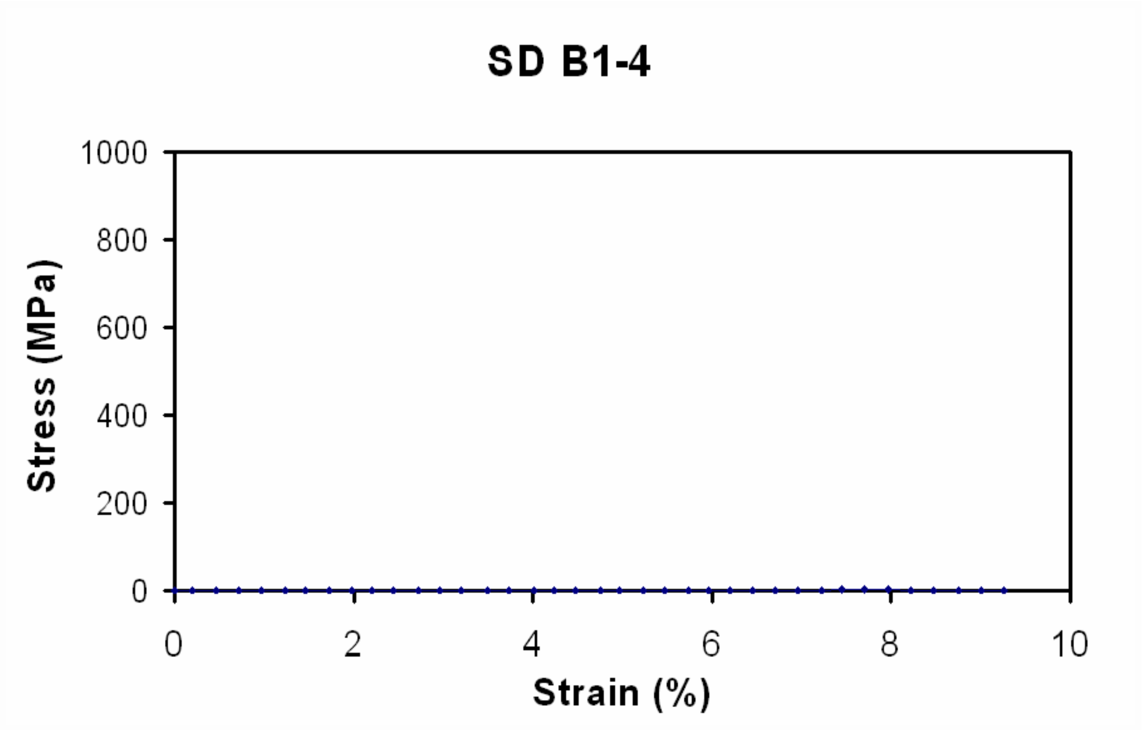
SD B1-4
Stress (MPa)
1000
800
600
400
200
0
Strain (%)
0
2
4
6
8
10

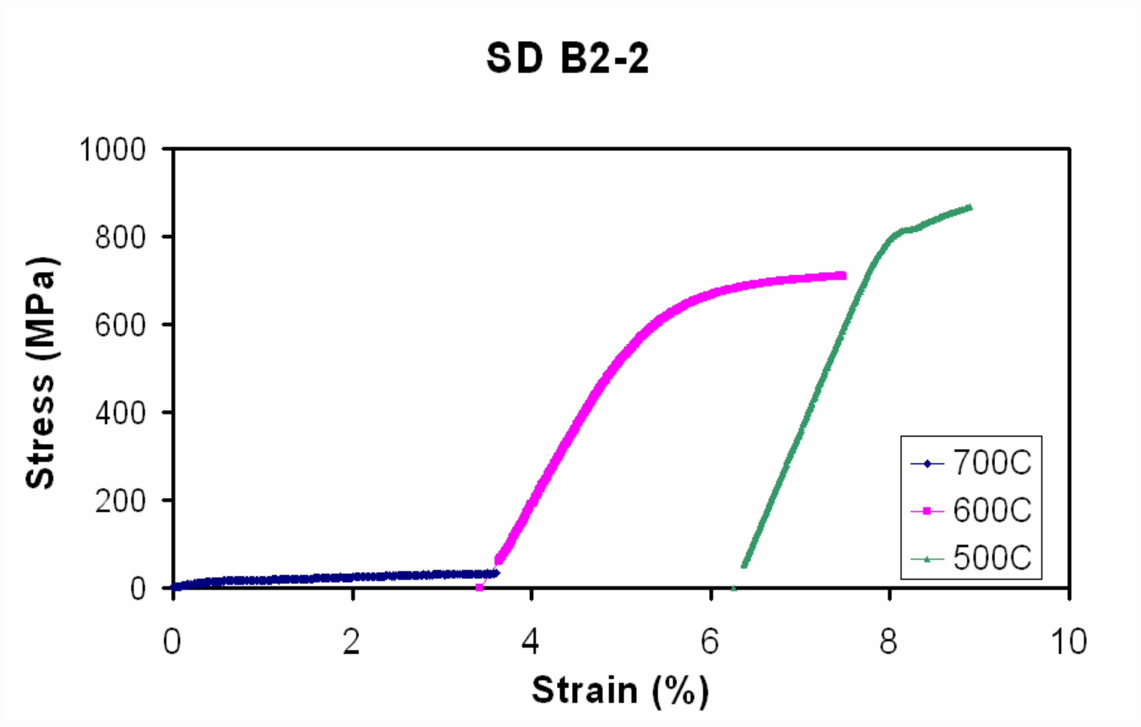
SD B2-2
Stress (MPa)
1000
800
600
400
200
0
0
2
4
6
8
10
Strain (%)
700C
600C
500C

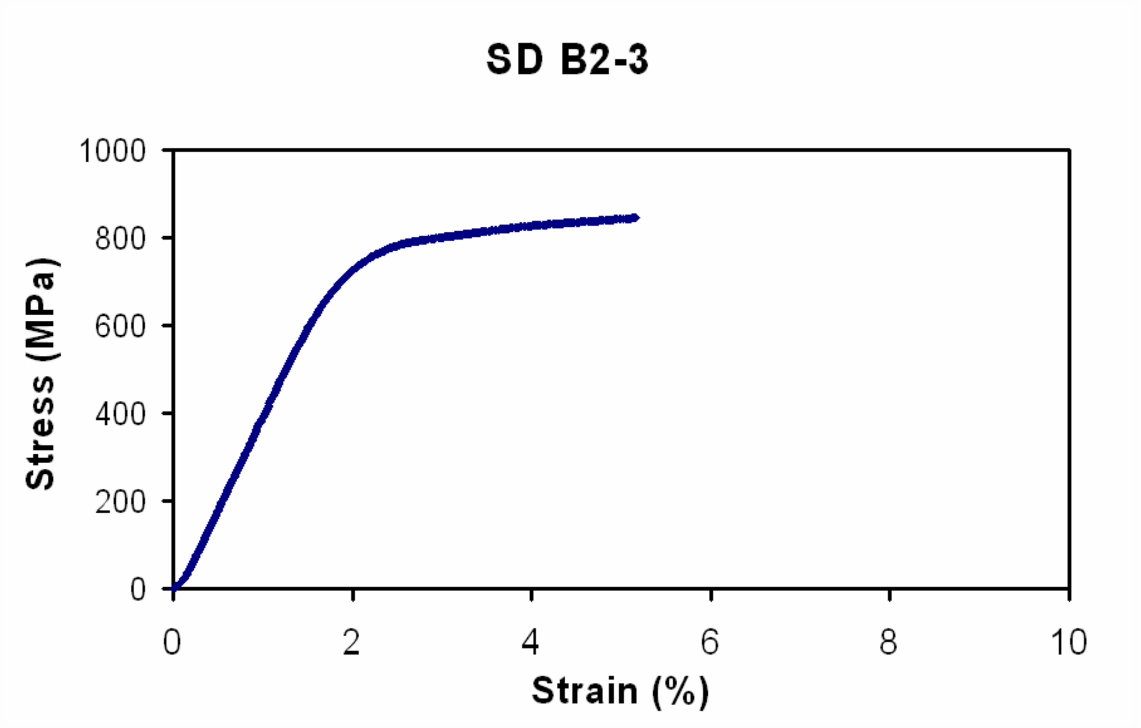
SD B2-3
Stress (MPa)
1000
800
600
400
200
0
0
2
4
6
8
10
Strain (%)

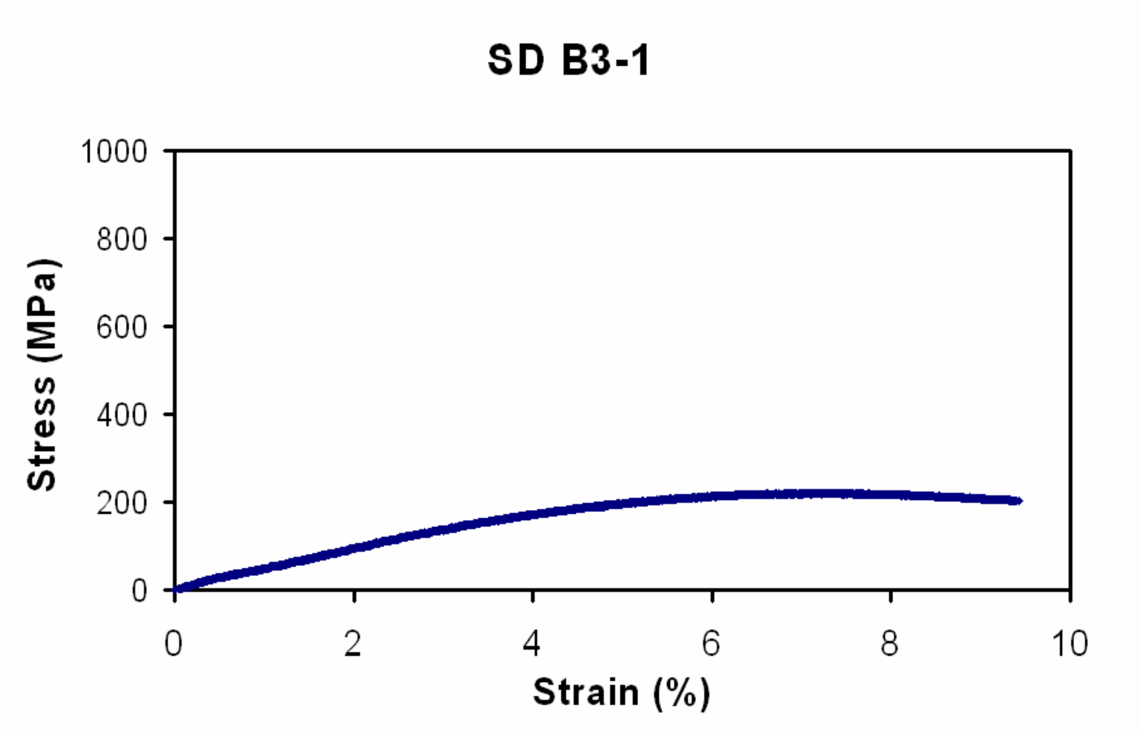
SD B3-1
Stress (MPa)
1000
800
600
400
200
0
0
2
4
6
8
10
Strain (%)

VITA

Name: Nathan E. Davis

Address: The Department of Geology & Geophysics, Texas A&M University
College Station, TX 77843-3115

Education: B.S., Geology, University of Missouri: Rolla, May 2001
MS., Geology, Texas A&M University, August 2005